

Computational modelling of fracture with local maximum entropy approximations

Bruch-Modellierung mit lokalen
Maximum-Entropie Approximationen

DISSERTATION

Zur Erlangung des akademischen Grades eines
Doktor-Ingenieur (Dr.-Ing.)
an der Fakultät Bauingenieurwesen
der Bauhaus Universität Weimar

vorgelegt von

M.Sc., Fatemeh Amiri

geboren am 21. März 1984

in Ahvaz, Iran

Mentor:

Prof. Dr.-Ing. Timon Rabczuk

Weimar, August 2015

To my family ...

Acknowledgements

Conducting the research and writing the results for this thesis is an iterative process that has taken place over several years. It would have been difficult to accomplish without the support and encouragement I have received. I would particularly like to thank my adviser, Prof. Dr.-Ing. Rabczuk, for sharing his insights and knowledge in the field of fracture mechanics. I have greatly benefited, as a researcher and student, from his experience and supervision.

The first part of my work has been in collaboration with Dr. C. Anitescu. Innumerable discussions between us helped me to dig into the field of meshfree methods. His suggestions and guidance have been useful in thinking out of the box. Furthermore, special thanks to him for his comments during the review and preparation of my thesis. During my research, I spent seven months at the Dept. of de Matemática Aplicada 3., in collaboration with Prof. M. Arroyo, Universitat Politècnica de Catalunya, Spain. The research collaboration helped in applying my phase field method to thin shell problems with complex geometry and topology. Many thanks to him for the nice cooperation. The support extended by my colleagues at UPC, in particular Dr. D. Millán, Behrooz Hashemian is appreciated. Special thanks to Dr. D. Millán, who helped me a lot while staying in UPC and afterward. He shared with me his computer codes, which has made my project progress fast. I would also like to thank Prof. Stéphane Bordas and Prof. Y. Shen for their assistance in insightful suggestions and collaboration in research. I am grateful to thank all my colleagues at the ISM, especially Mohammad Silani, for their friendly support. I am thankful for the help from the secretaries Frau Terber and Frau Rosemarie.

I also would like to thank the Free State of Thuringia and Bauhaus Research School for financial support during the duration of my project. I am thankful for the help from the Stipendienkoordination/Promotionsberatung, Frau Marion Hensel. I would like to thank the DAAD Programme des Projektbezogenen Personenaustauschs, for financial support to trip to Spain. Thanks to all for making my life in Weimar memorable.

Fatemeh Amiri

Weimar, June 2015

Abstract

The key objective of this research is to study fracture with a meshfree method, local maximum entropy approximations, and model fracture in thin shell structures with complex geometry and topology. This topic is of high relevance for real-world applications, for example in the automotive industry and in aerospace engineering. The shell structure can be described efficiently by meshless methods which are capable of describing complex shapes as a collection of points instead of a structured mesh. In order to find the appropriate numerical method to achieve this goal, the first part of the work was development of a method based on local maximum entropy (LME) shape functions together with enrichment functions used in partition of unity methods to discretize problems in linear elastic fracture mechanics. We obtain improved accuracy relative to the standard extended finite element method (XFEM) at a comparable computational cost. In addition, we keep the advantages of the LME shape functions, such as smoothness and non-negativity. We show numerically that optimal convergence (same as in FEM) for energy norm and stress intensity factors can be obtained through the use of geometric (fixed area) enrichment with no special treatment of the nodes near the crack such as blending or shifting.

As extension of this method to three dimensional problems and complex thin shell structures with arbitrary crack growth is cumbersome, we developed a phase field model for fracture using LME. Phase field models provide a powerful tool to tackle moving interface problems, and have been extensively used in physics and materials science. Phase methods are gaining popularity in a wide set of applications in applied science and engineering, recently a second order phase field approximation for brittle fracture has gathered significant interest in computational fracture such that sharp cracks discontinuities are modeled by a diffusive crack. By minimizing the system energy with respect to the mechanical displacements and the phase-field, subject to an irreversibility condition to avoid crack healing, this model can describe crack nucleation, propagation, branching and merging. One of the main advantages of the phase field modeling of fractures is the unified treatment of the interfacial tracking and

mechanics, which potentially leads to simple, robust, scalable computer codes applicable to complex systems. In other words, this approximation reduces considerably the implementation complexity because the numerical tracking of the fracture is not needed, at the expense of a high computational cost. We present a fourth-order phase field model for fracture based on local maximum entropy (LME) approximations. The higher order continuity of the meshfree LME approximation allows to directly solve the fourth-order phase field equations without splitting the fourth-order differential equation into two second order differential equations. Notably, in contrast to previous discretizations that use at least a quadratic basis, only linear completeness is needed in the LME approximation. We show that the crack surface can be captured more accurately in the fourth-order model than the second-order model. Furthermore, less nodes are needed for the fourth-order model to resolve the crack path. Finally, we demonstrate the performance of the proposed meshfree fourth order phase-field formulation for 5 representative numerical examples. Computational results will be compared to analytical solutions within linear elastic fracture mechanics and experimental data for three-dimensional crack propagation.

In the last part of this research, we present a phase-field model for fracture in Kirchoff-Love thin shells using the local maximum-entropy (LME) meshfree method. Since the crack is a natural outcome of the analysis it does not require an explicit representation and tracking, which is advantage over techniques as the extended finite element method that requires tracking of the crack paths. The geometric description of the shell is based on statistical learning techniques that allow dealing with general point set surfaces avoiding a global parametrization, which can be applied to tackle surfaces of complex geometry and topology. We show the flexibility and robustness of the present methodology for two examples: plate in tension and a set of open connected pipes.

Contents

Contents	VII
List of Figures	IX
List of Tables	XIII
1 Introduction	1
1.1 Background and motivation	1
1.2 Discrete fracture models	2
1.3 Continuous fracture models	3
1.4 Local Maximum Entropy (LME) approximants	5
1.5 Contributions and Organization	6
2 Local Maximum entropy approximants	9
2.1 Local Maximum entropy shape functions	10
3 Extended Local Maximum entropy method	15
3.1 Basic Fracture Mechanics Concepts	15
3.2 Extrinsic enrichments for Partition of Unity Methods	16
3.3 Numerical Examples	19
3.3.1 Infinite plate with a horizontal crack	19
3.3.2 Edge crack under shear traction	23
3.3.3 Slanted crack in an infinite plate	24
4 Phase-field model for Local Maximum entropy approximants	29
4.1 Governing Equations and Weak Form	30
4.1.1 Second and fourth-order phase field model	30

4.1.2	Phase field model for an elastic body	33
4.2	Discretization with LME approximates	35
4.3	Numerical Examples	36
4.3.1	Phase Field Problems	36
4.3.2	Mechanical Problems	42
5	Phase-field modeling of fracture mechanics in thin shells	55
5.1	Dimensionality Reduction	57
5.2	Manifold description from scattered points	58
5.3	Thin shell model	61
5.3.1	Kinematics of the shell	62
5.3.2	Thin shell potential energy	63
5.3.3	Phase-field model for thin shell structures	64
5.3.4	Galerkin discretization	66
5.4	Numerical results	67
5.4.1	Single edge notch tensile	67
5.4.2	Connected pipes pulling	71
6	Conclusions and future work	75
6.1	Contributions	75
6.2	Open lines for research	77
Appendix A Derivatives of the LME shape functions		79
Appendix B The Γ-convergence approximation conjecture of De Giorgi model		83
Appendix C The Green–Lagrange strain tensor for Kirchhoff–Love assumptions		85
C.1	Equilibrium configuration of thin shells	86
C.2	Small displacements	87
Bibliography		89

List of Figures

2.1	Local max-ent shape functions in 2D.	14
3.1	Signed distance function.	16
3.2	Signed distance function.	18
3.3	Infinite plate with a center crack under uniform tension and modeled geometry ABCD.	20
3.4	Error in the energy norm for the horizontal crack problem in mode I. .	21
3.5	Percentage error of stress intensity factor for horizontal crack.	22
3.6	Elements which have a node within a ball of radius r_d around the crack tip.	22
3.7	Edge-cracked plate under shear stress.	24
3.8	Percentage error of K_I for edge-cracked plate under shear stress.	25
3.9	Percentage error of K_{II} for edge-cracked plate under shear stress.	25
3.10	a) Slanted crack in an infinite plate where the principal stress is not perpendicular to the crack. b) An infinite plate rotated with respect to the crack's angle.	26
3.11	Percentage error of K_I for slanted crack in an infinite plate with $\alpha = 30^\circ$	28
3.12	Percentage error of K_{II} for slanted crack in an infinite plate with $\alpha = 30^\circ$	28
4.1	(a) Sharp crack at $x = 0$, (b) Exponential solution of the second order phase field model and (c) Exponential solution of the fourth order phase field model with the length scale parameter $l = 2l_0$	31
4.2	The error in the L^2 norm and Semi-norm H^1 of the solution of the second order ODE as a function of nodal spacing, h , with $l_0 = 0.025$ and different values of γ	37

4.3	The error in the L^2 norm and Semi-norm H^1 of the solution of the fourth order ODE as a function of nodal spacing, with $l_0 = 0.025$ and different values of γ	37
4.4	The error in semi-norm H^2 of the solution of the fourth order ODE as a function of nodal spacing, with $l_0 = 0.025$ and different values of γ	38
4.5	Two dimensional 1×1 square, with a sharp crack surface $\Gamma = 0.5$	39
4.6	Exact crack length over approximated crack length versus length scale parameter over nodal spacing, by (a) the second order phase field model with $\gamma = 0.8, 1.8, 4.8$, and (b) the fourth order phase field model with $\gamma = 0.6, 0.8, 1.0$, for $h = 0.0013$	40
4.7	Exact crack length over approximated crack length versus length scale parameter over nodal spacing the fourth order phase field model with $\gamma = 0.6, 1.8$, for $h = 0.0013$	40
4.8	L^2 norm error versus length scale parameter over nodal spacing, by (a) the second order phase field model with $\gamma = 4.8$, and (b) the fourth order phase field model with $\gamma = 0.8$	41
4.9	Absolute error of the crack length for the second and fourth order models.	41
4.10	(a) L^2 norm Error for $h = 0.005$, and different values of l_0 , (b) L^2 norm Error versus different discretization.	43
4.11	The geometry and boundary conditions of a square beam of side length $L = 1$ mm.	44
4.12	Load-deflection curves of (a) the second order model with $\gamma = 4.8$, (b) the fourth order model with $\gamma = 1.0$, $l_0 = 2h$, $h = 0.0015, 0.0008$ and $15274, 60931$ nodes respectively.	44
4.13	(a) Load-deflection curves of the second order method for different values of l_0 , fixed value $h = 0.0015$ and $\gamma = 4.8$. (b) Load-deflection curves of the fourth order model for different values of l_0 , fixed value $h = 0.0015$ and $\gamma = 1.0$	45
4.14	Close up around the crack path at the three stages of evolution.	45
4.15	Geometry, loading and boundary condition for the three-dimensional mode-I tension test.	46
4.16	The crack path at the four stages of evolution.	47
4.17	Phase field results on the cross section plane $y = 2.5$ to indicate crack path inside the body.	47

4.18	Load-deflection curves of the second order method with $\gamma = 4.8$, $l_0 = 0.414$ and different refinement with 1661, 14453, 28177 number of nodes respectively.	48
4.19	Load-deflection curves of the fourth order method with $\gamma = 1.8$, $l_0 = 0.414$ and different refinement with 14453, 28177 number of nodes respectively.	48
4.20	Reaction force-displacement curves for the fourth order model with $h = 0.1$, $l_0 = 0.414$, $\gamma = 1.8$ and different values of G_c	49
4.21	Geometry, loading and boundary condition for the three-dimensional Single edge notched beam.	50
4.22	The crack path at two different views.	50
4.23	Crack path for the fourth and the second order phase field methods with $\gamma = 1.8$ and $\gamma = 4.8$ respectively, compared with the experiments in [1].	51
4.24	Reaction force displacement curve for point A, compared with [1, 2]. . .	51
4.25	Side and top views of the beam with an initial crack for the non-planar crack growth.	52
4.26	Evolution of the crack front in the beam seen from the top, the maximum and the minimum of phase field, i.e. $v = 1$ and $v = 0$ are shown.	53
4.27	The crack path at the different stages of evolution from a side view, the maximum and the minimum of phase field, i.e. $v = 1$ and $v = 0$ are shown.	53
5.1	Some thin shell structures are found in nature.	56
5.2	Tag Kasra: is a Sassanid-era Persian monument located near the modern town of Salman Pak, Iraq. It is the only visible remaining structure of the ancient city of Ctesiphon. The archway is the largest single-span vault of unreinforced brickwork in the world. Picture from 1864 (a), picture from 2003 (b).	57
5.3	Building made of shell structures, Valencia aquarium.	57
5.4	Swiss roll benchmark in dimensionality reduction. (A) Sampling in 3D by an unstructured set of points. Two-dimensional embeddings obtained with PCA (B), MLLE (C), and Isomap (D). Color is used to identify the location of the points. PCA fails because the sampled manifold is not unfolded and the points collapse in a line [3].	59

5.5	Three point-set surfaces that require partitioning for different reasons: (A) and (B) for their non-trivial topology, and (C) for its complex geometry.	60
5.6	Reference and the deformed configurations of the middle shell surface. .	62
5.7	Square plate of side length $L = 1$ mm with initial crack of length $L/2$ under pure tension.	68
5.8	(Left) initial phase-field parameter values with initial crack width of $2h$, (right) phase-field solution of the plate for the final state after full breaking.	69
5.9	Load-deflection curves for FEM and LME with $\gamma = 0.8, 1.8$ and 4.8 . . .	69
5.10	Load-deflection curves for $h = 0.005$, $G_c = 1.0, 1.5, 2.0$ N/mm, $\ell = 0.05$ mm and $\gamma = 1.8$	70
5.11	Load-deflection curves for $h = 0.005$, $G_c = 1.0, 1.5, 2.0$ N/mm, $\ell = 0.025$ mm and $\gamma = 1.8$	70
5.12	Load-deflection curves for $h = 0.0204, 0.0101, 0.005$, $G_c = 1.0$ N/mm, $\ell = 0.05$ mm and $\gamma = 1.8$	71
5.13	Sketch for the brittle thin shell problem. (A) Material and geometrical parameters describing a set of six connected open pipes. (B) The prescribed boundary conditions and the applied incremental displacement. .	72
5.14	Selected snapshots of the deformation process of a brittle thin shell with complex topology. The boundary curve of the bottom pipe is clamped and the top boundary curve is incrementally displaced in the upward $(0, 0, 1)$ direction. The process has been performed without an initial crack. (A,C) Phase field as colormap in the reference configuration for two selected imposed displacements of the top boundary curve, just before the fracture ($d = 0.0055$) and for the final imposed displacement, $d = 0.01$. (B,D) Deformed configurations for two selected instants, the deformation field has been magnified by 20.	73

List of Tables

3.1	Error for energy norm and SIF together with the running time and efficiency ratio (3.8) for a problem discretized with 36×36 nodes. . . .	20
3.2	Error and the average running time when the number of nodes is 36×36 , the number of Gauss points is 16, $\alpha = 15^\circ, 30^\circ$ and radius of influence is 2 for $\gamma = 4.8$ and $\gamma = 3.8$, 3 for $\gamma = 2.8$ and $\gamma = 1.8$	27

Chapter 1

Introduction

1.1 Background and motivation

The modeling of fracture is of major importance in engineering applications such as aircraft fuselages, pressure vessels, automobile components, and castings. The progress in this field and the ability to prevent material failure have helped control the dangers caused by increasing technological complexity. According to report given in [4], the cost of fracture-related damage in the United States estimated at over 100 billion dollars per year. It seems reasonable that this amount could be reduced by advances in fracture mechanics research. Clearly, the damage due to fracture in manufactured components is a significant economic problem. The first step in reducing the costs associated with this phenomenon is understanding it. The study of fracture mechanics is an endeavor that uses concepts from engineering, physics, materials science and statistics to answer some of the following questions:

- Given a particular structure or component, what load conditions and over what period of time can be supported before fracture-related damage occurs?
- In which parts of the structure or the component are cracks more likely to appear and in what direction will they propagate?
- What is the number and size of pre-existing fractures, or fracture-related flaws, at which the structure or component will still be able to operate safely (at least for a specific amount of time)?

The last question in particular is the most important and perhaps also the most surprising. Virtually all materials have flaws that are introduced in the manufacturing process. Over time these flaws become microcracks, which can combine and propagate to become macrocracks that can endanger the safety of the structure or equipment.

Being able to differentiate between an airplane component that is fractured but still able to operate safely and one that is not, can make the difference between a routine flight and a catastrophe.

1.2 Discrete fracture models

A theoretical model for brittle fracture in solids was introduced by Griffith [5] and Irwin [6], which relates crack nucleation and propagation to a critical value of the energy release rate. During the last few decades the numerical simulation of such process has gained importance and often plays a key role in design decisions [4, 7, 8]. This has been mainly motivated by the impossibility to have analytical solutions in most practical situations and the costs of obtaining meaningful and detailed information from experiments. Numerical methods, such as the finite element method have been used to model fracture with some success, but often they are unable to capture some physical properties of the phenomenon. Modeling of moving discontinuities with classical finite elements is difficult to automate because of the requirement that the mesh must conform to the surfaces of discontinuity. It also usually requires local refinement near the fracture zone, in particular near the crack tips where singularities in the stress field occur [9–12].

An attractive approach to overcome these difficulties has been presented by the extended finite element method (XFEM) [13, 14] or the generalized finite element method (GFEM) [15]. These methods allow the approximation of arbitrary discontinuities or singularities by incorporating them in the approximation field through enrichments. This uses the fact that standard shape functions must form a partition of unity, which is then used to patch together the local approximation spaces [16]. This allows the modeling of different features of the solution (including discontinuities and boundary layers) without remeshing, by simply incorporating the information about the character of the solution in the approximation space. Moreover, the quality of the approximation is often also improved with a comparatively lower number of degrees of freedom. For example, crack-tip singularities can be expressed in the approximation space in terms of the branch functions, which provide an optimal representation [13, 14]. Other computational physics problems have been modeled by the use of XFEM [17–24], and open-source codes have been developed [25]. Moreover, the algorithmic implementation and numerical efficiency aspects of this method have been extensively studied [26]. Due to its relative robustness and efficiency, XFEM is also used in industrial applications [27, 28] and has been implemented in commercial numerical simulation software

[29–31].

There is in particular a growing interest in modeling fracture mechanics with enrichment functions combined with meshless methods [32–34], or isogeometric analysis [35]. Advantages of the resulting methods include the possibility to model exactly curved boundaries through higher order shape functions. The resulting basis functions also have higher continuity, which is particularly advantageous when the physical model problem requires higher continuity, such as the Kirchhoff-Love theory. Also in some enriched meshless methods, no explicit representation of the crack’s topology is needed as this is handled through cracking particles as in [36] or weight-function enrichments as in [37, 38]. The cracking particles method introduces crack segments through the entire domain of influence of cracked nodes. They do not require any representation of the crack surface and crack branching and crack coalescence is a natural outcome of the simulation. However, the crack kinematics is not as accurate as in XFEM.

In all of these methods, a discontinuity is incorporated in the displacement field or geometry either through the mesh or through the approximation space. One key challenge of such methods is describing the crack geometry and tracking the paths of the cracks as the fracture progresses. This becomes increasingly challenging for complex structures and domain geometries. In general these numerical approximations track the evolution of the fracture during the simulations but they have shown to be inefficient regarding, for example, crack branching in three dimensional applications. Moreover, ill-conditioned systems are obtained due to addition of extra degrees of freedom into the displacement field. Although, some preconditioning methods have been introduced to alleviate this issue [39, 40], the computational cost of these methods is quite high.

1.3 Continuous fracture models

Besides the discrete models that has been gaining popularity over the last decade, continuous descriptions of fracture in solids have been recently presented which are based on an energy approach of fracture, such as continuum damage models [41, 42] and variational regularized model of Griffith’s fracture [43]. In these approaches, discontinuities are not introduced into the displacement field. Therefore, special treatment of cracks tip singularities, such as computing the stress intensity factors for predicting the crack path, are not needed. These methods do not require a representation of the crack surface which reduces complexity. Phase-field approaches for fracture [43] are such an alternative to the above mentioned discrete crack methods, as they do not require an explicit representation of the crack surface or separate crack tracking algorithms. The

crack surface is obtained as part of the solution and it is represented by an indicator function that is equal to 0 on the crack surface and 1 away from the fracture zone. In recent years, phase-field methods are widely used in science and engineering to model a variety of physics problems [44–47]. The predecessors of phase-field approaches to fracture can be traced back to 1998 in [48, 49], where the brittle crack propagation problem was regularized and recast as a minimization problem. In this model, the proposed energy functional is closely similar to the potential functional presented by Mumford and Shah [50], which has been used in image segmentation. The existence of solution to the Mumford-Shah functional minimization was proven by Ambrosio in [51]. In [52], an approximation by an elliptic functional defined on Sobolev spaces was developed, based on the theory of Γ -convergence. Later on, Bourdin introduced image segmentation based on a finite element method in [53].

In the phase-field approach a continuous field governed by a partial differential equation is used to model the cracks and their evolution. No evaluation of the stress intensity factors is necessary and this method naturally deals with complex crack geometries. Its main drawback is higher computational cost of solving a coupled PDE system. In this method, the crack zone is controlled by a regularization parameter. As this regularization parameter converges to zero, the phase field model converges to a discrete crack model.

Of particular importance to the modeling of practical engineering problems are thin shell formulations. Despite the advances made in simulating fracture for solids [54, 55], fracture in shell structures such as in an entire wing of an aircraft – remains a challenge due to the complex relation between the cracks and the shell kinematics and geometry. Because the physical dimension is reduced (i.e. from 3D to 2D), the computational resources are drastically reduced. Thin shell models are used in the design of new cars and aircraft in impact simulations. Non-propagating cracks in plates and shells have been modeled with partition- of-unity methods [56–58], but these approaches have been restricted to simple geometries. The majority of the formulations are based on Mindlin-Reissner theory [59]. There are comparatively fewer methods considering fracture in thin shells [60]. In [61–63], some meshfree thin shell models for static and dynamic fracture were presented. Furthermore, many of the approaches are applied to simple geometries such as plates, or spherical and cylindrical geometries [64–67]. Recently, nonlinear manifold learning techniques have been used to parametrize 2D sub-domains of a point-set surface, which are then used as parametric patches and joined together with a partition of unity. This method is able to model shells with complex geometry and topology structures [3, 68]. In [69], a shell element based on discrete Kirchhoff

theory was proposed assuming through-the-thickness cracks. Later, a shell model with the phantom node method based on edge rotations was proposed [66] for both thin and thick shells, where the crack tip can be located inside an element. A method based on subdivision shell elements and modeling the fracture along the element edges with a cohesive law was proposed in [70]. Most of above methods are based on discrete crack models that require explicitly tracking the crack path. Towards a more general, flexible and robust methodology to deal with fracture in Kirchhoff-Love shells, we propose modeling fracture with a phase-field model and discretizing the coupled thin-shell/phase-field equations with a meshfree method developed recently for manifolds of complex geometry and topology [3, 68].

1.4 Local Maximum Entropy (LME) approximants

The main objective of this thesis is to study fracture with local maximum entropy approximations and model fracture in thin shell structures with complex geometry and topology. In order to achieve this goal, in the first part of this dissertation, we study numerical methods to model discrete fracture in solid. We propose a coupling of the LME shape functions with the extrinsic enrichments used in partition of unity enriched methods for fracture, such as the extended finite element method (XFEM), see [62, 71, 72]. The LME shape functions are based on the principle of maximum entropy, which gives them optimal properties with respect to the uncertainty in the approximation. They are also very smooth (C^∞ - continuous), non-negative, which improves stability, and they possess a weak Kronecker delta property which makes it easy to impose the boundary conditions. With a fixed area (geometric) enrichment, optimal convergence is obtained. The LME basis functions are in general not polynomials but rather particle-based smooth functions, whose support is dictated by a non-dimensional parameter γ . When γ takes on large values, the LME shape functions asymptotically approach the FEM shape function (while maintaining C^∞ - continuity). On the other hand, when γ decreases, the LME shape functions have better approximation properties compared to standard FEM shape functions, but the size of their support increases. Hence, accurate numerical integration using standard Gauss quadrature requires a greater number of function evaluations. We observed that there is an optimal value of γ of around 1.8 that maximizes the accuracy in relation to computational cost. Moreover, this method is more accurate than standard XFEM and does not require the so-called blending elements (the elements near the crack tip). When compared to usual meshfree methods for crack propagation, such as Element Free Galerkin (EFG), the method presented

here, which satisfies the weak kronecker delta property, can more easily deal with essential boundary conditions. Moreover, smooth and non-negative basis functions, such as those in isogeometric analysis or LME approximations are gaining importance in recent research. We also, studied phase field models for the solid structures. This approach offers new perspectives for creating theoretical and computational models that can deal with complex fracture patterns. The discrete crack methods, such as XLME, seem less efficient in 3D applications with complex crack branching. All of the discrete crack methods need a considerable amount of additional algorithmic structure in these cases. Conversely, phase field method can be implemented in a straightforward manner to model complex crack branching. Furthermore, for the phase field method the extension of 2D algorithmic to 3D is straightforward. Complex crack patterns in 3D can be modeled without significant changes in the algorithmic structure for sufficiently fine mesh resolutions. We also developed a higher-order phase field model for fracture. The reason is that a second order phase field model is not as accurate as previously considered methods for modelling fracture. A higher-order phase field can take advantage of the increased regularity of the LME shape functions to deliver more accurate results. However, we observed that some particular problems, by using appropriate γ for the second order phase field model, we get almost the same accuracy as the fourth order phase field model. The advantage of using the second order phase field model is related to the computational cost. The second order phase field model with $\gamma \geq 4.8$ is much faster than the fourth order phase field model with $\gamma \leq 1.8$. Hence, we conclude that using the second order or the fourth order phase field models is problem dependent.

1.5 Contributions and Organization

The principal goal is to develop computationally efficient fracture model with LME approximants in order to model fracture in thin shell structure with complex geometry and topology. For this purpose, we have studied the LME shape functions, the statistical manifold learning technique that allow dealing with general point set surfaces avoiding a global parametrization, the extended LME method and the phase field method to model fracture with complex crack branching. Coupling the phase-field method, which can model completely arbitrary cracks, with this new geometric methods for thin shell structures will enable us to deal with fracture of complex thin shell structures. In fact, this framework is sufficiently realistic that it could be directly validated by comparison with experimental data.

During the course of the work, it was realized that many substantially different problems have to be solved in order to approach the global goal. Therefore, the associated objectives along with the outline of presentation can be listed as follows: In the chapter 2, we briefly describe the LME approximants. In the chapter 3, we introduce the coupling between LME and partition of unity enrichment functions, with particular reference to implementation issues such as numerical integration. Next we examine the accuracy of the method through several numerical examples, showing optimal convergence rates for the energy norm of the error and stress-intensity factors can be achieved. In the chapter 4 we introduce the general theory and motivation for the second and fourth order phase field models. In this chapter, the convergence rate and the error of modeling of the fourth order model are compared to the second order model. Also, the continuum formulation of an elastic body with phase field model, is presented. Finally, we demonstrate the capabilities of the method through some numerical examples. We indicate that it is straightforward to extend $2D$ examples to $3D$. In the chapter 5 modeling fracture in thin shell structures with complex geometry and topology is presented. In the section 5.1 some dimensionality reduction methods are mentioned. The section 5.2 describes the representation of general surfaces represented by a set of scattered points [3]. In the section 5.3, we review the Kirchhoff–Love theory of thin shells. In this section, we introduce a phase-field model for fracture in thin shells. The Galerkin discretization is also presented in this section. In the section 5.4 we demonstrate the capabilities of the method through a numerical example to capture cracks in thin shell structure with complex geometry and topology. Chapter 6 contains concluding remarks and some possibilities for future work.

Chapter 2

Local Maximum entropy approximants

Maximum entropy shape functions are a relatively new class of approximation functions, as they were first introduced in [73] in the context of polygonal interpolation. The idea of these functions is to maximize the Shannon entropy [74] of the basis functions, which gives a measure of the uncertainty in the approximation scheme. The principle of maximum entropy (max-ent) was developed by Jaynes [75, 76], who showed that there is a natural correspondence between statistical mechanics and information theory. In particular, max-ent offers the least-biased statistical inference when the shape functions are viewed as probability distributions subject to the approximation constraints (such as linear reproducing properties). However, without additional constraints, the basis functions are non-local, which due to increased overlapping makes them unsuitable for analysis using Galerkin methods. The large overlapping of the basis functions, generally leads to more expensive numerical integration schemes due to large number of evaluation points. It also produces non-sparse stiffness matrix which require significantly more computational resources to solve.

The local maximum-entropy (LME) approximation schemes were developed in [77] using a framework similar to meshfree methods. Here the support of the basis functions is introduced as a thermalization (or penalty) parameter β in the constraint equations. When $\beta = 0$, then the max-ent principle is fully satisfied and the basis functions will be least biased. For example, if only zero-order consistency is required, the shape functions are Shepard approximants [78] with Gaussian weight function. When β is large, then the shape functions have minimal support. In particular, they become the usual linear finite element functions defined on a Delaunay triangulation of the domain

associated with the given node set. In [77] it was shown that for some values of β , the approximation properties of the maximum-entropy basis functions are greatly superior to those of the finite element linear functions, even when the added computational cost due to larger support is taken into account.

Subsequent studies, such as [79–81], show that maximum entropy shape functions are suitable for solving a variety of problems such as thin shell analysis, compressible and nearly-incompressible elasticity and incompressible media problems. Higher order approximations can also be obtained using the max-ent framework, as shown in [82]. This class of methods is therefore related to the MLS-based meshless methods (due to the node-based formulation) and isogeometric analysis (with whom it shares features such as weak Kronecker delta and non-negativity), inheriting some advantages from both.

2.1 Local Maximum entropy shape functions

LME meshfree approximants, introduced in [77], are related to other convex approximation schemes, such as natural neighbor approximants [83], subdivision approximants [84], or B-spline and NURBS basis functions [?]. The LME basis functions will be denoted by $p_a(\mathbf{x})$, $a = 1, \dots, N$ with $\mathbf{x} \in \mathbb{R}^d$, d is the dimension of the physical domain. They are non-negative and are required to satisfy the zeroth-order and first-order consistency conditions:

$$p_a(\mathbf{x}) \geq 0, \tag{2.1}$$

$$\sum_{a=1}^N p_a(\mathbf{x}) = 1, \tag{2.2}$$

$$\sum_{a=1}^N p_a(\mathbf{x}) \mathbf{x}_a = \mathbf{x}. \tag{2.3}$$

In the last equation, the vector \mathbf{x}_a identifies the positions of the nodes associated with each basis function. Consider a set of nodes $X = \{\mathbf{x}_a\}_{a=1, \dots, N}$, which we will call *the node set*. The convex hull of X is the set

$$\text{conv}X := \{\mathbf{x} \in \mathbb{R}^d \mid \mathbf{x} = \mathbf{X}\lambda, \lambda \in \mathbb{R}_+^N, \mathbf{1} \cdot \lambda = 1\} \tag{2.4}$$

Here \mathbb{R}_+^N is the non-negative orthant, $\mathbf{1}$ denotes the vector in \mathbb{R}^N whose entries are one, and \mathbf{X} is the $d \times N$ matrix whose columns are the co-ordinates of the position vectors

of the nodes in the node set X [77]. Convex approximants, which are in the span of convex basis functions, can only exist within the convex hull of X (or subsets of it) and satisfy a weak Kronecker delta property at the boundary of the convex hull of the nodes. This means that the shape functions corresponding to the interior nodes vanish on the boundary. With this property, the imposition of essential boundary conditions in the Galerkin method is straightforward.

The principle of maximum entropy comes from statistical physics and information theory, which consider the measure of uncertainty or information entropy [74]. Consider a random variable $\chi : I \rightarrow \mathbb{R}^d$, where I is the index set $I = \{1, \dots, N\}$ and $\chi(a) = \mathbf{x}_a$ gives to each index the position vector of its corresponding node. Since the shape functions of a convex approximation scheme are non-negative and form a partition of unity, we regard $\{p_1(\mathbf{x}), \dots, p_N(\mathbf{x})\}$ as the corresponding probabilities. The statistical expectation or average of this random variable, as seen from equation (2.3), is \mathbf{x} . According to this interpretation, the approximation of a function $u(\mathbf{x}) \approx \sum_{a=1}^N p_a(\mathbf{x}) u_a$ from the nodal values $\{u_a\}_{a=1, \dots, N}$ is understood as an expected value $u(\mathbf{x})$ of a random variable $\mu : I \rightarrow \mathbb{R}$ where $\mu(a) = u_a$. A first question of interest is whether there exist shape functions consistent with the constraints. From the convex hull meaning the following theorem holds [85].

Theorem 1. *There is a discrete distribution having the probabilities $\{p_1(\mathbf{x}), \dots, p_N(\mathbf{x})\}$ that satisfies the constraints 2.1, 2.2 and 2.3 if and only if $\mathbf{x} \in \text{conv}X$.*

The main idea of max-ent is to maximize the Shannon's entropy, $H(p_1, p_2, \dots, p_N)$, subject to the consistency constraints as follows:

(ME) For a fixed \mathbf{x} maximize (2.5)

$$H(p_1, p_2, \dots, p_N) = - \sum_{a=1}^N p_a \log(p_a)$$

subject to $p_a \geq 0, \quad a = 1, \dots, N$

$$\sum_{a=1}^N p_a = 1$$

$$\sum_{a=1}^N p_a \mathbf{x}_a = \mathbf{x}.$$

The existence and uniqueness of the solution of this program are established by the following Theorem.

Theorem 2. *There exists a max-ent distribution for the program (2.5) if and only if $\mathbf{x} \in \text{conv}X$, and the solution is unique.*

Solving the (ME) problem produces the set of basis functions, $p_a := p_a(\mathbf{x}), a = 1, \dots, N$. However, these basis functions are non-local, i.e. they have support in all of $\text{conv}X$, and are not suitable for use in a Galerkin approximation because it would lead to a full, non-banded matrix. In addition, the max-ent approximation is far from interpolating in the interior, and results in a very poor fit to the given data as illustrated in [77]. Nevertheless, they have been used in [73] as basis functions for polygonal elements.

Another optimization problem which takes into account the locality of the shape functions is Rajan's form of the Delaunay triangulation [86]. This can be stated as the following linear program:

(RAJ) For a fixed \mathbf{x} minimize (2.6)

$$\begin{aligned}
 U(\mathbf{x}, p_1, p_2, \dots, p_N) &= \sum_{a=1}^N p_a |\mathbf{x} - \mathbf{x}_a|^2 \\
 \text{subject to } p_a &\geq 0, \quad a = 1, \dots, N \\
 \sum_{a=1}^N p_a &= 1 \\
 \sum_{a=1}^N p_a \mathbf{x}_a &= \mathbf{x}
 \end{aligned}$$

Theorem 3. *The program (RAJ) has unique solution if and only if $\mathbf{x} \in \text{conv}X$ and nodes in X are in general positions.*

It is easy to see that $U(\mathbf{x}, p_1, p_2, \dots, p_N)$ is minimized when the shape functions p_1, \dots, p_N decay rapidly as the distance from the corresponding nodes \mathbf{x}_a increases. There, the shape functions that satisfy (RAJ) problem will have small supports, where the support can be defined up to a small tolerance ϵ by

$$\text{supp}(p_a) = \{\mathbf{x} : p_a(\mathbf{x}) > \epsilon\}$$

The main idea of LME approximants is to compromise between the (ME) problem and the (RAJ) problem by introducing parameters β_a that control the support of the p_a .

Therefore we write:

$$\begin{aligned}
 &\text{For a fixed } \mathbf{x} \text{ minimize} && (2.7) \\
 f_{\beta_a}(\mathbf{x}, p_1, p_2, \dots, p_N) &= \sum_{a=1}^N \beta_a p_a |\mathbf{x} - \mathbf{x}_a|^2 + \sum_{a=1}^N p_a \log(p_a) \\
 &\text{subject to } p_a \geq 0, \quad a = 1, \dots, N \\
 &\sum_{a=1}^N p_a = 1 \\
 &\sum_{a=1}^N p_a \mathbf{x}_a = \mathbf{x}
 \end{aligned}$$

Since for $\beta \in [0, +\infty)$ the function $f_{\beta_a}(\mathbf{x}, \cdot)$ is continuous and strictly convex in the domain of $\{p_1(\mathbf{x}), \dots, p_N(\mathbf{x})\}$ or feasible set, an identical theorem to that in Theorem (2) states that LME program has a unique solution if and only if $\mathbf{x} \in \text{conv}X$. The non-negative parameters β_a can in general be functions of the position \mathbf{x} . This convex optimization problem is solved efficiently by a duality method as described in [77]. Finally, the shape functions are written in the form:

$$p_a(\mathbf{x}) = \frac{1}{Z(\mathbf{x}, \lambda^*(\mathbf{x}))} \exp[-\beta_a |\mathbf{x} - \mathbf{x}_a|^2 + \lambda^*(\mathbf{x}) \cdot (\mathbf{x} - \mathbf{x}_a)]$$

where

$$Z(\mathbf{x}, \lambda) = \sum_{b=1}^N \exp[-\beta_b |\mathbf{x} - \mathbf{x}_b|^2 + \lambda \cdot (\mathbf{x} - \mathbf{x}_b)]$$

is a function associated with the node set X and $\lambda^*(\mathbf{x})$ is defined by

$$\lambda^*(\mathbf{x}) = \arg \min_{\lambda \in \mathbb{R}^d} \log Z(\mathbf{x}, \lambda)$$

This optimization problem is efficiently solved with Newton Raphson's method.

The local max-ent shape functions are as smooth as $\beta(\mathbf{x})$ and $p_a(\mathbf{x}, \beta_a)$ is a continuous function of $\beta \in [0, +\infty)$ [77]. For example LME shape functions are C^∞ if β is constant. In this dissertation we choose $\beta = \frac{\gamma}{h^2}$, where h is a measure of the nodal spacing and γ is constant over the domain. In this case the shape functions are smooth and their degree of locality is controlled by the parameter γ . A plot of the LME functions for $\gamma = 1.8$ and a particular choice of nodes is given in Figure 2.1. In general, the optimal β is not obvious and this will be discussed later in this work.

As we mentioned before, LME shape functions satisfy a weak Kronecker delta prop-

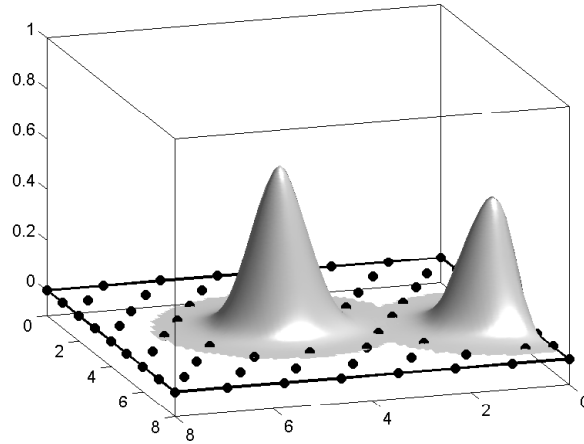


Figure 2.1: Local max-ent shape functions in 2D.

erty at the boundary of the convex hull of the nodes. Therefore, the shape functions that correspond to interior nodes vanish on the boundary. This property makes it easy to impose the boundary conditions. In the last chapter, we indicate how the smoothness property of these shape functions can be used to model structures with complex geometry and topology.

Chapter 3

Extended Local Maximum entropy method

Fracture can be studied from many scales related to the field of the application, for instance at the atomic level and at the scale of the microstructure of the material. From the engineering point of view, the material is treated as a continuum and it is desired to predict and model fracture through the analysis of stress, strain and energy. In this dissertation, we consider this engineering point of view and follow the continuum and fracture mechanics formulations in solid.

3.1 Basic Fracture Mechanics Concepts

In 1956, Irwin used the Westergaard approach to develop the concepts that were introduced by Griffith in 1920. According to the Westergaard [87], Irwin [88], Sneddon [89] and Williams's work [90], linear elastic theory predicts that the stress distribution σ_{ij} tensor round the crack tip, in polar coordinates (r, θ) with origin at the crack tip, has the form

$$\sigma_{ij}(r, \theta) = \frac{K}{\sqrt{2\pi r}} f_{ij}(\theta) + \text{higher order terms} \quad (3.1)$$

where K is the stress intensity factor and $f_{ij}(\theta)$ is a dimensionless quantity that varies with the load and geometry. Fracture mechanics theories have been developed to account for various types of nonlinear material behavior and dynamic effects. All of these recent methods are extensions of linear elastic fracture mechanics. So, here we focus on the theory of linear elastic fracture mechanics (LEFM). Regarding stress analysis point of view, there are three types of loading that a crack can experience (a) Opening, mode I: The crack surfaces separate symmetrically with respect to the

planes xy and xz . (b) Sliding, mode II: The crack surfaces slide relative to each other symmetrically with respect to the plane xy and skew-symmetrically with respect to the plane xz . (c) Tearing, mode III: The crack surfaces slide relative to each other skew-symmetrically with respect to both planes xy and xz . The stress intensity factors are usually given a subscript to denote the mode of loading; i.e., K_I , K_{II} and K_{III} , which are called the Mode I, Mode II and Mode III stress intensity factors. Stress intensity factors are local parameters of fracture behavior which qualify the stresses, strains and displacements around the crack tip. Stress intensity factors are useful instruments for analysis the discrete descriptions of fracture numerical methods which incorporate a discontinuity into the displacement field or geometry, such as the extended finite element method (X-FEM) [14], the cohesive zone methods [91, 92], and the cohesive segments method [93].

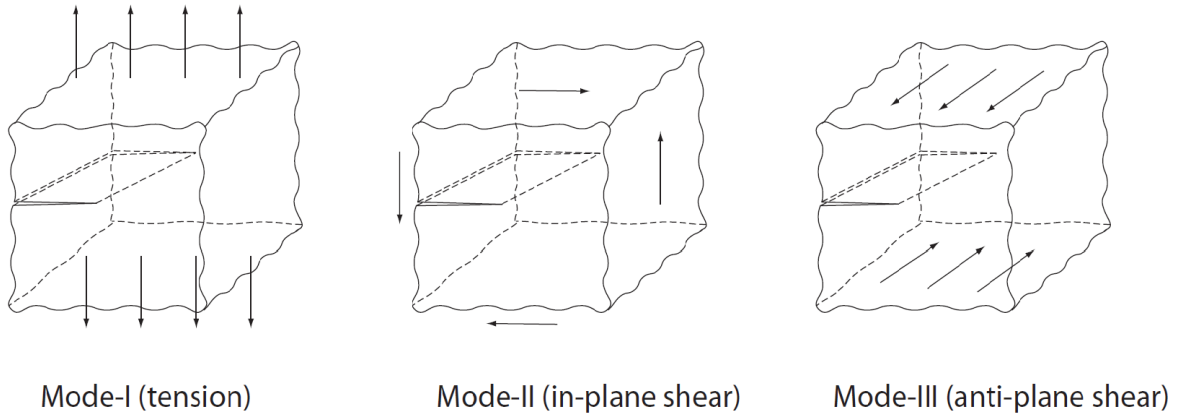


Figure 3.1: Signed distance function.

3.2 Extrinsic enrichments for Partition of Unity Methods

In this section, we focus on discrete methods of modeling cracks. As we mentioned in the introduction chapter, in these methods the discontinuity is introduced to the displacement field by means of remeshing or by enriching the basis by inserting discontinuities using the partition of unity method proposed by Babuška and Melenk [16]. The enrichment is aimed to increase the accuracy of approximation by including information of the analytical solution. The main idea of Partition of Unity (PU) enrichment as used here is to extend the basis approximation space with some additional enrichment

functions, such that it is able to reproduce certain features of the problem of interest, e.g. cracks. The proposed method here is based on a local partition of unity and uses an extrinsic enrichment to model the discontinuity. So, the LME approximation can be decomposed into a standard part and an enriched part:

$$u^h(\mathbf{x}) = \sum_{I \in W} p_I(\mathbf{x})u_I + \sum_{J \in W_b} p_J(\mathbf{x})\chi(\phi_J(\mathbf{x}))a_J + \sum_{K \in W_s} p_K(\mathbf{x}) \sum_{k=1}^4 B_k(\mathbf{x})b_{kK}$$

Here the first term is the standard approximation part and the second and the third terms are the enriched parts. W is the set of nodes in the entire discretization and W_b and W_s are the sets of enriched nodes. p_I are the shape functions and χ and B_k are the enrichment functions. Normally, χ is selected as a step or Heaviside function and is used to enrich the nodes where the supports of the LME shape functions are completely cut by crack. B_k are branch functions and are used to enrich the shape functions whose supports include the crack tip. In this work we use a geometric (fixed area) enrichment, and therefore we obtain optimal convergence rate ($O(h^2)$) without a special treatment of the so-called "blending" area around the crack tip. Branch functions are defined as follows (in polar coordinate relative to the crack tip):

$$\begin{aligned} B_1(r, \theta) &= \sqrt{r} \sin \frac{\theta}{2} \\ B_2(r, \theta) &= \sqrt{r} \cos \frac{\theta}{2} \\ B_3(r, \theta) &= \sqrt{r} \sin \frac{\theta}{2} \cos \theta \\ B_4(r, \theta) &= \sqrt{r} \cos \frac{\theta}{2} \cos \theta \end{aligned}$$

Where $r = \|\mathbf{x} - \mathbf{x}^{tip}\|$.

$\phi(\mathbf{x})$ is the signed distance from the point \mathbf{x} to the crack segment and a_I and b_{kI} are additional degrees of freedom [94]. The signed distance function is defined as:

$$\phi(\mathbf{x}) = \min_{\mathbf{x}_\Gamma \in \Gamma} \|\mathbf{x} - \mathbf{x}_\Gamma\| \text{sign}(\mathbf{n} \cdot (\mathbf{x} - \mathbf{x}_\Gamma))$$

Here Γ is the curve of discontinuity, \mathbf{x}_Γ is an arbitrary point on Γ and \mathbf{n} is normal vector to Γ (see Figure 2). If we choose χ as a Heaviside function, then

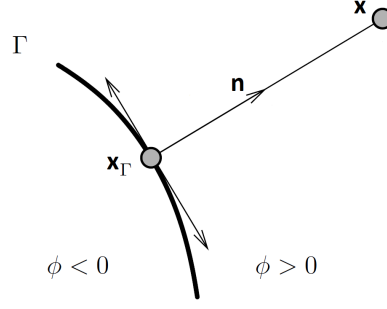


Figure 3.2: Signed distance function.

$$H(\phi(\mathbf{x})) = \begin{cases} 1 & \text{if } \phi(\mathbf{x}) > 0 \\ -1 & \text{if } \phi(\mathbf{x}) < 0 \end{cases} \quad (3.2)$$

This enrichment function captures the jump across the crack faces.

In order to model any curved crack, the signed distance function can be approximated by the same shape functions as the displacement. Assume t is a vector tangent to the curved crack, which its direction is to the crack curve. We approximate ϕ by:

$$\tilde{\phi}(\mathbf{x}) = \sum_I p_I(\mathbf{x}) \phi_I, \quad \mathbf{x} \in \Omega_\phi \quad (3.3)$$

Where ϕ_I are the nodal values of ϕ , p_I are the shape functions and Ω_ϕ , is the domain of definition for ϕ , which is defined by:

$$\Omega_\phi := \{\mathbf{x} | t \cdot \nabla r(\mathbf{x}) > 0\} \quad (3.4)$$

So, the approximated crack position is considered as:

$$\Gamma := \{\mathbf{x} | \tilde{\phi}(\mathbf{x}) = 0, \mathbf{x} \in \Omega_\phi\} \quad (3.5)$$

In this case, $\tilde{\phi}(\mathbf{x})$ is not defined beyond the crack tips. So, two possibilities are considered for the angle θ of the Branch functions. If $t \cdot \nabla r \leq 0$, then the regular polar angle from $-t$ is computed. If $t \cdot \nabla r > 0$, θ is considered as [95]:

$$\theta = \arctan\left(\frac{-\phi}{\sqrt{r^2 - \phi^2}}\right) \quad (3.6)$$

3.3 Numerical Examples

3.3.1 Infinite plate with a horizontal crack

Consider an infinite plate containing a straight crack of length $2a$ under a remote uniform stress field σ as shown in Figure 5. The analytical solution near crack tip for stress fields and displacement in terms of local polar coordinates from the crack tip are [32]

$$\begin{aligned}\sigma_{xx}(r, \theta) &= \frac{K_I}{\sqrt{r}} \cos \frac{\theta}{2} \left(1 - \sin \frac{\theta}{2} \sin \frac{3\theta}{2} \right) \\ \sigma_{yy}(r, \theta) &= \frac{K_I}{\sqrt{r}} \cos \frac{\theta}{2} \left(1 + \sin \frac{\theta}{2} \sin \frac{3\theta}{2} \right) \\ \sigma_{xy}(r, \theta) &= \frac{K_I}{\sqrt{r}} \sin \frac{\theta}{2} \cos \frac{\theta}{2} \cos \frac{3\theta}{2} \\ \\ u_x(r, \theta) &= \frac{2(1+\nu)}{\sqrt{2\pi}} \frac{K_I}{E} \sqrt{r} \cos \frac{\theta}{2} \left(2 - 2\nu - \cos^2 \frac{\theta}{2} \right) \\ u_y(r, \theta) &= \frac{2(1+\nu)}{\sqrt{2\pi}} \frac{K_I}{E} \sqrt{r} \sin \frac{\theta}{2} \left(2 - 2\nu - \cos^2 \frac{\theta}{2} \right)\end{aligned}\tag{3.7}$$

where $K_I = \sigma\sqrt{\pi a}$ is the stress intensity factor, ν is Poisson's ratio and E is Young's modulus. The analytical solution is valid for a region close enough to the crack tip. We consider a square ABCD of length $10 \text{ mm} \times 10 \text{ mm}$, $a = 100 \text{ mm}$, $E = 10^7 \text{ N/mm}^2$, $\nu = 0.3$, $\sigma = 10^4 \text{ N/mm}^2$ and the modeled crack length is 5 mm . In all problems of this chapter, plane strain state is assumed. We use Dirichlet boundary conditions on the bottom, right and top edges and Neumann boundary conditions on the left edge which includes the crack. As we mentioned in Section 2, LME shape functions satisfy a weak Kronecker delta property. This property allows us to impose Dirichlet boundary conditions by computing a node-based interpolant or an L^2 projection of the boundary data. The latter can also be used for edges that contain enriched nodes. Numerical integration is performed on a background mesh of rectangular elements and the almost polar integration is used on the elements containing a crack tip. The error in the energy norm is illustrated in Figure 3.4 for different values of γ and Figure 3.5 shows the percentage error for stress intensity factor (SIFs). It is obvious from these figures that in this case there is an optimal value for the parameter γ of around 1.8 for which accuracy is maximized. For very low values of γ , convergence is degraded. This is due to numerical integration. With a higher number of Gauss points and

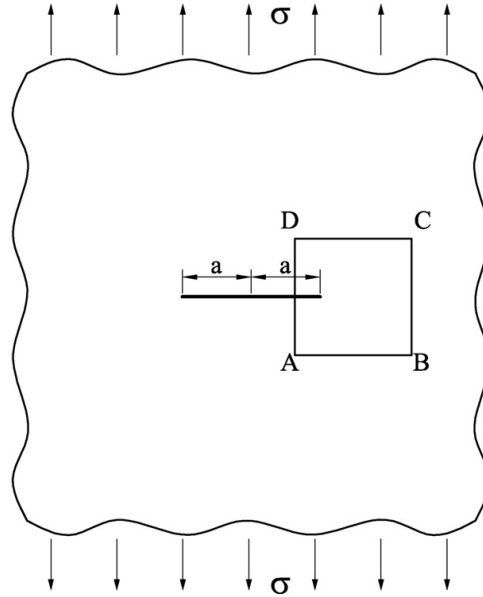


Figure 3.3: Infinite plate with a center crack under uniform tension and modeled geometry ABCD.

$\gamma = 0.8$, the optimal rate of convergence for a plane elasticity problem was recovered in [77]. But in that case, the method is very expensive. The LME results converge to the standard XFEM results as γ increases. As shown in Figure 3.4, the rate of convergence for different values of γ , the parameter that controls the support of the shape functions, is about 1. For a fixed number of nodes, when γ decreases the error also decreases. For example, for $n = 36 \times 36$ we see from Table 3.1 that the error becomes smaller as γ decreases to 0.8. However, as γ decreases, because the support of the LME shape functions becomes larger, we also need to consider a larger radius of

Table 3.1: Error for energy norm and SIF together with the running time and efficiency ratio (3.8) for a problem discretized with 36×36 nodes.

Method	XFEM	$\gamma = 4.8$	$\gamma = 3.8$	$\gamma = 2.8$	$\gamma = 1.8$	$\gamma = 0.8$
Rad. of Infl.	1	2	2	3	3	6
Energy error	0.04611	0.04532	0.04161	0.03160	0.01752	0.00640
SIF error	0.08822	0.08474	0.07020	0.03979	0.01016	0.00226
Assembly time	7.0	25.7	26.0	58.0	64.8	226.9
Solution time	0.4	1.4	1.7	2.9	2.9	7.9
Post-proc. time	8.0	21.5	20.7	36.7	36.0	103.6
Total time	15.4	48.5	48.4	97.6	103.7	338.4
Efficiency (energy)	1.000	0.322	0.352	0.230	0.390	0.327
Efficiency (SIF)	1.000	0.329	0.399	0.349	1.288	1.770

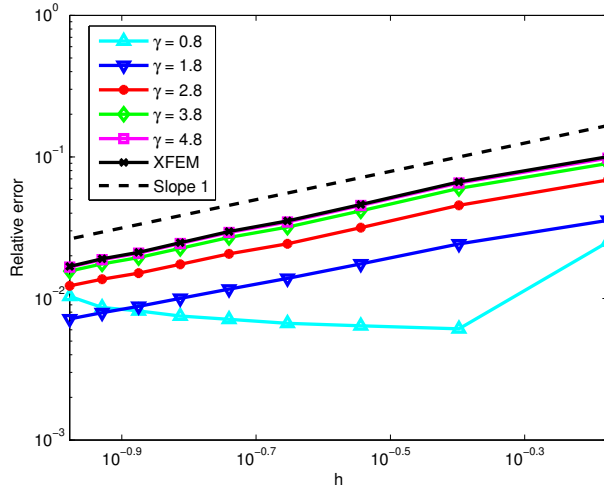


Figure 3.4: Error in the energy norm for the horizontal crack problem in mode I.

influence (the distance of the neighbor search between the nodes), which leads to more function evaluations and increases the computational cost. In this study, we found that choosing $\gamma = 1.8$, which corresponds to a radius of influence of 3 nodes, provides a reasonable balance between accuracy and computational cost.

We note from Table 3.1 that LME is significantly slower than XFEM for the same number of nodes, and that the computational cost increases as γ decreases due to larger radius of influence. However, especially for $\gamma = 1.8$, the method is much more accurate than XFEM, which makes up for some of the added computational cost. This is particularly true for the computation of the stress intensity factor, where the error is almost 9 times smaller (although the method is 7 times slower). For $\gamma = 0.8$ and 36×36 nodes the method is even more accurate, but unfortunately as was discussed before, the method becomes prohibitively expensive.

In Table 3.1, we also show the computational efficiency of the method which we define by:

$$\text{efficiency} = \frac{\% \text{ improvement in accuracy}}{\% \text{ increase in total computational time}} \quad (3.8)$$

We note that an efficiency index of 1 indicates the method is as efficient as XFEM, an index greater than 1 indicates the method is more efficient than XFEM, and an index less than 1 indicates the method is less efficient. Because of the additional overhead required (Newton iterations, neighbor node search, less-sparse stiffness matrix), XLME in the current implementation is generally less efficient than XFEM. The ratios showed in Table 3.1 are representative for any number of nodes and for the other model problems considered later in this chapter. In general, the results agree with other findings

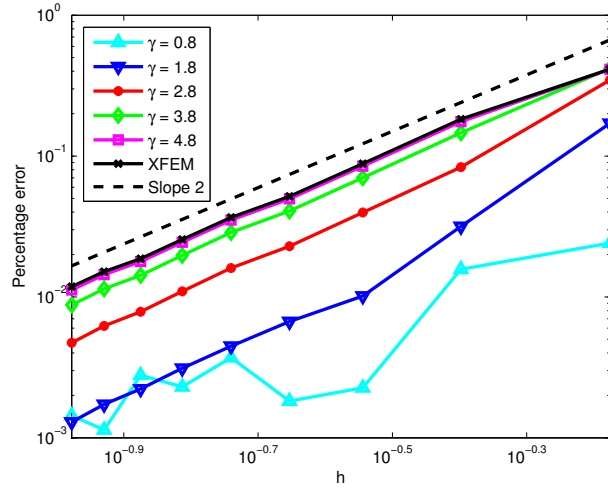


Figure 3.5: Percentage error of stress intensity factor for horizontal crack.

in literature, which show that LME is more efficient than MLS but less efficient than FEM [96].

We compute the stress intensity factors by the interaction integral method, where the domain form of the interaction integral is given by [14]

$$I^{(1,2)} = \int_A \left[\sigma_{ij}^{(1)} \frac{\partial u_i^2}{\partial x_1} - \sigma_{ij}^{(2)} \frac{\partial u_i^1}{\partial x_1} - W^{(1,2)} \delta_{1j} \right] \frac{\partial q}{\partial x_j} dA$$

The domain of integration, A , is set to be the union of all the elements which have a node within a ball of radius r_d around the crack tip (see Figure 8). Since we use a fixed area enrichment, r_d is also a fixed distance. We found that most accurate results are obtained when r_d is half of the modeled crack length. This results in a superconvergent ($O(h^2)$) rate for K_I , as also reported for XFEM in [29] and [97].

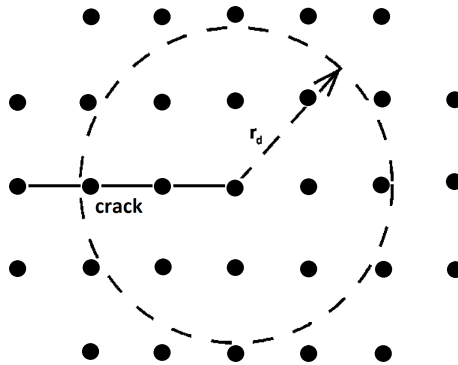


Figure 3.6: Elements which have a node within a ball of radius r_d around the crack tip.

The weight function q is taken to have a value of unity for all nodes within the ball r_d , and zero on the outside of the ball. Hence, the bilinear shape functions are used as the weight functions. $W^{(1,2)}$ is the interaction strain energy density

$$W^{(1,2)} = \sigma_{ij}^{(1)} \epsilon_{ij}^{(2)} = \sigma_{ij}^{(2)} \epsilon_{ij}^{(1)}$$

$\sigma_{ij}^{(1)}$ and $\epsilon_{ij}^{(1)}$ are computed stresses and strains and $\sigma_{ij}^{(2)}$ and $\epsilon_{ij}^{(2)}$ are auxiliary stresses and strains derived by Westergaard and Williams, corresponding to mode 1 and mode 2 as described in [14].

3.3.2 Edge crack under shear traction

The second problem investigated in this chapter, is a finite dimensional plate subjected to uniform shear on the top of the plate $\tau = 1.0 \text{ N/mm}^2$ and the bottom is fixed, as shown in the Figure 9. We choose Young's modulus $E = 3 \times 10^7 \text{ Pa}$ and Poisson's ratio $\nu = 0.25$.

The stress intensity factors K_I and K_{II} , are calculated by the extended LME method and compared to the reference solutions [98]:

$$K_I^{ref} = 34.0$$

$$K_{II}^{ref} = 4.55$$

We note that these values were calculated using a boundary collocation method and are given with an accuracy of 3 significant digits. The SIFs K_I and K_{II} calculated by the extended LME method on a fine mesh converge to the following values (accurate to 4 significant digits):

$$K_I^0 = 34.04$$

$$K_{II}^0 = 4.537$$

We note that there is a very good agreement between the reference solution and our computed solution. To study the convergence of the method we calculated the percentage error between the computed SIFs at various levels of refinement and K_I^0 and K_{II}^0 .

Figures 10 and 11 illustrate the percentage error for K_I and K_{II} . As evident from these figures, the smallest error for this problem is obtained by $\gamma = 1.8$ and $\gamma = 2.8$. We note that for these values of γ the error becomes less than 0.01%, which is equal to

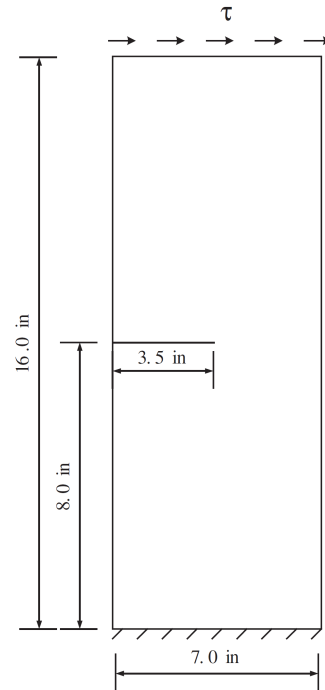
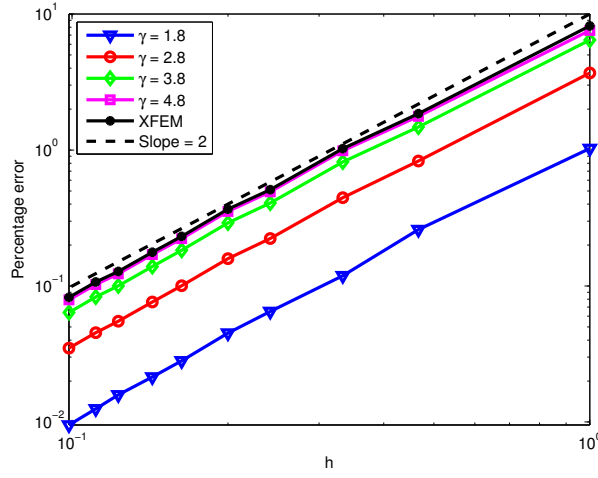
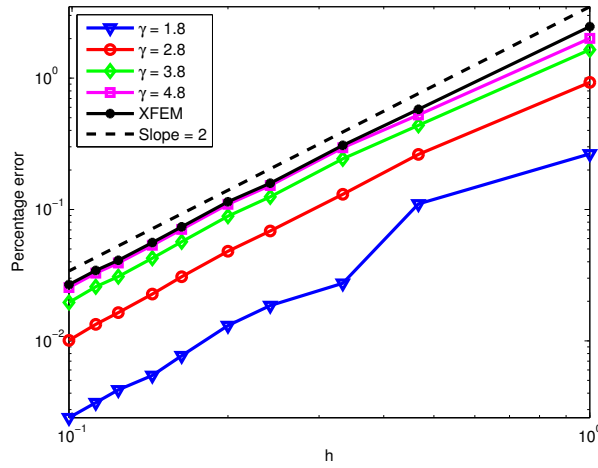


Figure 3.7: Edge-cracked plate under shear stress.

K_I^0 and K_{II}^0 up to the given significant digits. For values of γ that are lower than 1.8, computing the SIF accurately becomes expensive due to the large support of the shape functions. Therefore, we will not consider the case $\gamma = 0.8$ in the following examples.

3.3.3 Slanted crack in an infinite plate

Consider an infinite plate containing an angled crack as shown in Figure 12a. This problem is a mixed mode I-II problem. The analytical near-tip field solution for this

Figure 3.8: Percentage error of K_I for edge-cracked plate under shear stress.Figure 3.9: Percentage error of K_{II} for edge-cracked plate under shear stress.

problem in polar coordinates is given in [99]

$$\begin{aligned}
 \sigma_{xx}(r, \theta) &= \frac{K_I}{\sqrt{2\pi r}} \cos \frac{\theta}{2} \left(1 - \sin \frac{\theta}{2} \sin \frac{3\theta}{2} \right) \\
 &\quad - \frac{K_{II}}{\sqrt{2\pi r}} \sin \frac{\theta}{2} \left(2 + \cos \frac{\theta}{2} \cos \frac{3\theta}{2} \right) \\
 \sigma_{yy}(r, \theta) &= \frac{K_I}{\sqrt{2\pi r}} \cos \frac{\theta}{2} \left(1 + \sin \frac{\theta}{2} \sin \frac{3\theta}{2} \right) \\
 &\quad + \frac{K_{II}}{\sqrt{2\pi r}} \sin \frac{\theta}{2} \cos \frac{\theta}{2} \cos \frac{3\theta}{2} \\
 \sigma_{xy}(r, \theta) &= \frac{K_I}{\sqrt{2\pi r}} \sin \frac{\theta}{2} \cos \frac{\theta}{2} \cos \frac{3\theta}{2} \\
 &\quad + \frac{K_{II}}{\sqrt{2\pi r}} \cos \frac{\theta}{2} \left(1 - \sin \frac{\theta}{2} \sin \frac{3\theta}{2} \right)
 \end{aligned}$$

$$\begin{aligned}
u_x(r, \theta) &= \frac{K_I}{2\mu} \sqrt{\frac{r}{2\pi}} \cos \frac{\theta}{2} \left(\kappa - 1 + 2 \sin^2 \frac{\theta}{2} \right) \\
&\quad + \frac{K_{II}}{2\mu} \sqrt{\frac{r}{2\pi}} \sin \frac{\theta}{2} \left(\kappa + 1 + 2 \cos^2 \frac{\theta}{2} \right) \\
u_y(r, \theta) &= \frac{K_I}{2\mu} \sqrt{\frac{r}{2\pi}} \sin \frac{\theta}{2} \left(\kappa + 1 - 2 \cos^2 \frac{\theta}{2} \right) \\
&\quad - \frac{K_{II}}{2\mu} \sqrt{\frac{r}{2\pi}} \cos \frac{\theta}{2} \left(\kappa - 1 - 2 \sin^2 \frac{\theta}{2} \right)
\end{aligned}$$

Here μ is the shear modulus, $\kappa = 3 - 4\nu$ for plane strain. The angle θ and the distance r from the crack tip are indicated in Figure 12b. We redefine the x -coordinate axis

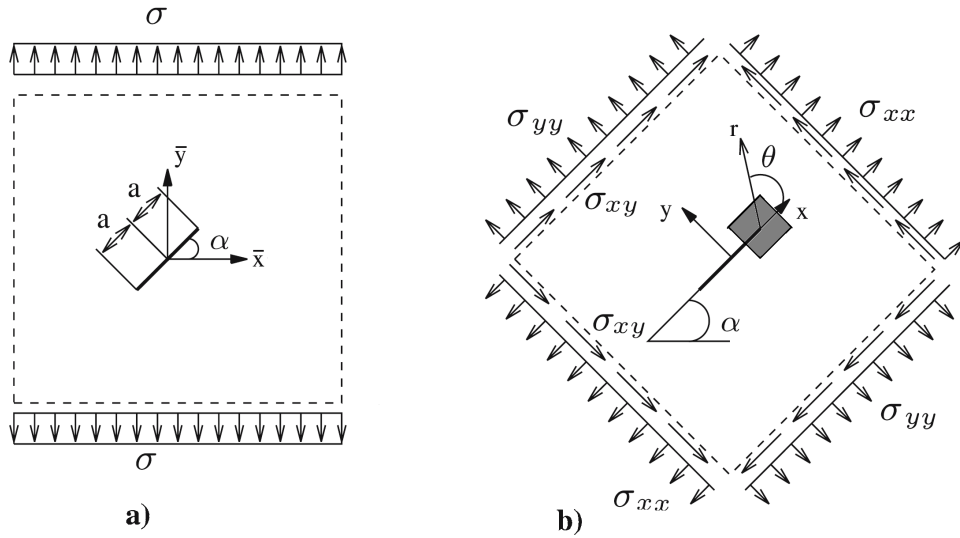


Figure 3.10: a) Slanted crack in an infinite plate where the principal stress is not perpendicular to the crack. b) An infinite plate rotated with respect to the crack's angle.

to coincide with the crack orientation [100], see Figure 12b. The applied stress is decomposed into normal and shear components. The stress normal to the crack, σ_{yy} , produces pure mode I loading, while σ_{xy} applies mode II loading to the crack. The stress intensity factors for the plate, can be computed by the relationship between σ_{yy} and σ_{xy} relative to σ and α through Mohr's circle [101]

$$\begin{aligned}
K_I &= \sigma_{yy} \sqrt{\pi a} = \sigma \cos^2 \alpha \sqrt{\pi a} \\
K_{II} &= \sigma_{xy} \sqrt{\pi a} = \sigma \sin \alpha \cos \alpha \sqrt{\pi a}
\end{aligned}$$

Table 3.2: Error and the average running time when the number of nodes is 36×36 , the number of Gauss points is 16, $\alpha = 15^\circ, 30^\circ$ and radius of influence is 2 for $\gamma = 4.8$ and $\gamma = 3.8, 3$ for $\gamma = 2.8$ and $\gamma = 1.8$

γ	Relative error of K_I , $\alpha = 15^\circ$	Relative error of K_{II} , $\alpha = 15^\circ$	Relative error of K_I , $\alpha = 30^\circ$	Relative error of K_{II} , $\alpha = 30^\circ$	Average total running time (seconds)
XFEM	0.088212	0.014660	0.088209	0.014663	15.7
4.8	0.084748	0.013936	0.084753	0.013924	49.0
3.8	0.070224	0.011169	0.070251	0.011112	46.7
2.8	0.039802	0.005500	0.039819	0.005465	101.4
1.8	0.010153	0.002018	0.010146	0.002010	99.9

In this problem, we again modeled a square region around the crack tip, the gray square in Figure 12b, and chose different values for crack's angle. The same tendency as for the 1st example is observed for this mixed mode problem. Again, $\gamma = 1.8$ gives the most accurate results and this method has a convergence rate of approximately 2.

As shown in Table 3.2 when γ decreases to the optimal value, in this case $\gamma = 1.8$, the error decreases, however the computational cost increases due to a larger radius of influence of the shape functions. Nevertheless, we note that the error is much smaller (almost an order of magnitude) between $\gamma = 4.8$, which is virtually the same as standard XFEM, and $\gamma = 1.8$. We note that there is only a very small difference between the $\alpha = 15^\circ$ and $\alpha = 30^\circ$. This can be explained by the fact that the discretization is identical, the only difference being the size of the forces applied to the boundaries, as can be seen from Figure 12. The log-log plots indicating the convergence rates of K_I and K_{II} with $\alpha = 30^\circ$ are shown in Figures 13 and 14. We also computed the errors for K_I and K_{II} for angles $\alpha = 45^\circ, 60^\circ, 75^\circ$ with similar results.

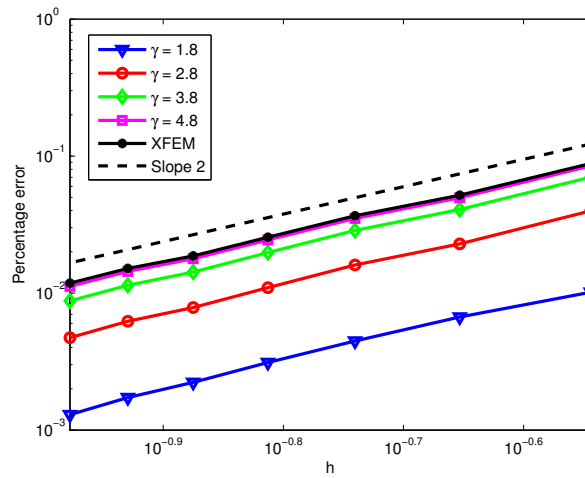


Figure 3.11: Percentage error of K_I for slanted crack in an infinite plate with $\alpha = 30^\circ$.

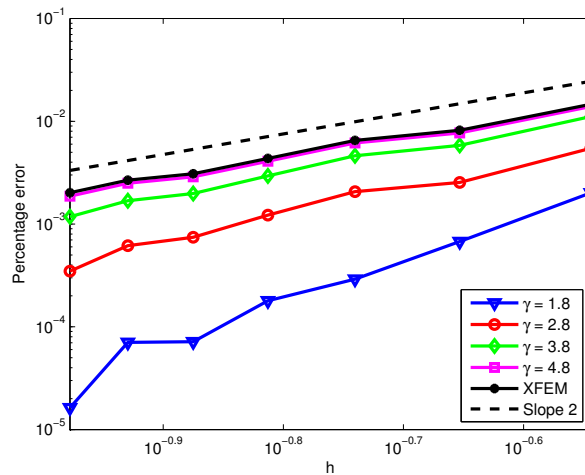


Figure 3.12: Percentage error of K_{II} for slanted crack in an infinite plate with $\alpha = 30^\circ$.

We conclude that the locality of the LME basis functions and their smoothness depends on a nondimensional parameter γ . The large values of γ leads to shape functions with steeper derivatives, while the small value results in smoother bubble-shaped basis functions with larger supports. We have incorporated the discontinuities and crack-tip singularity in the approximation space through XFEM-like enrichments, and we have tested the efficiency of the method through some 2D examples to determine suitable values γ .

Chapter 4

Phase-field model for Local Maximum entropy approximants

One of the most important questions in fracture mechanics is, “in what directions will a crack grow in structure?”. The XLME method and generally all the discrete methods to model crack, require cumbersome computation to get the direction of crack propagation, such as computing stress intensity factor for each elements.

In recent years, much attention has been devoted to variational problems involving both bulk and surface energies. Such problems are usually of the form

$$\min\{E_v(u, K) + E_s(u, K) + \text{"Lower order terms"}\}, \quad (4.1)$$

where E_v and E_s denote the volume and surface energies, and (u, K) are unknowns with K varying in a class of surfaces contained in a fixed open set $\Omega \subset R^n$ and $u : \Omega \setminus K \rightarrow R^m$ belonging to a class of sufficiently smooth functions. These kind of problems called free discontinuity problems (as opposed to free boundary problems). The free discontinuity problems have widely applications to the study of multi-phase systems, fracture mechanics, computer science, etc. In the case of fracture mechanics, $\Omega \subset R^3$ is the reference configuration of an elastic body, K is the crack surface and u represents the elastic deformation in the unfractured part of the body.

The extension of this method for fracture in solids was introduced in [48, 49], where the brittle crack propagation problem was regularized and recast as a minimization problem. In this model the proposed energy functional is similar to the potential functional presented by Mumford and Shah [50], which is used in image segmentation. The existence of solutions of the Mumford-Shah image segmentation functional was proven by Ambrosio in [51]. In [52], Ambrosio et al. approximated the Mumford and

Shah image segmentation functional by an elliptic functional defined on Sobolev space, based on the theory of Γ -convergence. Later on, Bourdin introduced image segmentation with a finite element method in [53]. We refer to Ambrosio and Tortorelli [52] and the reviews of Dal Maso [102] and Braides [103, 104] for details on Γ -convergent approximations of free discontinuity problems. Here we focus on energy base analysis of fracture. We study phase field model, which is based on global energy balance.

4.1 Governing Equations and Weak Form

4.1.1 Second and fourth-order phase field model

Consider a bar of length $2L$ placed in the domain $\Omega = \Gamma \times L$, where Γ is a cross-section and $L = [-\infty, \infty]$. According to Fig. 4.1(a), a crack is placed at $x = 0$. The phase field variable $v(x) \in [0, 1]$ with

$$v(x) = \begin{cases} 0 & x = 0, \\ 1 & \text{otherwise,} \end{cases} \quad (4.2)$$

is introduced to describe the crack topology. $v = 0$ indicates the crack (total damage) while $v = 1$ refers to intact state. This phase field is discontinuous at $x = 0$ and satisfies the following conditions

$$\begin{aligned} v(0) &= 0, \\ v(\pm\infty) &= 1. \end{aligned} \quad (4.3)$$

A function that fulfils the criterion (4.2) and (4.3) is

$$v(x) = 1 - e^{-\frac{|x|}{2l_0}}, \quad (4.4)$$

when the diffusivity $l_0 \rightarrow 0$. Furthermore, as it was shown in [105], this function is the solution of a homogeneous second order differential equation

$$v(x) - 4l_0^2 v'' - 1 = 0 \quad \text{in } \Omega, \quad (4.5)$$

subject to the essential boundary conditions given in Eq. (4.3). This second order differential equation leads to a second order phase field approximation method, which

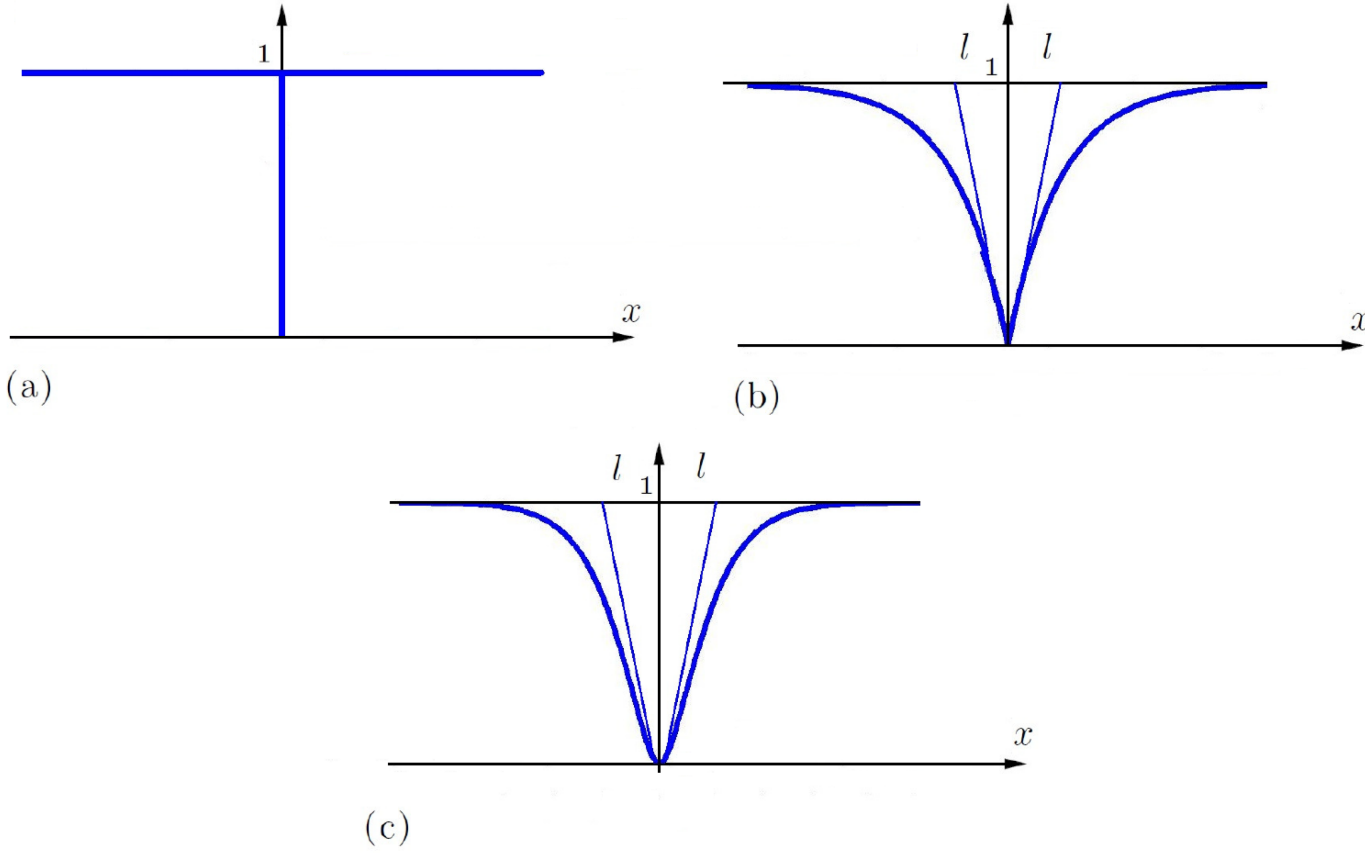


Figure 4.1: (a) Sharp crack at $x = 0$, (b) Exponential solution of the second order phase field model and (c) Exponential solution of the fourth order phase field model with the length scale parameter $l = 2l_0$.

computes the length of the crack by

$$\Gamma_{l_0} = \frac{1}{4l_0} \int_{\Omega} (1 - v)^2 + 4l_0^2 (v')^2 dV. \quad (4.6)$$

With $dV = \Gamma dx$. In order to approximate this function, a C^0 basis such as the one provided by the standard finite element method (FEM) is needed. In meshfree methods such as LME approximants [77], the basis functions are smooth. Hence, the kink (at $x = 0$) in the phase field might not be captured sufficiently with these methods. Let us assume another function [106]

$$v(x) = 1 - e^{-\frac{|x|}{l_0}} \left(1 + \frac{|x|}{l_0} \right). \quad (4.7)$$

This function satisfies the conditions (4.3) and introduces smoother approximation as is demonstrated in Fig. 4.1(c). We find that Eq. (4.7) is the solution of the homogeneous

fourth order differential equation

$$v - 1 - 2l_0^2 v'' + l_0^4 v^{(4)} = 0 \quad \text{in } \Omega, \quad (4.8)$$

under the assumption that $v(0) = 0, v'(0) = 0$ and $v^\alpha(x) \rightarrow 0$ as $x \rightarrow \pm\infty$ for all $\alpha \geq 0$ [106]. The weak form functional of this ordinary differential equations (ODE) is

$$I(v) = \frac{1}{2} \int_{\Omega} (1 - v)^2 + 2l_0^2 (v')^2 + l_0^4 (v'')^2 dV. \quad (4.9)$$

The value of this functional for Eq. (4.7) is $2l_0\Gamma$, which gives

$$\Gamma_{l_0} = \frac{1}{4l_0} \int_{\Omega} (1 - v)^2 + 2l_0^2 (v')^2 + l_0^4 (v'')^2 dV. \quad (4.10)$$

As was expressed by Miehe and coworkers in [105], the functional Γ_{l_0} can be considered as the crack surface itself. Eq. (4.10) is the fourth order phase field model in 1D.

Finite elements based on Lagrange polynomials are not well suited for the fourth-order phase-field model which requires C^1 continuity in the phase field. A common approach is to split the fourth-order differential equation into 2 second-order differential equations as proposed e.g. in [107]. Due to the higher order continuity of the LME approximations, they are ideally suited to directly solve the fourth-order phase field equations. Such an approach has been proven to be successful in IGA [107]. However, in contrast to IGA which requires a quadratic basis, the LME approximation uses only a linear basis.

The extension of the phase field model to higher dimensional problems is straightforward. Assume $\Omega \subseteq R^d$, be a domain with $d \in [1, 2, 3]$ and $\partial\Omega \subseteq R^{d-1}$ is the boundary of this domain. The crack length can be computed by

$$\Gamma_{l_0}(v) = \int_{\Omega} \gamma(v, \nabla v, \Delta v) dV, \quad (4.11)$$

with

$$\gamma(v, \nabla v) = \frac{1}{4l_0} \left[(1 - v)^2 + l_0^2 |\nabla v|^2 \right], \quad (4.12)$$

for the second order model and

$$\gamma(v, \nabla v, \Delta v) = \frac{1}{4l_0} \left[(1 - v)^2 + 2l_0^2 |\nabla v|^2 + l_0^4 |\Delta v|^2 \right], \quad (4.13)$$

for the fourth order model.

4.1.2 Phase field model for an elastic body

In [5], Griffith demonstrated that crack propagation for elastic solids, is caused by the transfer of energy from the external work to surface energy. He applied the first law of thermodynamics to formulate cracks in elastic solid bodies. The first law of thermodynamics states the change of total energy is equal to the sum of the change of work done by the external forces and the change of heat content per unit time. Since, the loads are applied in a quasi static behavior in this work, the change of heat and the kinetic energy are zero. The change of the total energy for this case, can be written as

$$\frac{\partial}{\partial a}(E + \Gamma) = \frac{\partial P}{\partial a} \quad (4.14)$$

Here E is the total internal strain energy, Γ the surface energy, a indicates the crack length and P the external work. Therefore, following Griffith model for brittle material we define

$$G = \frac{\partial \Gamma}{\partial a} = \frac{\partial P}{\partial a} - \frac{\partial E}{\partial a}, \quad (4.15)$$

where G is the energy release rate or the crack driving force. The material parameter G_c is the critical energy release rate or the surface energy density. The crack propagates when G gets G_c , where the crack surface is approximated by

$$\Gamma \approx G_c \Gamma_{l_0},$$

Γ_{l_0} is crack surface functional defined in Eq.4.11.

For a linear elastic isotropic solid, the strain energy is expressed as

$$E = \int_{\Omega} F(\boldsymbol{\varepsilon}(\mathbf{u}), v) dV, \quad (4.16)$$

We assume traction free conditions on the crack faces. In order to satisfy this condition, the elastic energy density of an undamaged solid, F_0 , is multiplied by the jump set function $g(v)$ yielding

$$F(\boldsymbol{\varepsilon}(\mathbf{u}), v) = g(v)F_0(\boldsymbol{\varepsilon}(\mathbf{u})), \quad (4.17)$$

where $F_0(\boldsymbol{\varepsilon}(\mathbf{u})) = \frac{1}{2}\boldsymbol{\varepsilon}(\mathbf{u}) : \mathbf{C} : \boldsymbol{\varepsilon}(\mathbf{u})$. Here \mathbf{C} is the elasticity tensor and $\boldsymbol{\varepsilon}(\mathbf{u}) = \mathbf{D}\mathbf{u}$ with

$$\mathbf{D} = \begin{pmatrix} \frac{\partial}{\partial x_1} & 0 & 0 \\ 0 & \frac{\partial}{\partial x_2} & 0 \\ 0 & 0 & \frac{\partial}{\partial x_3} \\ \frac{\partial}{\partial x_2} & \frac{\partial}{\partial x_1} & 0 \\ 0 & \frac{\partial}{\partial x_3} & \frac{\partial}{\partial x_2} \\ \frac{\partial}{\partial x_3} & 0 & \frac{\partial}{\partial x_1} \end{pmatrix}$$

The function $g(v)$ is assumed to satisfy the following conditions,

$$g(0) = 0, g(1) = 1, g'(0) = 0, \quad (4.18)$$

$$\forall v_1, v_2 \in [0, 1], \text{ if } v_1 \leq v_2 \Rightarrow g(v_1) \leq g(v_2). \quad (4.19)$$

The first and second condition in Eq.4.18, are the limits for the fully damage and undamaged case. The third condition states that when $v \rightarrow 0$, the energy converges to a finite value. A simple function that meets these requirements, is

$$g(v) = v^2 + k \quad (4.20)$$

The parameter $k \ll 1$ is introduced to avoid the singularity of disappearing internal energy density when the phase-field parameter is zero. Consider the external potential energy functional

$$P(\mathbf{u}) = \int_{\Omega} \mathbf{b}(x) \cdot \mathbf{u} dV + \int_{\Gamma_t} \mathbf{t}_N(x) \cdot \mathbf{u} d\Gamma_t, \quad (4.21)$$

where $\mathbf{b}(x)$ is body force and $\mathbf{t}_N(x)$ are the tractions. The total potential energy functional is introduced as

$$\Pi(\mathbf{u}, v) = E(\mathbf{u}, v) + G_c \Gamma_{l_0} - P(\mathbf{u}). \quad (4.22)$$

Since the variations $\delta \mathbf{u}$ and δv are independent, the first variation of the functional, $\Pi(\mathbf{u}, v)$, leads to two decoupled equations

$$\Pi[\mathbf{u}, v, \delta \mathbf{u}] = \delta_{\mathbf{u}} E(\mathbf{u}, v) - \delta_{\mathbf{u}} P(\mathbf{u}) = 0, \quad (4.23)$$

$$\Pi[\mathbf{u}, v, \delta \mathbf{u}] = \int_{\Omega} [v^2 + k] \delta_{\mathbf{u}} F_0(\boldsymbol{\varepsilon}(\mathbf{u})) dV - \left[\int_{\Omega} \mathbf{b}(x) \cdot \delta \mathbf{u} dV + \int_{\Gamma_t} \mathbf{t}_N(x) \cdot \delta \mathbf{u} d\Gamma_t \right] = 0. \quad (4.24)$$

$$\Pi[\mathbf{u}, v, \delta v] = \delta_v E(\mathbf{u}, v) + G_c \delta_v \Gamma_{l_0} = 0 \quad (4.25)$$

For the second order phase field model, we obtain

$$\Pi_{2nd}[\mathbf{u}, v, \delta v] = \int_{\Omega} \left\{ 2v \delta v F_0(\boldsymbol{\varepsilon}(\mathbf{u})) + \frac{G_c}{2l_0} [-\delta v + v \delta v + 4l_0^2 \nabla v \cdot \nabla(\delta v)] \right\} dV, \quad (4.26)$$

and for the fourth order phase field model

$$\Pi_{4th}[\mathbf{u}, v, \delta v] = \int_{\Omega} \left\{ 2v \delta v F_0(\boldsymbol{\varepsilon}(\mathbf{u})) - \frac{G_c}{2l_0} \delta v + \frac{G_c}{2l_0} [v \delta v + 2l_0^2 \nabla v \cdot \nabla(\delta v) + l_0^4 \Delta v \cdot \Delta(\delta v)] \right\} dV. \quad (4.27)$$

The decoupled equations can be solved by a staggered scheme which is more robust which has been demonstrated e.g. by [108].

4.2 Discretization with LME approximates

We consider now the discrete equilibrium equations of (4.23) and (4.25), and approximate \mathbf{u} and v as follow

$$\mathbf{u} = \sum_a p_a u_a, \quad (4.28)$$

$$v = \sum_a p_a v_a, \quad (4.29)$$

where p_a are LME shape functions and u_a and v_a are nodal displacement and phase field parameter. Virtual displacements and virtual phase-field parameters are represented likewise. Replacing the variation of the strain energy density into the Eq. (4.24), we obtain

$$\Pi[\mathbf{u}, v, \delta \mathbf{u}] = \int_{\Omega} [v^2 + k] \{ \mathbf{D}(\delta \mathbf{u}) : \mathbf{C} : \mathbf{D} \mathbf{u} \} dV - \left[\int_{\Omega} \mathbf{b}(x) \cdot \delta \mathbf{u} dV + \int_{\Gamma_t} \mathbf{t}_N(x) \cdot \delta \mathbf{u} d\Gamma_t \right] = 0. \quad (4.30)$$

Approximating \mathbf{u} and $\delta \mathbf{u}$ with (4.28) and a simple calculation yields the Galerkin stiffness matrix. The interaction between nodes a and b for displacement field is given by

$$\mathbf{K}_u^{ab} = \int_{\Omega} [v^2 + k] \mathbf{B}^a \mathbf{C} \mathbf{B}^{bT} dV, \quad (4.31)$$

where

$$\mathbf{B}^a = \mathbf{D} p_a.$$

The force contribution of the a -th node is

$$\mathbf{f}_u^a = \int_{\Omega} \mathbf{b} p_a dV + \int_{\Gamma_t} \mathbf{t}_N p_a d\Gamma_t. \quad (4.32)$$

Finally, the phase-field stiffness matrix for the second and fourth order are

$$\mathbf{K}_v^{ab} = \int_{\Omega} \left\{ [2F_0(\boldsymbol{\varepsilon}(\mathbf{u})) + \frac{G_c}{2l_0}] p_a p_b + 2G_c l_0 \nabla p_a \nabla p_b \right\} dV \quad (4.33)$$

$$\mathbf{K}_v^{ab} = \int_{\Omega} \left\{ [2F_0(\boldsymbol{\varepsilon}(\mathbf{u})) + \frac{G_c}{2l_0}] p_a p_b + \frac{G_c}{l_0} [l_0^2 \nabla p_a \nabla p_b + \frac{l_0^4}{2} \Delta p_a \Delta p_b] \right\} dV \quad (4.34)$$

and the right hand side for phase-field is

$$\mathbf{f}_v^a = \int_{\Omega} \frac{G_c}{2l_0} p_a dV. \quad (4.35)$$

In this model, cracks can propagate, branch and merge but can not reverse, whereas this feature is reached by imposing $v^i \leq v^{i-1}$, such that v^{i-1} and v^i are the phase-field parameters at step $i-1$ and i [109].

4.3 Numerical Examples

4.3.1 Phase Field Problems

One-dimensional problem

First, we determine how well the proposed second and fourth order models approximate the “crack topology”. For simplicity, we start with the 1D model explained in section 4.1. We compute the error in the L^2 norm and H^1 semi-norm for the second order model by considering Eq. (4.4) as exact solutions and $L = 1$. As it is obvious from Fig. 4.2, the best results are obtained for $\gamma = 5.8$. The rate of convergence in the L^2 norm in this case is about 1.7, while the rate of convergence for $\gamma < 2.8$ is about 1.0. The convergence rate in the H^1 semi-norm is optimal, i.e. equal 1, with $\gamma = 5.8$ but sub-optimal (order 0.4) for $\gamma \leq 2.8$. This is due to the smooth shape functions to approximate non-smooth function. For $\gamma = 5.8$, the LME shape functions are much sharper.

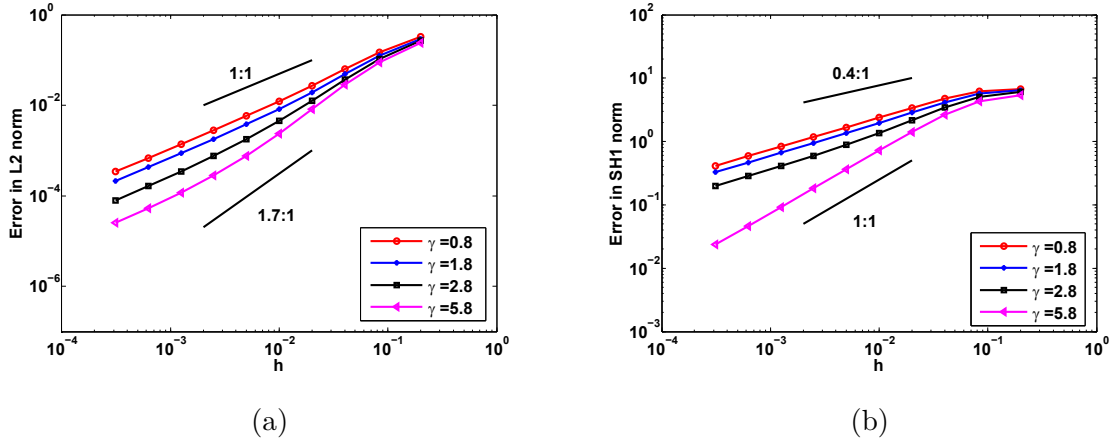


Figure 4.2: The error in the L^2 norm and Semi-norm H^1 of the solution of the second order ODE as a function of nodal spacing, h , with $l_0 = 0.025$ and different values of γ .

For the fourth order phase field model, we compute the error in the L^2 norm, H^1 semi-norm and H^2 semi-norm. For the LME shape functions, the best results are obtained for $\gamma = 0.6$. As can be seen from Fig. 4.3a, for values of $\gamma \geq 1.0$ no convergence in the L^2 norm is obtained. Note that, in contrast to the at least quadratic NURBS–formulation [110], we employ only linear basis. In FEM, Hughes [111] have shown for the fourth order PDEs, at least a quadratic basis is required. However, as shown in our previous work [112], a linear LME basis was sufficient to obtain excellent results for Kirchhoff–Love thin shells (also fourth order PDE).

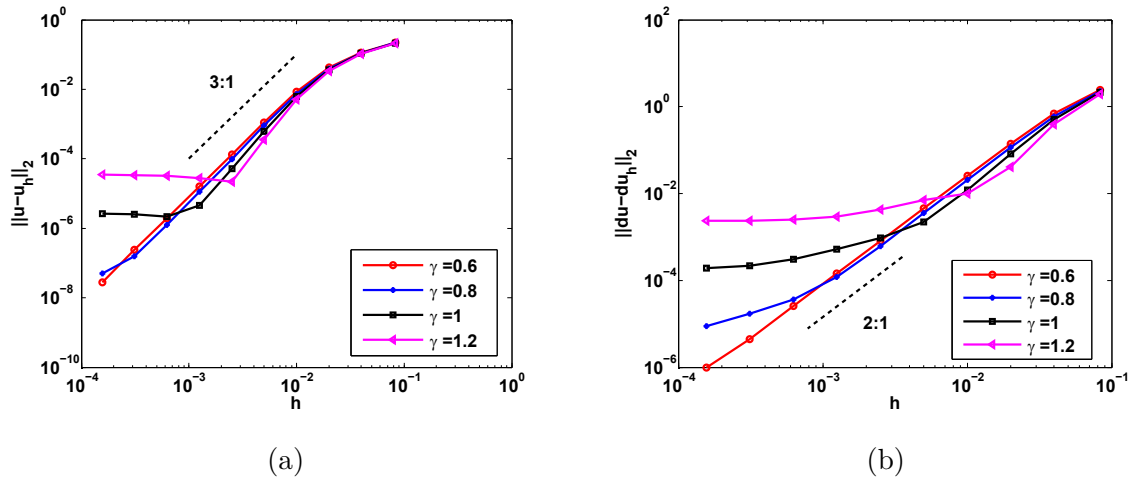


Figure 4.3: The error in the L^2 norm and Semi-norm H^1 of the solution of the fourth order ODE as a function of nodal spacing, with $l_0 = 0.025$ and different values of γ .

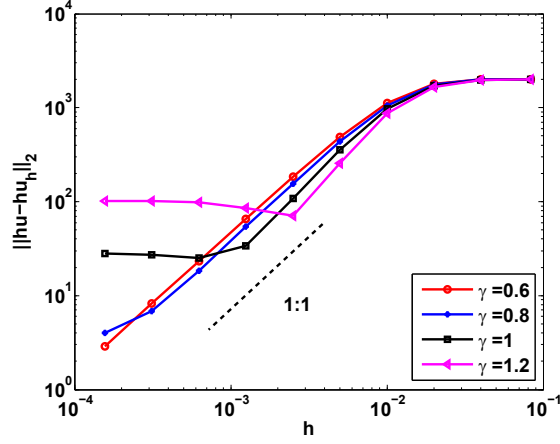


Figure 4.4: The error in semi-norm H^2 of the solution of the fourth order ODE as a function of nodal spacing, with $l_0 = 0.025$ and different values of γ .

Two dimensional domain

Subsequently, we will study the accuracy of the second and fourth order phase field model to approximate the crack length according to Fig. 4.5. There are two sources of errors in the phase field model:

1. Error of the approximation of the crack geometry, which is related to length scale parameter.
2. Model error which is related to the phase field model.

We first focus on the first error. The length scale parameter l_0 is considered as a positive parameter to regulate the size of the fracture zone. When l_0 goes to zero, Γ_{l_0} converges to the discrete fracture surface. A certain minimum mesh size is needed to find the “appropriate” length scale. Here we consider a two dimensional domain Ω with a sharp crack surface $\Gamma = 0.5$ as is shown in the Fig. 4.5.

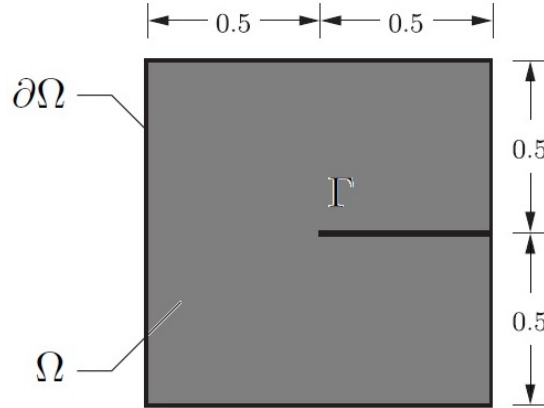


Figure 4.5: Two dimensional 1×1 square, with a sharp crack surface $\Gamma = 0.5$.

We approximate the crack surface of Fig. 4.5 by the second and fourth order model for different length scales and different values of γ with constant nodal spacing size $h = 0.0013$. As it is obvious from Fig. 4.6, more accurate results are obtained with smaller length scale parameter for the fourth order approximation. For the second order phase field model, higher values of γ give better results. For instance, $\gamma = 4.8$ and $2h \leq l_0$ resolves the regularized crack surface such that $\Gamma_{l_0} \approx \Gamma$, while for $\gamma = 1.8$, $4h \leq l_0$ is needed. Hence, in the second order model, as γ increases the results get better and a finer length scale parameter is needed. In the fourth order phase field approximation model, as γ decreases the results get better. In this case, for all values of γ , choosing $h \leq l_0$ gives reasonable results. Fig. 4.8 indicates the error in the L^2 norm of the fourth and second order phase field models for best values of γ . The fourth order model represents the crack geometry more accurately.

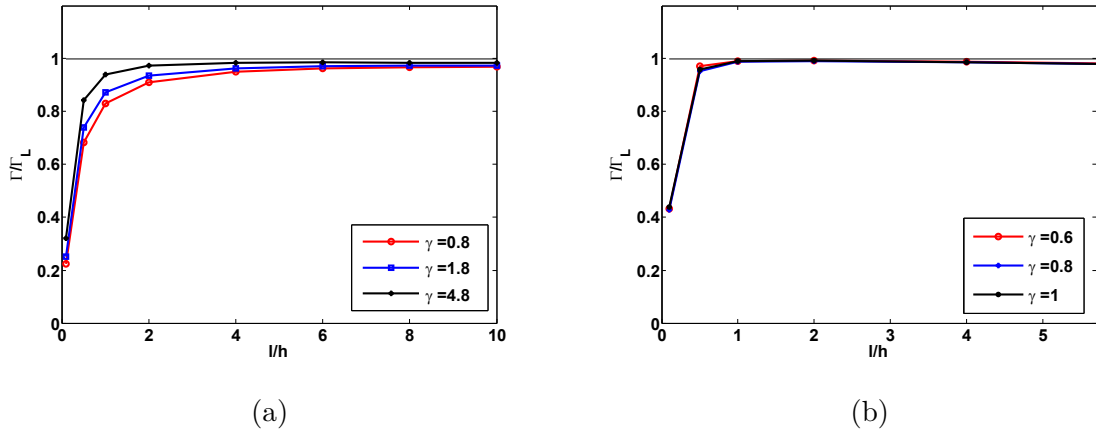


Figure 4.6: Exact crack length over approximated crack length versus length scale parameter over nodal spacing, by (a) the second order phase field model with $\gamma = 0.8, 1.8, 4.8$, and (b) the fourth order phase field model with $\gamma = 0.6, 0.8, 1.0$, for $h = 0.0013$.

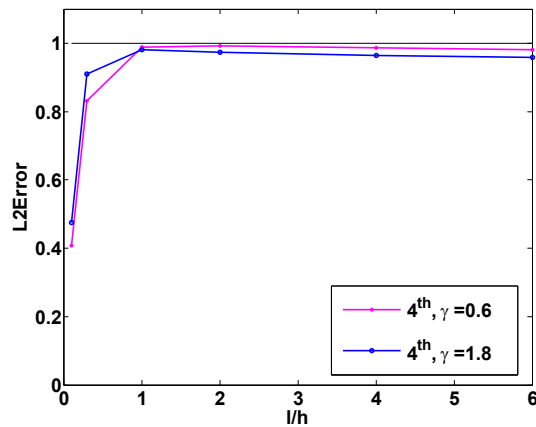


Figure 4.7: Exact crack length over approximated crack length versus length scale parameter over nodal spacing the fourth order phase field model with $\gamma = 0.6, 1.8$, for $h = 0.0013$.

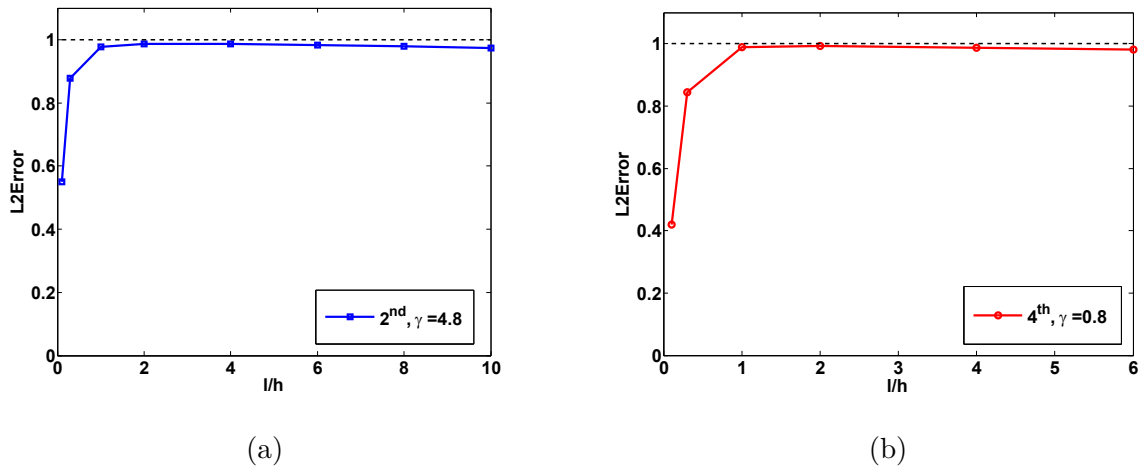


Figure 4.8: L^2 norm error versus length scale parameter over nodal spacing, by (a) the second order phase field model with $\gamma = 4.8$, and (b) the fourth order phase field model with $\gamma = 0.8$.

Next, we study the model error. The rate of convergence of these two models are compared for the same length scale parameter l_0 . The best rate of convergence is obtained for the fourth order model with lower γ and lower l_0 . Fig. 4.9 shows the rate of convergence of these two models with $l_0 = 2h$. The second order model with $\gamma = 0.8$ converges much slower than the fourth order model. This is due to the large radius of influence and smoothness of the LME shape functions. Fig. 4.9 also shows the rate of convergence for the second order model with $\gamma = 4.8$ and $l_0 = 2h$. In this case, the rate of convergence of the second order model is still much lower than the fourth order model with $\gamma = 0.8$ and $l_0 = 2h$.

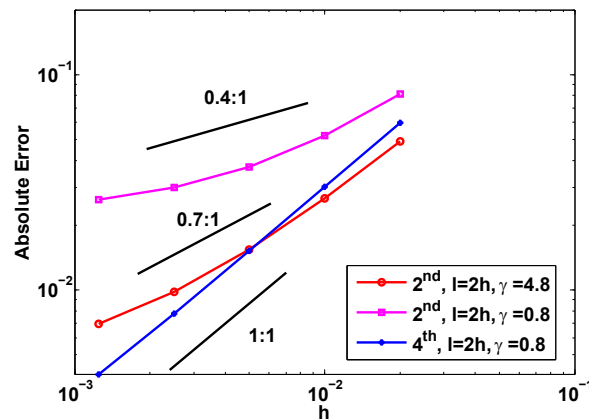


Figure 4.9: Absolute error of the crack length for the second and fourth order models.

4.3.2 Mechanical Problems

Infinite plate with a horizontal crack

In order to study the accuracy of the phase field model, we discuss a benchmark problem that has an exact solution. Consider an infinite plate with a horizontal crack of length $2a$ under a remote uniform stress field σ as shown in Fig. 3.3. The analytical solution near crack tip for stress fields and displacement in terms of local polar coordinates from the crack tip are as given in (3.7). The analytical solution is valid for region close enough to the crack tip. So, we consider a square ABCD of length $1mm \times 1mm$, $a = 100mm$, $E = 10^7 N/mm^2$, $\nu = 0.3$, $\sigma = 10^4 N/mm^2$ and the modeled crack length is $0.5mm$. Plane strain state is assumed. Dirichlet boundary conditions are imposed on the edges and the crack does not propagate. As we mentioned, LME shape functions satisfy a weak Kronecker delta property. This property allows us to impose Dirichlet boundary conditions by computing a node-based interpolant or an L^2 projection of the boundary data. We first solve a linear system for the v -field, subsequently we solve the elastic linear system for \mathbf{u} . For stationary cracks, the phase field value is not updated. Fig. 4.10a indicates the error in the $L2$ displacement norm for different length scale parameter for the finite element method, the second and fourth order methods with $\gamma = 4.8$ and $\gamma = 1.0$, respectively. Choosing $2h \leq l_0 < 4h$ and $l_0 \geq 8h$ for the fourth and second order model, respectively, gives the best approximation of the solution (for $h = 0.005$). As mentioned before, this figure also illustrates almost the same results for FEM and the second order method with $\gamma = 4.8$. In this case, the value of the length scale parameter, for the second order model and FEM, is large. In other words, a fine discretization is needed to resolve the crack, if small length scale parameter is required. Fig. 4.10b shows the $L2$ norm error versus h for different discretization. The best rate of convergence, is obtained for the fourth order phase field model with $\gamma = 1.0$ and $l_0 \geq 2h$. The convergence rate of 0.63 is poor. However, the phase field model cannot capture the jump in the displacement field and the analytic crack opening as discrete crack approaches such as XFEM. In this view, the convergence rate of the fourth order model is surprisingly good.

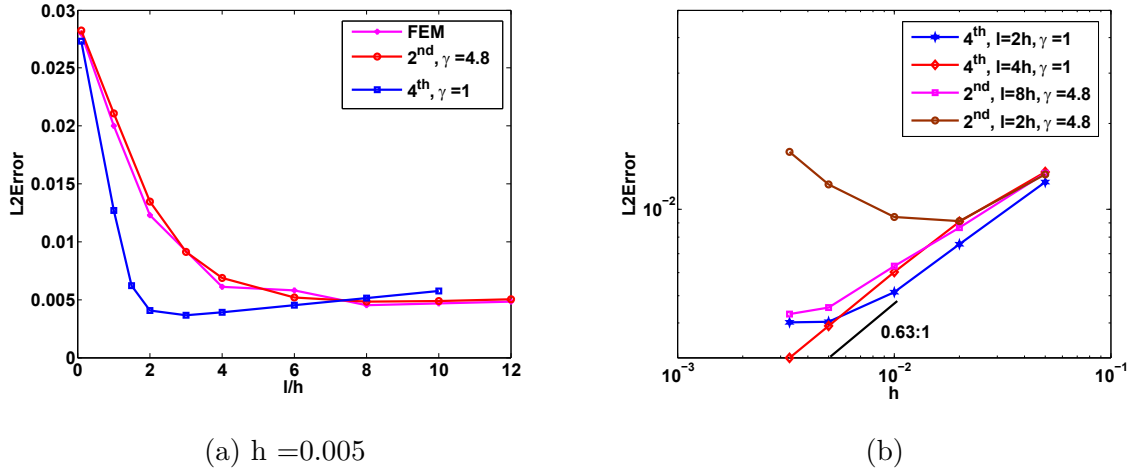


Figure 4.10: (a) L^2 norm Error for $h = 0.005$, and different values of l_0 , (b) L^2 norm Error versus different discretization.

Cantilever beam

Consider the two-dimensional cantilever beam problem under plane strain condition [105, 106]. The geometric setup is indicated in Fig. 4.11. In order to avoid rigid body motion, we fix the point $x = 1, y = 0.5$ and the left ends are displaced as shown in Fig. 4.11. The material properties used for the analysis are $E = 10^9$ N/mm², Poisson's ratio $\nu = 0.3$, critical energy release rate $G_c = 1000$ N/mm and $k = 10^{-6}$. Constant displacement increments $\Delta u = 0.6 \times 10^{-6}$ mm, are used for each step of computation. For computational efficiency, the discretization is refined only in the area where the crack is expected to propagate. We also study the effects of the length scale parameter. Fig. 4.12 shows that mesh-independent results are achieved when refining the discretization. For $h = 0.0015$, the influence of the length scale parameter on the global response of these two models, is analyzed in Fig. 4.13. For the fourth order model, $l_0 \geq 4h$, is needed in order to obtain a nearly identical peak load and post-peak curve. While for the second order model $l_0 \geq 12h$ is needed. In other words, the second order model is more sensitive with respect to the length scale. The crack path at different stages is illustrated in Fig. 4.14. As it was expected, the crack propagates straight [105].

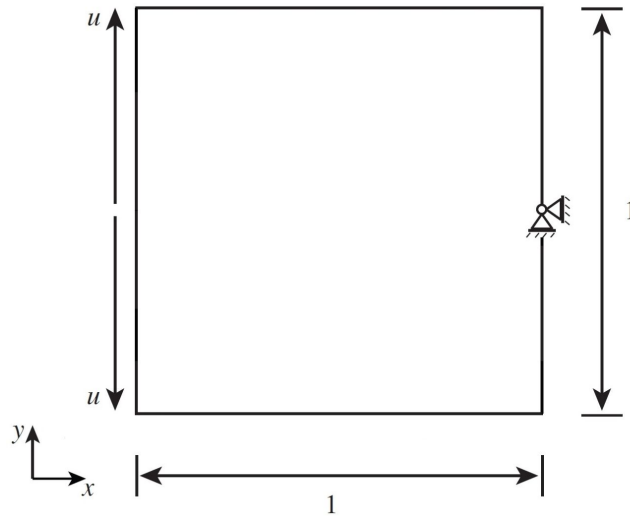


Figure 4.11: The geometry and boundary conditions of a square beam of side length $L = 1$ mm.

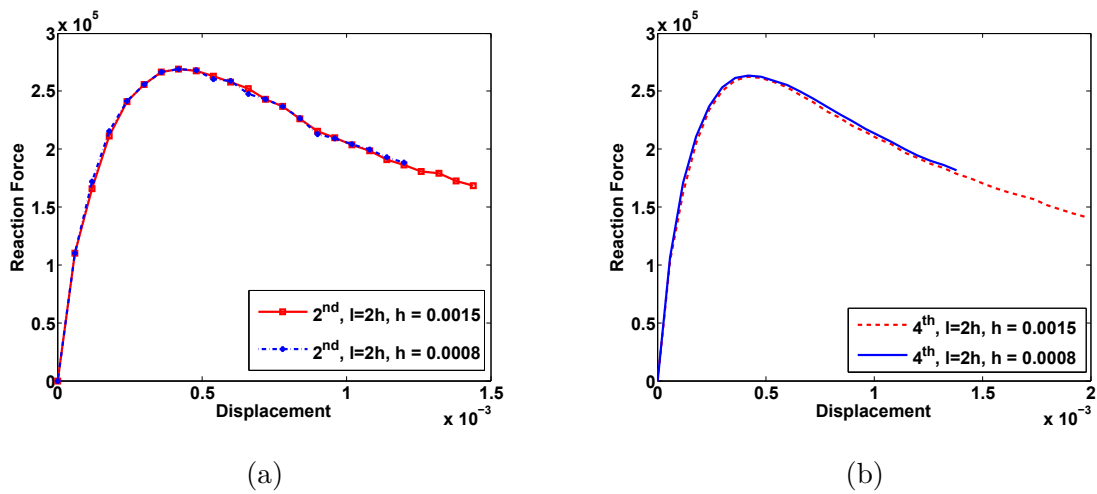


Figure 4.12: Load-deflection curves of (a) the second order model with $\gamma = 4.8$, (b) the fourth order model with $\gamma = 1.0$, $l_0 = 2h$, $h = 0.0015, 0.0008$ and 15274, 60931 nodes respectively.

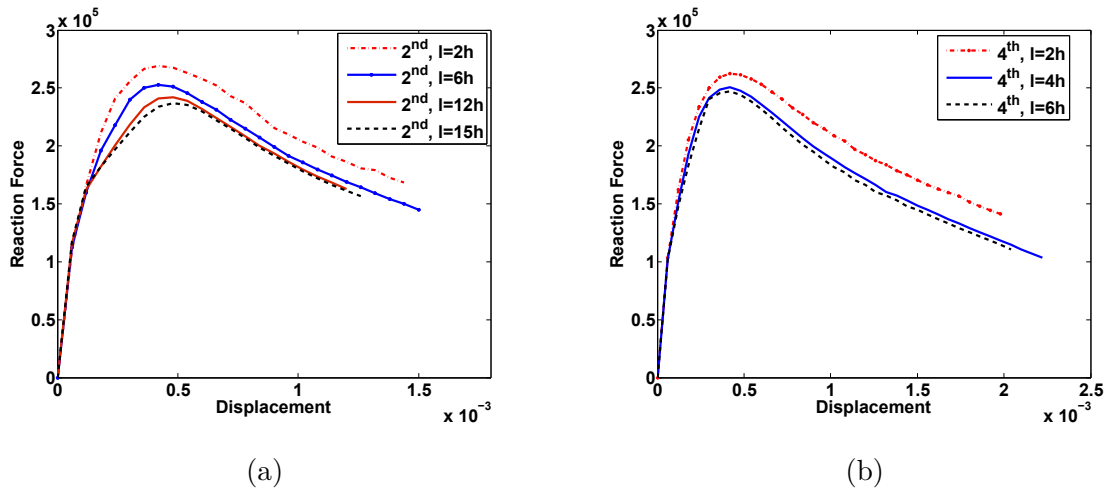


Figure 4.13: (a) Load-deflection curves of the second order method for different values of l_0 , fixed value $h = 0.0015$ and $\gamma = 4.8$. (b) Load-deflection curves of the fourth order model for different values of l_0 , fixed value $h = 0.0015$ and $\gamma = 1.0$.

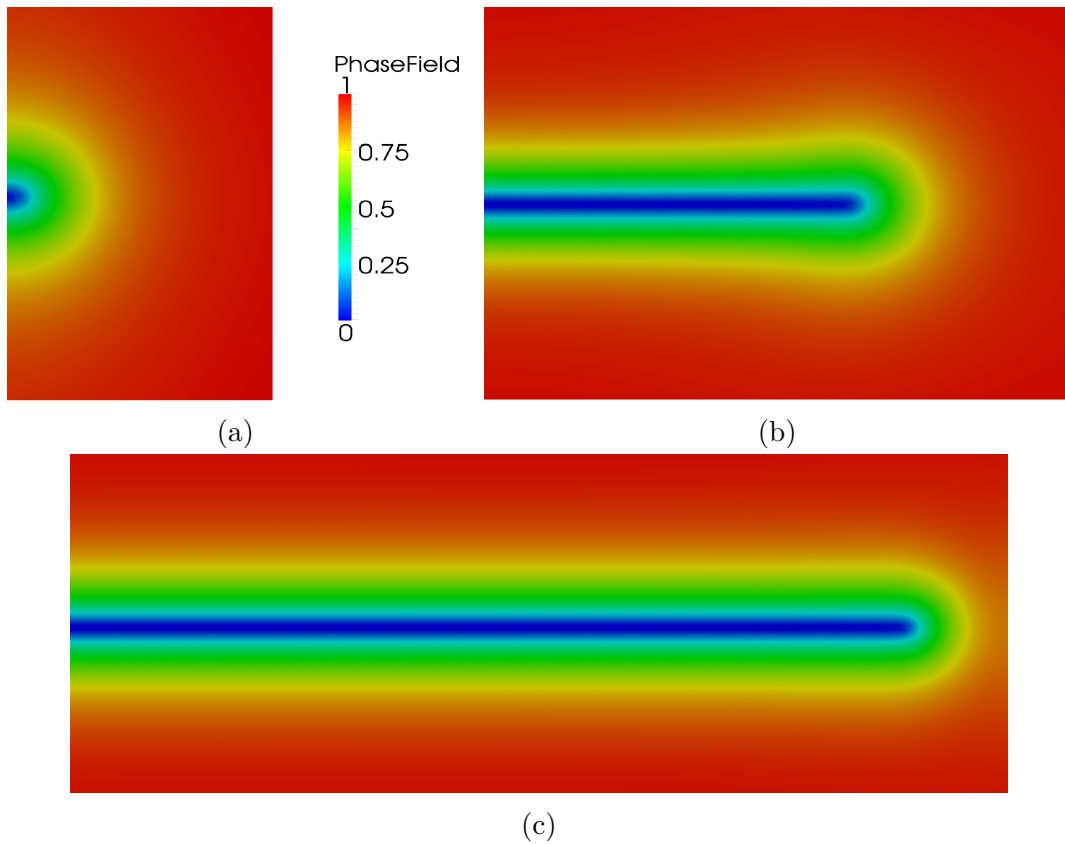


Figure 4.14: Close up around the crack path at the three stages of evolution.

Three-dimensional tension test

A similar problem is now solved in three dimensions as is illustrated in Fig. 4.15. The geometry and the boundary conditions are given in Fig. 4.15 as well. In order to avoid rigid body motion, the line $x = 0, y = 2.5$ and the point $x = 0, y = 2.5, z = 0.5$ are fixed. Numerical integration is applied on an unstructured background mesh of linear tetrahedral elements. The results are depicted in Fig 4.16 for an effective nodal spacing $h = 0.06\text{mm}$. The discretization is refined in an area where the crack is expected to propagate in order to approximate the sharp limit case $l_0 \rightarrow 0$. Material parameters have been selected as $E = 10^9$ and $\nu = 0.3, G_c = 100$. The constant displacement increments $\Delta u = 1.5 \times 10^{-5}\text{mm}$, are applied for each step of computation. The crack propagation path is illustrated in Figs. 4.16 and 4.17 . As it was expected, the crack propagates in the symmetry path [105]. Figs. 4.18 and 4.19 show the load-deflection curves for different discretization. Fig. 4.20 illustrate the load-deflection curves for different values of G_c .

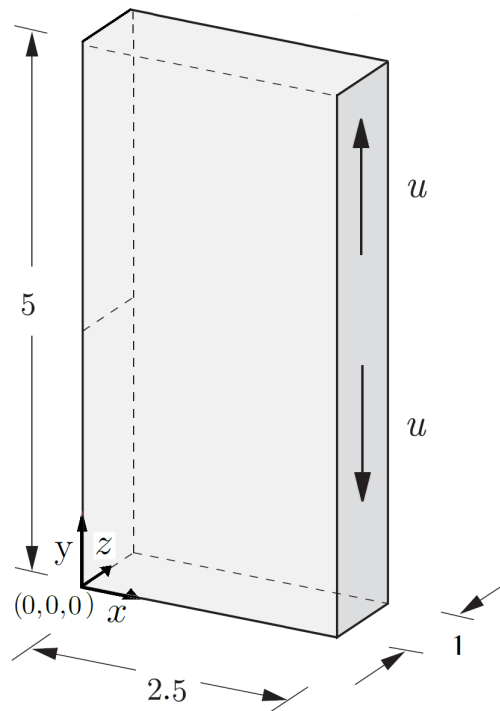


Figure 4.15: Geometry, loading and boundary condition for the three-dimensional mode-I tension test.

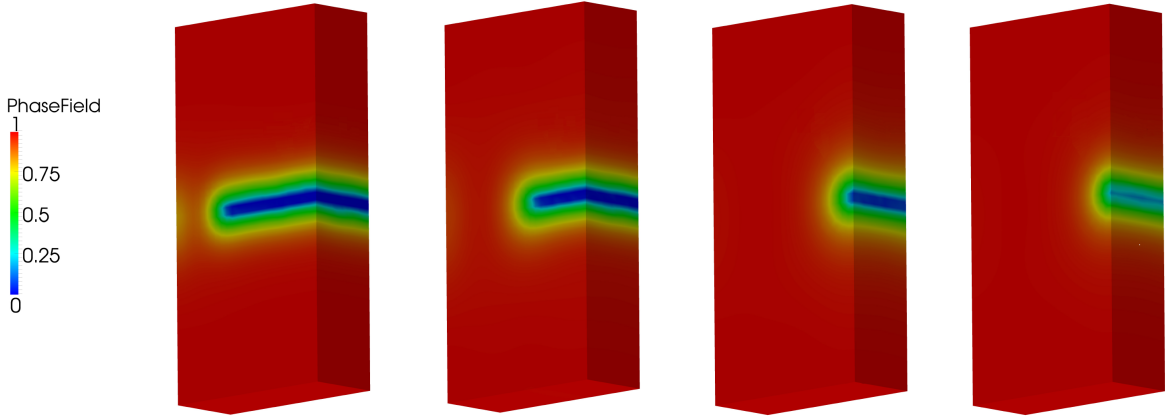


Figure 4.16: The crack path at the four stages of evolution.

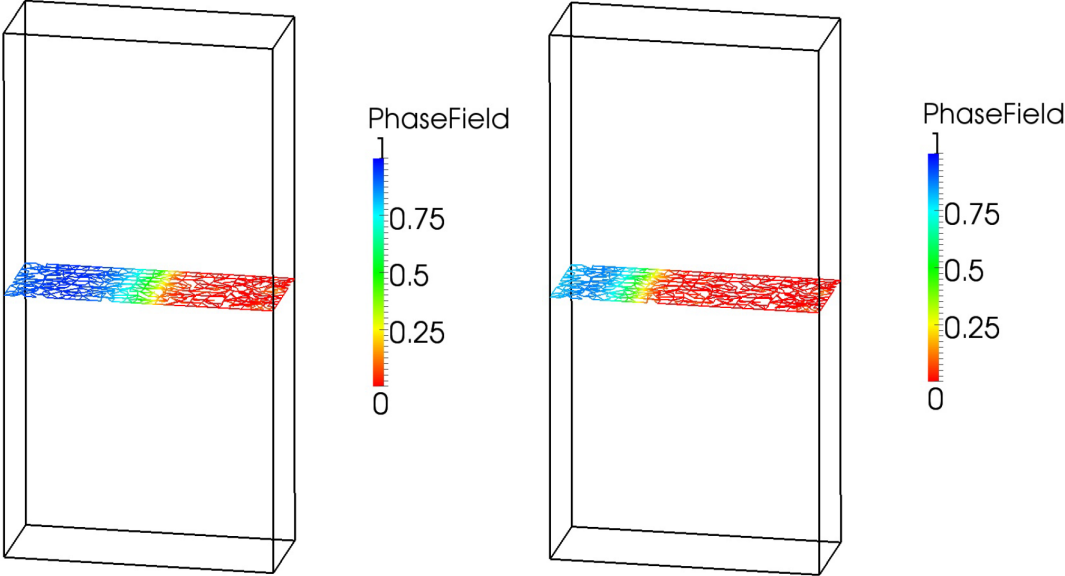


Figure 4.17: Phase field results on the cross section plane $y = 2.5$ to indicate crack path inside the body.

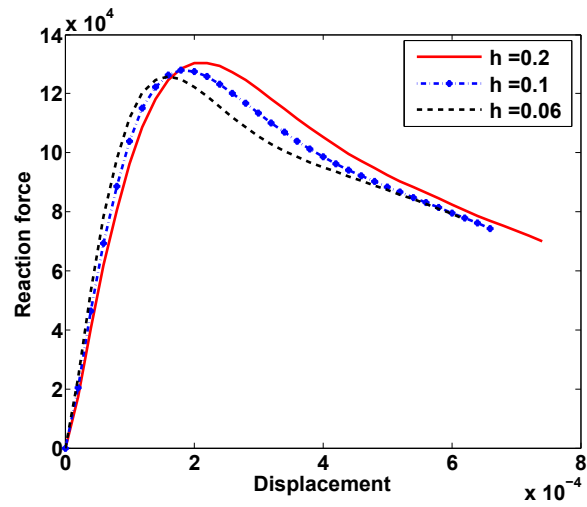


Figure 4.18: Load-deflection curves of the second order method with $\gamma = 4.8$, $l_0 = 0.414$ and different refinement with 1661, 14453, 28177 number of nodes respectively.

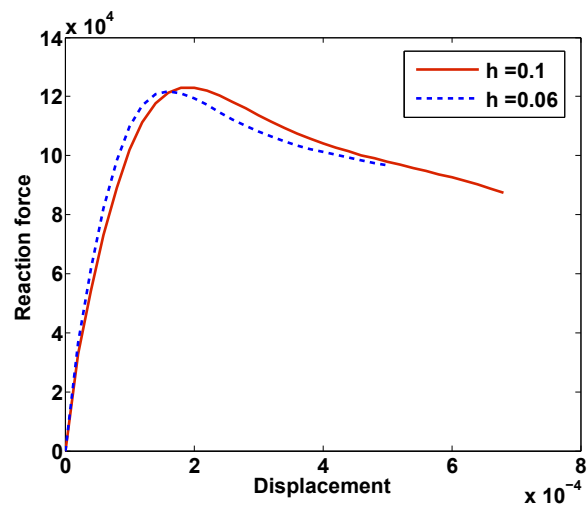


Figure 4.19: Load-deflection curves of the fourth order method with $\gamma = 1.8$, $l_0 = 0.414$ and different refinement with 14453, 28177 number of nodes respectively.

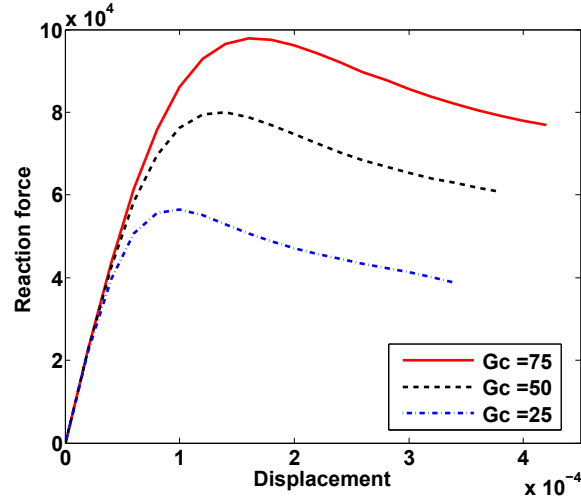


Figure 4.20: Reaction force-displacement curves for the fourth order model with $h = 0.1$, $l_0 = 0.414$, $\gamma = 1.8$ and different values of G_c .

Single edge notched beam with initial crack

In this example we study a slanted crack propagation problem. The initial crack, all relevant mechanical properties, boundary conditions and the dimensions are shown in Fig. 4.21. We consider the regularization parameter, approximately two times the effective nodal spacing. The results are shown in Figs. 4.22, 4.23 and 4.24, for 148790 number of nodes and an effective nodal spacing $h = 1\text{mm}$. The discretization is refined around the expected crack path. The constant displacement increments $\Delta u = 10^{-3}\text{mm}$, are applied for each step of computation. The crack propagation path is illustrated in Figs. 4.22, 4.23. In Fig. 4.23, the crack path for the second and fourth order model is compared with the experimental result in [1]. The load displacement curves are shown in Fig. 4.24 for both phase field models, XFEM [2] containing 46380 elements and experimental results in [1].

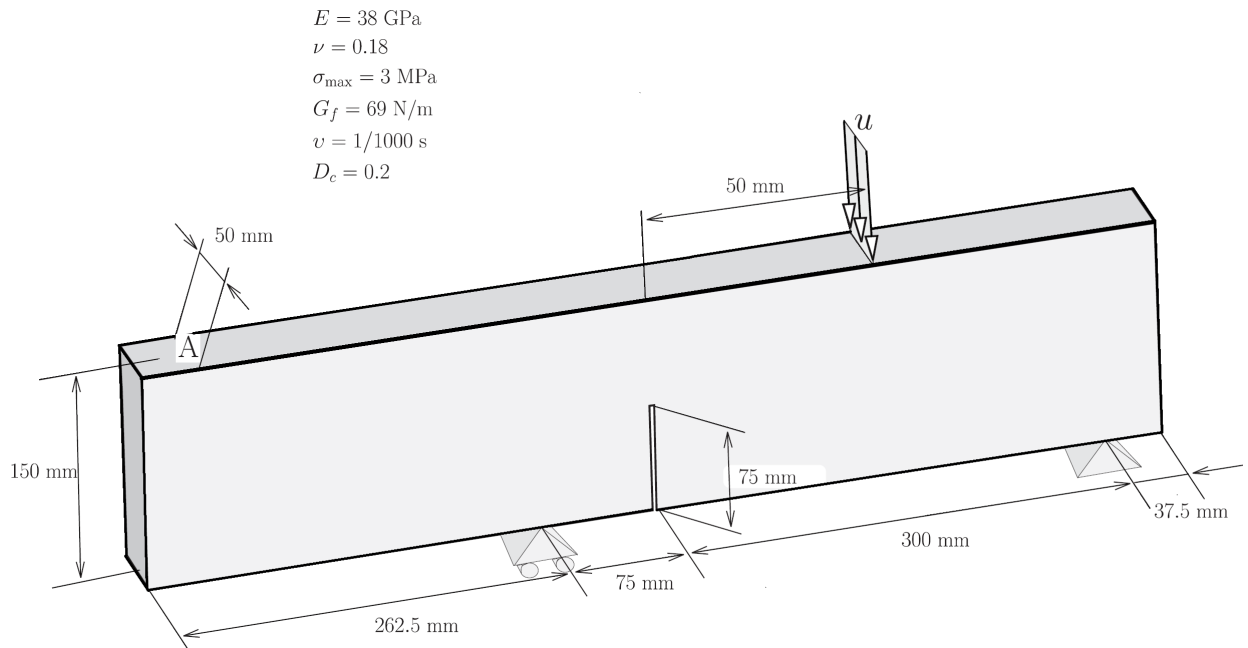


Figure 4.21: Geometry, loading and boundary condition for the three-dimensional Single edge notched beam.

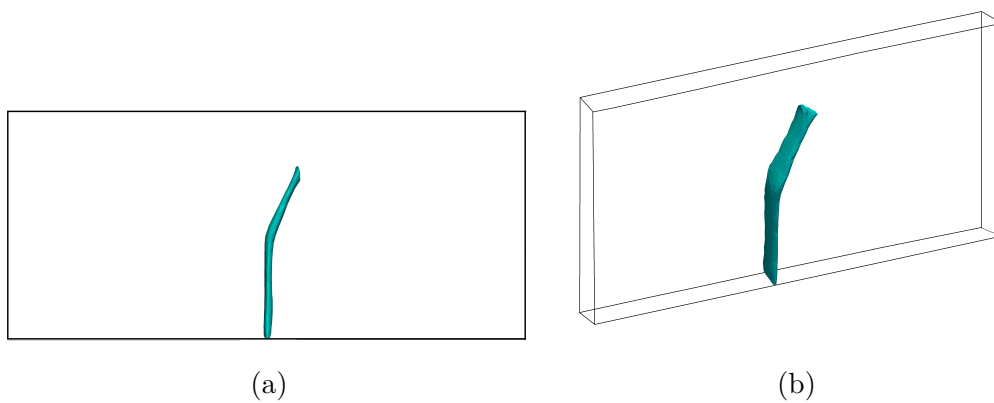


Figure 4.22: The crack path at two different views.

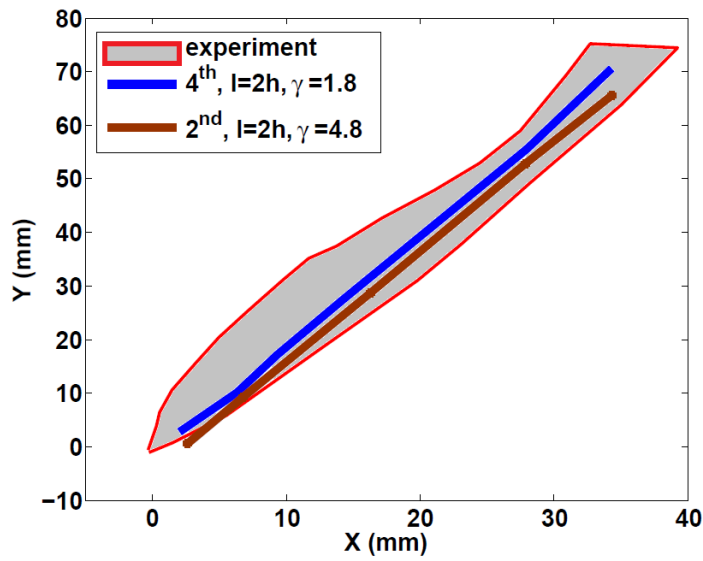


Figure 4.23: Crack path for the fourth and the second order phase field methods with $\gamma = 1.8$ and $\gamma = 4.8$ respectively, compared with the experiments in [1].

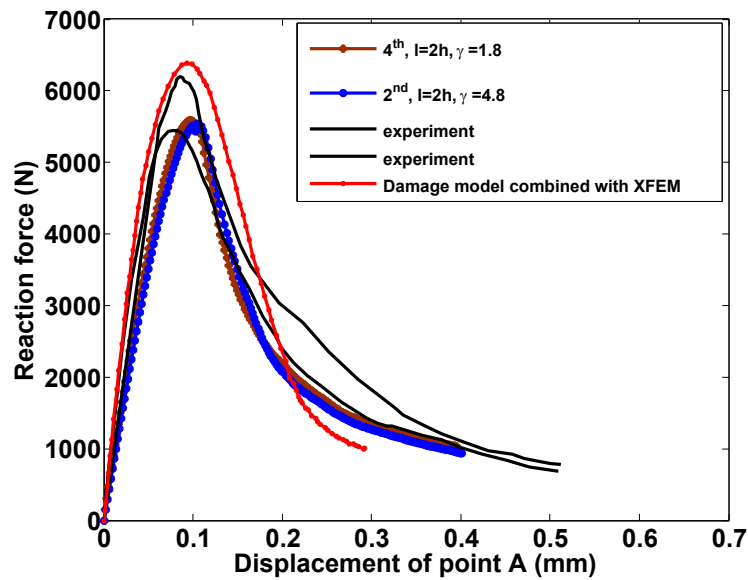


Figure 4.24: Reaction force displacement curve for point A, compared with [1, 2].

Non-planar crack growth

In this example, we consider a beam under bending which involves non-planar crack growth. The beam dimensions and the boundary condition are shown in Fig. 4.25. The

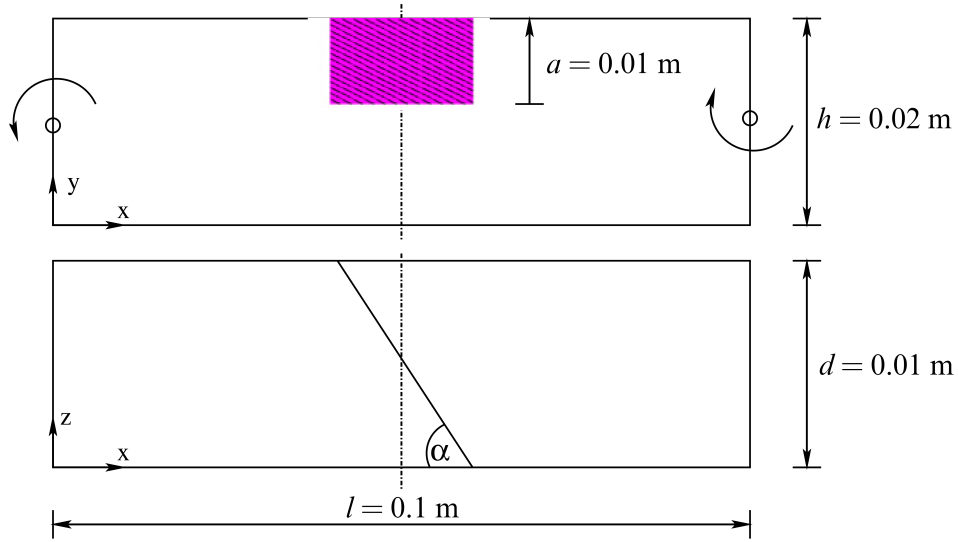


Figure 4.25: Side and top views of the beam with an initial crack for the non-planar crack growth.

beam is notched at an angle $\alpha = 45^\circ$ versus the x -axis, see Fig. 4.25. This example was also studied with the extended finite element method in [113] and meshfree method in [71]. They show that the crack surface, while propagating downwards, becomes finally orthogonal to the xz -plane.

We study the phase field method with numerical integration of an unstructured background mesh of 65456 tetrahedrons with the effective nodal spacing $h = 0.0018\text{mm}$ and $l_0 = 4h$. Here also discretization is refined in an area where the crack is expected to propagate. Fig. 4.26 illustrates the evolution of the crack front from a top view for the fourth order phase field method with $\gamma = 1.8$. The crack grows downwards and becomes orthogonal to the xz -plane. Fig. 4.27 shows the evolution of the crack front from a side view. The results are in good agreement with the results obtained in [71, 113]. The acceptable results have been obtained in [71], for 570000 and 4400000 particles (540000 and 4300000 stress points, respectively) and 65000 and 210000 particles for adaptive scheme. Similar results are obtained for the second order phase field model with $\gamma = 4.8$.



Figure 4.26: Evolution of the crack front in the beam seen from the top, the maximum and the minimum of phase field, i.e. $v = 1$ and $v = 0$ are shown.

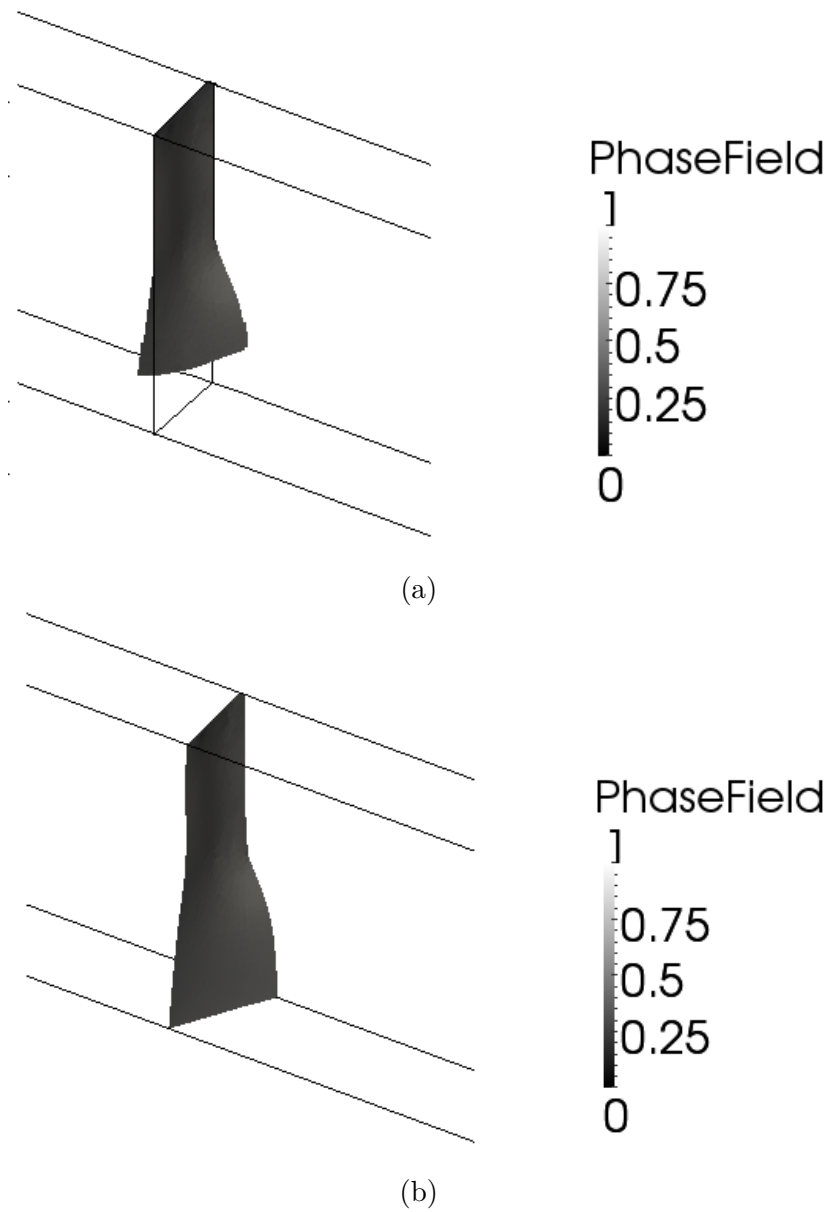


Figure 4.27: The crack path at the different stages of evolution from a side view, the maximum and the minimum of phase field, i.e. $v = 1$ and $v = 0$ are shown.

Chapter 5

Phase-field modeling of fracture mechanics in thin shells

Generally, a shell body is a three dimensional structure which is thinner in one direction compared to the other two directions. Shell structures are commonly found in nature, see Fig. 5.1 for some examples. Although thin and light, they span over large areas, and hold applied loads very effectively. With shell structures, nature has maximized the ability to cover over large areas with a minimum amount of material. Man-made structures inspired by nature, used this property to design thin structures which cover a wide area and hold large externally applied loads. For example, in civil engineering, thin shell structures are used for large roofs or elegant bridges and for the bodies of cars. In aeronautical engineering, airplane bodies and ship hulls are also shell structures. The thickness, curvature and of course the applied loads on shell structures play crucial roles in their behavior.

The fundamental shell theories have been studied in several contexts, such as [114, 115]. However, as we mentioned in the introduction section, in most cases obtaining a meaningful result from the analytical studies is impossible. During the last decades, numerical methods such as finite element methods, were developed for the analysis the mathematics model of shell. There are many challenges in the analysis of shell structures, due to the variety of behaviors and the difficulties of having to consider complex shells of arbitrary curvatures, material conditions, boundary supports, loading, and in particular of small thickness. Various shell finite element methods have been proposed by simply superimposing plate bending and plane stress membrane behaviors, but they have a limited level of accuracy. Later on, meshfree methods have been introduced to numerically model the shell structures. The smoothness of the shape

functions in meshfree method helped overcome the C^0 property of the finite element method.

Dealing computationally with the Kirchhoff-Love theory is challenging because second derivatives of the displacement field appear in the weak form, and therefore a Galerkin method requires C^1 -continuous basis functions. This can be overcome by discretizing the director field or introducing rotational degrees of freedom [116–118], or by considering more elaborate variational formulations such as in discontinuous Galerkin methods [119, 120]. Instead, here we focus on methods relying on smooth basis functions. Finite element methods with high order continuity have been proposed, either based on subdivision surfaces [70, 121] or on isogeometric analysis [122–124]. The higher order continuity of the meshfree basis functions has also been exploited for this purpose [61, 62], but since meshfree basis functions are defined in physical space, these methods were applied to simple geometries with a single parametric patch. Recently, nonlinear manifold learning techniques have been exploited to parametrize 2D sub-domains of a point-set surface, which are then used as parametric patches and glued together with a partition of unity [3, 79]. Here, we combine this methodology with local maximum-entropy (LME) meshfree approximants [77, 125, 126] because of their smoothness, robustness, and relative ease of quadrature compared with other meshfree approximants. In this dissertation, we study a method introduced by Millan and Arroyo to represent complex shell structures from a set of scattered points. Then, we combine this methodology with phase field method in order to model realistic crack in thin shell structures with complex geometry and topology.



Figure 5.1: Some thin shell structures are found in nature.

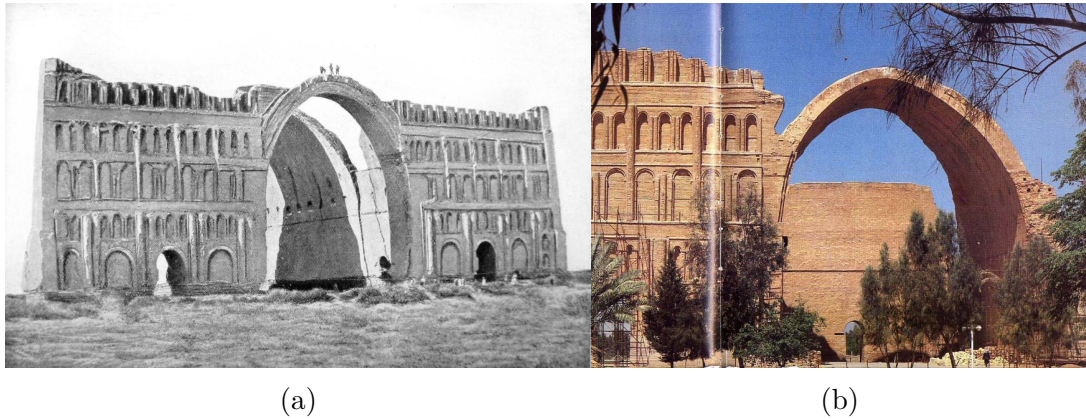


Figure 5.2: Tag Kasra: is a Sassanid-era Persian monument located near the modern town of Salman Pak, Iraq. It is the only visible remaining structure of the ancient city of Ctesiphon. The archway is the largest single-span vault of unreinforced brickwork in the world. Picture from 1864 (a), picture from 2003 (b).



Figure 5.3: Building made of shell structures, Valencia aquarium.

5.1 Dimensionality Reduction

As computer technology becomes more sophisticated, research in different areas such as engineering, astronomy, biology, and economics, must deal with increasingly large sets of data. To overcome this problem, dimensionality reduction methods, also known as manifold learning, have been developed. The goal of these methods to reduce the

dimensionality of a data set in which there are a large number of interrelated variables, while retaining as much as possible the variation present in the data set. In other words, for a given data set $X = \{x_1, x_2, \dots, x_N\} \subset R^D$, find a lower dimensional representation, $\Xi = \{\zeta_1, \zeta_2, \dots, \zeta_N\} \subset R^d$, such that $d \leq D$ and captures the content in the original data, according to some criterion. Generally, dimensionality reduction methods are classified in linear and nonlinear categories. The most common linear technique to perform dimensionality reduction was introduced in 1901 by Pearson [127]. It is also known by different names, such as Principal Components or Hotelling Transform [128], Karhunen-Loève Transform [129, 130], Empirical Orthogonal Functions [131] and Proper Orthogonal Decomposition [132]. Here we will refer to this method as Principal Component Analysis (PCA). A modern reference to this subject is [133]. Multidimensional Scaling (MDS) is another linear dimensionality reduction technique. PCA and MDS have successfully shown their capabilities to capture the Euclidean structure underlying data in many applications, but fail to produce compact and useful representations in others, likely because of the presence of strong nonlinear correlations. Nonlinear dimensionality reduction methods (NLDR) such as, isometric mapping (Isomap), locally linear embedding (LLE) and some subsequent modifications of LLE, such as Hessian LLE [134], or the Modified LLE method (MLLE)[135], have been developed over the last decades to address complex nonlinear problems. Fig. 5.4 indicates the dimensionality reduction results of an unstructured set of points sampling a swiss roll in 3D, by different method [3, 79]. The interested reader is referred to [3, 79] for full details. In this dissertation we use nonlinear dimensionality reduction method in the simulations to get more accurate results.

5.2 Manifold description from scattered points

To illustrate the method considered here for numerically representing surfaces defined by a set of scattered points, we refer to Fig. 5.5. As noted in [136], a fundamental difficulty in defining basis functions and performing calculations on a surface, as compared to open sub-sets in Euclidean space, is the absence in general of a single parametric domain. A simple example is the sphere, which does not admit a single singularity-free parametrization. Mesh-based methods, consisting of a collection of local parametrizations from the parent element to the physical elements, do not have any difficulty in this respect at the expense of reduced smoothness across the element boundaries or the need for special techniques to recover inter-element smoothness. In meshfree methods, such a natural parametric domain is not available, and the descrip-

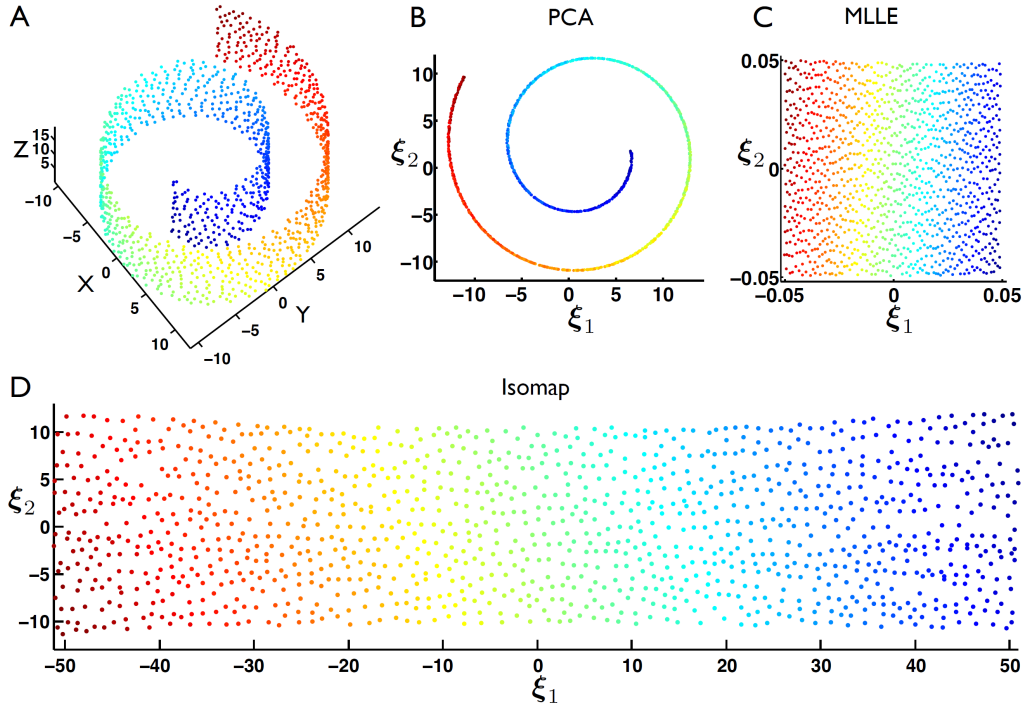


Figure 5.4: Swiss roll benchmark in dimensionality reduction. (A) Sampling in 3D by an unstructured set of points. Two-dimensional embeddings obtained with PCA (B), MLE (C), and Isomap (D). Color is used to identify the location of the points. PCA fails because the sampled manifold is not unfolded and the points collapse in a line [3].

tion of surfaces with a topology different to that of an open set in \mathbb{R}^2 , such as a sphere (A) or a set of connected pipes (B), is a challenge. Even for surfaces homeomorphic to open two-dimensional sets, such as that depicted in (C), the geometric complexity can make it very difficult to produce well-behaved global parametrizations. For these reasons, the method we follow here proceeds in four steps: (1) We first partition the set of scattered points into subsets. (2) For each subset, the geometric structure of the surface is detected by dimensionality reduction methods and its points are embedded in 2D. (3) The 2D embedding then serves as a local parametric patch, and a local parametrization of the surface using smooth meshfree LME approximants is defined. (4) Finally, the different patches are glued together by means of a partition of unity.

Consider a smooth surface \mathcal{M} embedded in \mathbb{R}^3 and represented by a set of (control) points $P = \{\mathbf{P}_1, \mathbf{P}_2, \dots, \mathbf{P}_N\} \subset \mathbb{R}^3$. The goal is to numerically represent \mathcal{M} from P and make computations on it. We consider another set $Q = \{\mathbf{Q}_1, \mathbf{Q}_2, \dots, \mathbf{Q}_M\} \subset \mathbb{R}^3$ with fewer point, typically a subset of P but not necessarily. We call the points of this set geometric markers. For simplicity, we will denote the points in P and its associated objects with a lower case subindex, e.g. \mathbf{P}_a , for $a = 1, 2, \dots, N$, and the geometric

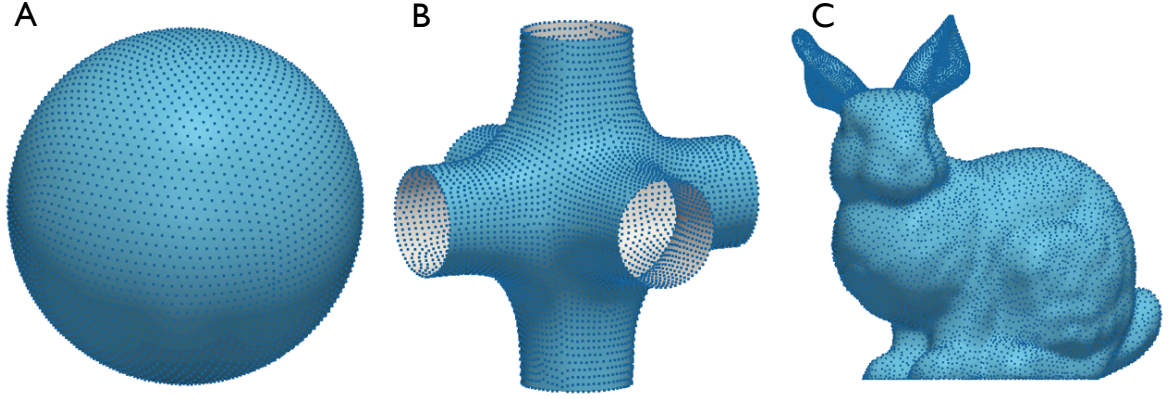


Figure 5.5: Three point-set surfaces that require partitioning for different reasons: (A) and (B) for their non-trivial topology, and (C) for its complex geometry.

markers in Q and its associated objects with an upper case subindex, e.g. \mathbf{Q}_A , for $A = 1, 2, \dots, M$.

We partition these geometric markers into L groups, we use the METIS library to partition the data [137]. These L groups of geometric markers can be represented with index sets $\mathcal{I}_\kappa, \kappa = 1, \dots, L$ with $\cup_{\kappa=1}^L \mathcal{I}_\kappa = \{1, 2, \dots, M\}$ and $\mathcal{I}_\kappa \cap \mathcal{I}_\iota = \emptyset$ such that $\kappa \neq \iota$. As it will become clear below, there is a one-to-one correspondence between these groups of geometric markers and the local parameterizations of the surface, which here we refer as patches.

We consider a Shepard partition of unity associated with the geometric markers. Given a set of non-negative reals $\{\beta_A\}_{A=1,2,\dots,M}$, we define the Shepard partition of unity with Gaussian weight associated to the set Q as

$$w_A(\mathbf{x}) = \frac{\exp(-\beta_A |\mathbf{x} - \mathbf{Q}_A|^2)}{\sum_{B=1}^M \exp(-\beta_B |\mathbf{x} - \mathbf{Q}_B|^2)}. \quad (5.1)$$

To obtain a coarser partition of unity representative of a partition, we aggregate the partition of unity functions as

$$\psi_\kappa(\mathbf{x}) = \sum_{A \in \mathcal{I}_\kappa} w_A(\mathbf{x}). \quad (5.2)$$

These functions form a partition of unity in \mathbb{R}^D , and consequently also in \mathcal{M} . We consider the index sets of all control points influencing each patch, \mathcal{J}_κ , with $\cup_{\kappa=1}^L \mathcal{J}_\kappa = \{1, 2, \dots, N\}$, but now $\mathcal{J}_\kappa \cap \mathcal{J}_\iota \neq \emptyset$ due to the overlap between patch partition of unity functions. Roughly speaking, these sets are $\{a \mid \mathbf{P}_a \in \text{supp } \psi_\kappa\}$, slightly enlarged so that the patch parameterization is smooth on the boundary of the support of ψ_κ .

For each patch through a nonlinear dimensionality reduction technique, the MLE method combined with the affine isometric correction, applied to the set of control points $P_\kappa = \{\mathbf{P}_a\}_{a \in \mathcal{J}_\kappa} \subset \mathbb{R}^3$, we obtain a two-dimensional embedding of these points, represented by the set $\Xi_\kappa = \{\boldsymbol{\xi}_a\}_{a \in \mathcal{J}_\kappa} \subset \mathbb{R}^2$. The two-dimensional region defined by these points is a convenient parametric space for the corresponding patch. It is important to note that the embedded points are in general unstructured, and that, although here $d = 2$, the methodology is applicable to higher dimensional embedded manifolds unlike mesh based techniques.

The patch parametrizations often need to be smooth, here because of the requirements of the Kirchhoff-Love theory. We consider here LME basis functions. Then, let $p_a(\boldsymbol{\xi})$ denote the LME approximants associated to the point-set Ξ_κ on a domain $\mathcal{A}_\kappa \subset \mathbb{R}^2$, a subset of the convex hull of the reduced node set $\text{conv } \Xi_\kappa$. We locally parameterize the manifold in this patch as

$$\begin{aligned} \boldsymbol{\varphi}_\kappa : \mathcal{A}_\kappa &\longrightarrow \mathbb{R}^3 \\ \boldsymbol{\xi} &\longmapsto \sum_{a \in \mathcal{J}_\kappa} p_a(\boldsymbol{\xi}) \mathbf{P}_a. \end{aligned} \quad (5.3)$$

Consider a function f over a surface \mathcal{M} , $f : \mathcal{M} \rightarrow \mathbb{R}$. The integral of this function over the surface can be split into integrals over the patches invoking the partition of unity

$$\int_{\mathcal{M}} f(\mathbf{x}) d\mathcal{M} \simeq \sum_{\kappa=1}^L \int_{\mathcal{A}_\kappa} \psi_\kappa(\boldsymbol{\varphi}_\kappa(\boldsymbol{\xi})) f(\boldsymbol{\varphi}_\kappa(\boldsymbol{\xi})) J_\kappa(\boldsymbol{\xi}) d\boldsymbol{\xi}, \quad (5.4)$$

where $J_\kappa = \sqrt{\det[(D\boldsymbol{\varphi}_\kappa)^T D\boldsymbol{\varphi}_\kappa]}$ is the Jacobian determinant of the parameterization. In this way, similarly to finite element methods, we have split the integral into local contributions, which can be evaluated using local parameterizations. Each patch integral can be approximated by numerical quadrature on the local parametric space, for instance we resort to Gauss quadrature on a support triangulation defined over Ξ_κ .

5.3 Thin shell model

In this section, we review the mechanics of thin shells [84, 138], based on a geometrically exact formulation presented in [117, 139]. We restrict our attention to the Kirchhoff-Love kinematical assumption of shells, which states that the material line orthogonal to the middle surface in the undeformed configuration remains straight, unstretched and always orthogonal to the middle surface during the deformations. Furthermore,

we follow the usual convention for Latin and Greek indices, referring to Cartesian and curvilinear coordinates, respectively (i.e. $i = 1, 2, 3$; $\alpha = 1, 2$). A comma denotes partial derivatives, subscripts refer to covariant components, and superscripts denote contravariant components.

5.3.1 Kinematics of the shell

We consider a shell with a middle surface Ω , defined by $\boldsymbol{\varphi}$ which is a mapping from the parametric space of \mathbb{R}^2 , denoted by \mathcal{A} , into Ω . Assume \mathbf{t} is a field of unit vectors (a field of directors). Thus, the thin shell body $\mathcal{S} \subset \mathbb{R}^3$ in three dimension can be described by the pair $(\boldsymbol{\varphi}, \mathbf{t})$, see Fig. 5.6. Additionally, the subscript 0 denotes quantities in the reference configuration, for instance $\boldsymbol{\varphi}_0$ parametrizes the reference middle surface. We assume the thickness t of the shell to be uniform for simplicity, and also we assume that the change in shell thickness after deformation is negligible. Then, the thin shell body \mathcal{S} is given by

$$\mathcal{S} = \left\{ \boldsymbol{\Phi} \in \mathbb{R}^3 \mid \boldsymbol{\Phi} = \boldsymbol{\varphi}(\xi^1, \xi^2) + \xi \mathbf{t}(\xi^1, \xi^2), -\frac{t}{2} \leq \xi \leq \frac{t}{2}, (\xi^1, \xi^2) \in \mathcal{A} \right\}, \quad (5.5)$$

where $\mathcal{A} \subset \mathbb{R}^2$ is the parametric space for the middle surface. Hence, the configuration $\boldsymbol{\Phi}$ is a mapping from a parametric domain $\mathcal{A} \times [-t/2, t/2]$ into \mathbb{R}^3 . The coordinates $\{\xi^1, \xi^2, \xi^3\}$ (where $\xi = \xi^3$) describe this parametric domain, which corresponding global Cartesian basis of these coordinates is $\{\mathbf{E}_k\}$. The area element of the middle surface can be computed as $d\Omega = \bar{j} d\xi^1 d\xi^2$, where $\bar{j} = |\boldsymbol{\varphi}_{,1} \times \boldsymbol{\varphi}_{,2}|$.

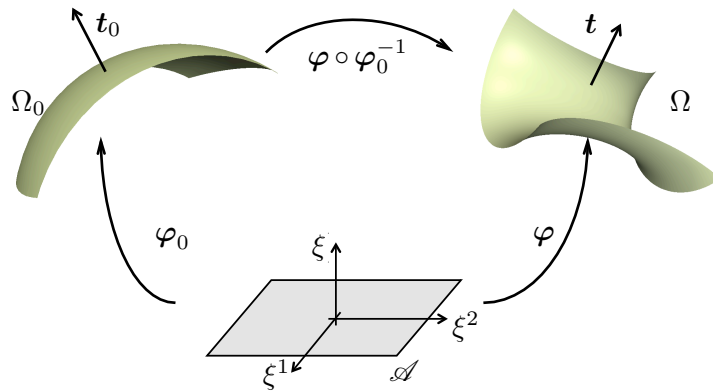


Figure 5.6: Reference and the deformed configurations of the middle shell surface.

The convective basis vectors \mathbf{g}_i can be defined by the tangent map as

$$\nabla \boldsymbol{\Phi} = \frac{\partial \boldsymbol{\Phi}}{\partial \xi^i} \otimes \mathbf{E}^i = \mathbf{g}_i \otimes \mathbf{E}^i,$$

with $\mathbf{g}_\alpha = \frac{\partial \Phi}{\partial \xi^\alpha} = \boldsymbol{\varphi}_{,\alpha} + \xi \mathbf{t}_{,\alpha}$ and $\mathbf{g}_3 = \frac{\partial \Phi}{\partial \xi} = \mathbf{t}$. The covariant components of the metric tensor in convected coordinates are given by $g_{ij} = \mathbf{g}_i \cdot \mathbf{g}_j$. The difference between the metric tensors of the undeformed and deformed configurations of the shell is measured by the Green–Lagrange strain tensor, i.e.

$$E_{ij} = \frac{1}{2} (g_{ij} - g_{0ij}) = \frac{1}{2} (\Phi_{,i} \cdot \Phi_{,j} - \Phi_{0,i} \cdot \Phi_{0,j}).$$

According to the Kirchhoff–Love theory of thin shells, we constrain the deformed director \mathbf{t} to coincide with the unit normal of the deformed middle surface of the shell, i.e.

$$\mathbf{t} = \frac{\boldsymbol{\varphi}_{,1} \times \boldsymbol{\varphi}_{,2}}{j}, \quad \boldsymbol{\varphi}_{,\alpha} \cdot \mathbf{t} = 0, \quad |\mathbf{t}| = 1, \quad \mathbf{t} \cdot \mathbf{t}_{,\alpha} = 0. \quad (5.6)$$

We assume that the deformation field for the shell is restricted to account only for small displacement. For more details, refer to [3, 79]. With the Kirchhoff–Love and the small deformation hypothesis, the only remaining non-zero components of the Green–Lagrange strain tensor are

$$E_{\alpha\beta} = \varepsilon_{\alpha\beta} + \xi \rho_{\alpha\beta}, \quad (5.7)$$

where $\varepsilon_{\alpha\beta} = \frac{1}{2} (\boldsymbol{\varphi}_{,\alpha} \cdot \boldsymbol{\varphi}_{,\beta} - \boldsymbol{\varphi}_{0,\alpha} \cdot \boldsymbol{\varphi}_{0,\beta})$ is the membrane strain tensor and $\rho_{\alpha\beta} = \boldsymbol{\varphi}_{,\alpha} \cdot \mathbf{t}_{,\beta} - \boldsymbol{\varphi}_{0,\alpha} \cdot \mathbf{t}_{0,\beta}$ is a tensor that measures the bending or change in curvature of the shell. Thus, the Kirchhoff–Love kinematic assumption leads to a formulation of the shell exclusively in terms of the middle surface. We refer to the Appendix C for a detailed computation of the Green–Lagrange strain tensor.

5.3.2 Thin shell potential energy

The potential energy of an elastic thin shell body under Kirchhoff–Love assumptions can be expressed by the functional

$$\Pi[\mathbf{u}] = \int_{\Omega_0} \mathcal{W}(\mathbf{u}) \, d\Omega_0 + \Pi_{\text{ext}}[\mathbf{u}], \quad (5.8)$$

where Ω_0 is the reference middle surface of the thin shell body, \mathcal{W} is an internal energy density per unit area, and Π_{ext} is the potential energy of the external loads.

For an isotropic Kirchhoff–St. Venant elastic material the internal energy density is given by:

$$\mathcal{W} = \frac{1}{2} C^{\alpha\beta\gamma\delta} \left(t \varepsilon_{\alpha\beta} \varepsilon_{\gamma\delta} + \frac{t^3}{12} \rho_{\alpha\beta} \rho_{\gamma\delta} \right),$$

with

$$C^{\alpha\beta\gamma\delta} = \frac{E}{(1-\nu^2)} \left[\nu a_0^{\alpha\beta} a_0^{\gamma\delta} + \frac{1}{2}(1-\nu) (a_0^{\alpha\gamma} a_0^{\beta\delta} + a_0^{\alpha\delta} a_0^{\beta\gamma}) \right],$$

where we have introduced the first fundamental form $a_{\alpha\beta} = \boldsymbol{\varphi}_{,\alpha} \cdot \boldsymbol{\varphi}_{,\beta}$ expressed in convected components, with $a_0^{\alpha\gamma} (a_0)_{\gamma\beta} = \delta_\beta^\alpha$. E is the Young's modulus, and ν is the Poisson's ratio [3, 79].

The external potential energy expressed in the reference middle surface is stated as:

$$\Pi_{\text{ext}}[\mathbf{u}] = - \int_{\Omega_0} \mathbf{q} \cdot \mathbf{u} \, d\Omega_0 - \int_{\partial\Omega_0} \mathbf{h} \cdot \mathbf{u} \, d\eta_0,$$

where \mathbf{q} is the external body load per unit area, \mathbf{h} the forces per unit length applied on the boundary of the middle surface, and $d\eta_0$ is the line element of the boundary of the middle surface.

5.3.3 Phase-field model for thin shell structures

Let us consider a thin shell model that assumes the phase-field to be constant across the thickness. The total potential energy functional for a thin shell body with crack (elastic and surface energies) is given by

$$\Pi[\mathbf{u}, v] = \int_{\Omega_0} (v^2 + \epsilon) \mathcal{W}(\mathbf{u}) \, d\Omega_0 + \int_{\Omega_0} G_c t \left[\frac{(1-v)^2}{4\ell} + \ell |\nabla v|^2 \right] d\Omega_0 + \Pi_{\text{ext}}[\mathbf{u}], \quad (5.9)$$

where v is phase-field describing uniform cracks through the thickness, G_c is the critical energy release rate, or surface energy, in Griffith's theory, and ℓ is a positive regularization constant to regulate the size of the fracture zone. As ℓ tends to zero, the phase-field approximation of the fracture energy converges to the fracture energy.

For an accurate discretized surface energy, the nodal spacing of the discretization h should be smaller than the regularization parameter ℓ , i.e. $h/\ell \ll 1$. Moreover, the crack area, which is controlled by ℓ , should be smaller than the domain area, in order to approximate the sharp-interface model. Numerical experiments illustrate that setting $2h \sim \ell$ still gives reasonable results. However, the computed surface energy will be slightly overestimated.

The natural boundary conditions are used for v . The crack is assumed to be traction-free. In order to satisfy this condition the internal energy density \mathcal{W} is multiplied by the jump set function $(v^2 + \epsilon)$. The parameter $\epsilon \ll 1$ is introduced to avoid the singularity of disappearing internal energy density when the phase-field parameter is zero. To avoid crack healing, we impose $v^i \leq v^{i-1}$ constraint on phase field solution of

each step. Here v^{i-1} and v^i are the phase-field parameters at step $i - 1$ and i [109].

The first variation of the functional $\Pi[\mathbf{u}, v]$ is given by

$$\delta\Pi = \delta\Pi_{\text{int}} + \delta\Pi_{\text{ext}} = 0.$$

Since the variations $\delta\mathbf{u}$ and δv are independent, the above expression leads to two decoupled equations

$$\delta\Pi[\mathbf{u}, v, \delta\mathbf{u}] = \int_{\mathcal{A}} (v^2 + \epsilon) C^{\alpha\beta\gamma\delta} \left(t \varepsilon_{\gamma\delta}(\mathbf{u}) \varepsilon_{\alpha\beta}(\delta\mathbf{u}) + \frac{t^3}{12} \rho_{\gamma\delta}(\mathbf{u}) \rho_{\alpha\beta}(\delta\mathbf{u}) \right) \bar{j}_0 d\xi^1 d\xi^2 + \delta\Pi_{\text{ext}}[\delta\mathbf{u}] = 0, \quad (5.10)$$

$$\delta\Pi[\mathbf{u}, v, \delta v] = \int_{\mathcal{A}} 2v\delta v \mathcal{W}(\mathbf{u}) \bar{j}_0 d\xi^1 d\xi^2 + 2 \int_{\mathcal{A}} t G_c \left(-\frac{(1-v)\delta v}{4\ell} + \ell \nabla v \nabla(\delta v) \right) \bar{j}_0 d\xi^1 d\xi^2 = 0, \quad (5.11)$$

with the external virtual work

$$\delta\Pi_{\text{ext}}[\delta\mathbf{u}] = - \int_{\mathcal{A}} \mathbf{q} \cdot \delta\mathbf{u} \bar{j}_0 d\xi^1 d\xi^2 - \int_{\partial\mathcal{A}} \mathbf{h} \cdot \delta\mathbf{u} \|\boldsymbol{\varphi}_{0,t}\| d\eta_\xi. \quad (5.12)$$

With the strategy presented in Section 5.2, we can split the expressions stated by the principle of virtual work into partition contributions, that is

$$\begin{aligned} \delta\Pi[\mathbf{u}, v, \delta\mathbf{u}] &= \sum_{\kappa=1}^L \int_{\mathcal{A}_\kappa} \left[(v^2 + \epsilon) C^{\alpha\beta\gamma\delta} \left(t \varepsilon_{\gamma\delta}(\mathbf{u}) \varepsilon_{\alpha\beta}(\delta\mathbf{u}) + \frac{t^3}{12} \rho_{\gamma\delta}(\mathbf{u}) \rho_{\alpha\beta}(\delta\mathbf{u}) \right) \bar{j}_0 \right]_{\kappa} (\psi_\kappa \circ \boldsymbol{\varphi}_0) d\xi^1 d\xi^2 \\ &\quad - \sum_{\kappa=1}^L \int_{\mathcal{A}_\kappa} [\mathbf{q} \cdot \delta\mathbf{u} \bar{j}_0]_{\kappa} (\psi_\kappa \circ \boldsymbol{\varphi}_0) d\xi^1 d\xi^2 - \sum_{\kappa=1}^L \int_{\partial\mathcal{A}_\kappa} [\mathbf{h} \cdot \delta\mathbf{u} \|\boldsymbol{\varphi}_{0,t}\|]_{\kappa} (\psi_\kappa \circ \boldsymbol{\varphi}_0) d\eta_\xi = 0, \end{aligned} \quad (5.13)$$

and

$$\begin{aligned} \delta\Pi[\mathbf{u}, v, \delta v] &= \sum_{\kappa=1}^L \int_{\mathcal{A}_\kappa} \left[\left(2\mathcal{W}(\mathbf{u}) + \frac{t G_c}{2\ell} \right) v \delta v \bar{j}_0 \right]_{\kappa} (\psi_\kappa \circ \boldsymbol{\varphi}_0) d\xi^1 d\xi^2 \\ &\quad + \sum_{\kappa=1}^L \int_{\mathcal{A}_\kappa} 2 \left[t G_c \ell \left(\frac{\partial v}{\partial \xi^\alpha} g^{\alpha\beta} \frac{\partial(\delta v)}{\partial \xi^\beta} \right) \bar{j}_0 \right]_{\kappa} (\psi_\kappa \circ \boldsymbol{\varphi}_0) d\xi^1 d\xi^2 \\ &\quad - \sum_{\kappa=1}^L \int_{\mathcal{A}_\kappa} \left[\frac{t G_c}{2\ell} \delta v \bar{j}_0 \right]_{\kappa} (\psi_\kappa \circ \boldsymbol{\varphi}_0) d\xi^1 d\xi^2 = 0, \end{aligned} \quad (5.14)$$

such that $g^{\alpha\gamma} g_{\gamma\beta} = \delta_\beta^\alpha$. Here, $[\cdot]_\kappa$ means that the expression within the brackets is evaluated with the κ -th partition approximation of the undeformed middle surface.

5.3.4 Galerkin discretization

We consider now the discrete equilibrium equations for a shell whose middle surface in the reference configuration is numerically represented with the procedure described before, in terms of a set of nodes $P_0 = \{\mathbf{P}_{01}, \dots, \mathbf{P}_{0N}\}$, and a set of L patches. We follow a total Lagrangian approach, with the same parameter space and basis functions for the reference and deformed configurations. Let $\varphi_{0\kappa}$ be the reference configuration mapping for the middle surface of a specific part κ , defined over the parametric space \mathcal{A}_κ

$$\varphi_{0\kappa}(\boldsymbol{\xi}) = \sum_{a \in \mathcal{J}_\kappa} p_a(\boldsymbol{\xi}) \mathbf{P}_{0a}, \quad (5.15)$$

We represent the deformed configuration in a given partition κ as

$$\mathbf{u}_\kappa(\boldsymbol{\xi}) = \sum_{a \in \mathcal{J}_\kappa} p_a(\boldsymbol{\xi}) \mathbf{u}_a, \quad (5.16)$$

and the approximation of the phase-field parameter, v , as

$$v_\kappa(\boldsymbol{\xi}) = \sum_{a \in \mathcal{J}_\kappa} q_a(\boldsymbol{\xi}) v_a, \quad (5.17)$$

where $p_a(\boldsymbol{\xi})$ and $q_a(\boldsymbol{\xi})$ are LME basis functions. Virtual displacements and virtual phase-field parameters are represented likewise. A simple calculation yields the Galerkin stiffness matrix. The interaction between nodes a and b is given by

$$\mathbf{K}_u^{ab} = \sum_{\kappa=1}^L \int_{\mathcal{A}_\kappa} \left[(v^2 + \epsilon) \left({}_t \mathbf{M}^{aT} \mathbf{C} \mathbf{M}^b + \frac{t^3}{12} \mathbf{B}^{aT} \mathbf{C} \mathbf{B}^b \right) \bar{j}_0 \right]_\kappa (\psi_\kappa \circ \varphi_0) d\xi^1 d\xi^2,$$

where \mathbf{M}^a and \mathbf{B}^a are the membrane and bending strain-displacement matrices for the a -th node. For a specific patch such as A , we have

$$M_{ij}^a = \mathbf{M}_i^a \cdot \mathbf{e}_j \quad \text{and} \quad B_{ij}^a = \mathbf{B}_i^a \cdot \mathbf{e}_j,$$

where

$$\begin{aligned}
\mathbf{M}_\alpha^a &= p_{a,\alpha} \boldsymbol{\varphi}_{0,\alpha}, \\
\mathbf{M}_3^a &= p_{a,2} \boldsymbol{\varphi}_{0,1} + p_{a,1} \boldsymbol{\varphi}_{0,2}, \\
\mathbf{B}_\alpha^a &= -p_{a,\alpha\alpha} \mathbf{t}_0 \\
&\quad + \bar{j}_0^{-1} [(\boldsymbol{\varphi}_{0,\alpha\alpha} \times \boldsymbol{\varphi}_{0,2}) p_{a,1} + (\boldsymbol{\varphi}_{0,1} \times \boldsymbol{\varphi}_{0,\alpha\alpha}) p_{a,2}] \\
&\quad + \bar{j}_0^{-1} (\mathbf{t}_0 \cdot \boldsymbol{\varphi}_{0,\alpha\alpha}) [(\boldsymbol{\varphi}_{0,2} \times \mathbf{t}_0) p_{a,1} + (\mathbf{t}_0 \times \boldsymbol{\varphi}_{0,1}) p_{a,2}], \\
\mathbf{B}_3^a &= -2 p_{a,12} \mathbf{t}_0 \\
&\quad + 2 \bar{j}_0^{-1} [(\boldsymbol{\varphi}_{0,12} \times \boldsymbol{\varphi}_{0,2}) p_{a,1} + (\boldsymbol{\varphi}_{0,1} \times \boldsymbol{\varphi}_{0,12}) p_{a,2}] \\
&\quad + 2 \bar{j}_0^{-1} (\mathbf{t}_0 \cdot \boldsymbol{\varphi}_{0,12}) [(\boldsymbol{\varphi}_{0,2} \times \mathbf{t}_0) p_{a,1} + (\mathbf{t}_0 \times \boldsymbol{\varphi}_{0,1}) p_{a,2}],
\end{aligned}$$

Note that $\mathbf{M}^a, \mathbf{B}^a \in \mathbb{R}^{3 \times 3}$ and the repeated indices in the expressions for \mathbf{M}_α^a and \mathbf{B}_α^a do not imply summation, see [79] for a detailed description. The force contribution of the a -th node is

$$\mathbf{f}_u^a = \sum_{\kappa=1}^L \int_{\mathcal{A}_\kappa} [\mathbf{q} p_a \bar{j}_0]_\kappa (\psi_\kappa \circ \boldsymbol{\varphi}_0) d\xi^1 d\xi^2 + \sum_{\kappa=1}^L \int_{\partial \mathcal{A}_\kappa} [\mathbf{h} p_a \|\boldsymbol{\varphi}_{0,t}\|]_\kappa (\psi_\kappa \circ \boldsymbol{\varphi}_0) d\eta_\xi.$$

Finally, the phase-field stiffness matrix is

$$\mathbf{K}_v^{ab} = \sum_{\kappa=1}^L \int_{\mathcal{A}_\kappa} \left[\left(2\mathcal{W}(\mathbf{u}) + \frac{t G_c}{2\ell} \right) q_a q_b \bar{j}_0 + 2 \ell t G_c q_{a,\alpha} q_{b,\beta} g^{\alpha\beta} \bar{j}_0 \right]_\kappa (\psi_\kappa \circ \boldsymbol{\varphi}_0) d\xi^1 d\xi^2, \quad (5.18)$$

and the right hand side for phase-field is

$$\mathbf{f}_v^a = \sum_{\kappa=1}^L \int_{\mathcal{A}_\kappa} \frac{t G_c}{2\ell} [q_a \bar{j}_0]_\kappa (\psi_\kappa \circ \boldsymbol{\varphi}_0) d\xi^1 d\xi^2. \quad (5.19)$$

The Dirichlet displacement and rotation boundary conditions are imposed with Lagrange multipliers, the interested reader is referred to [32, 79, 140, 141].

5.4 Numerical results

5.4.1 Single edge notch tensile

To get a better understanding of the proposed methodology, we consider a well studied benchmark example of $2D$ solid under plane stress state [142, 143]. The plane is a square of edge length $L = 1$ mm, under pure tension with initial crack (see sketch in Fig. 5.7). The crack is replaced at the middle of the plane edge with length $L/2$ and width of $2h$. The elastic constants are chosen as $E = 10^9$ N/mm² and $\nu = 0.3$, the

critical energy release rate as $G_c = 1$ N/mm and $\epsilon = 10^{-6}$. The constant displacement increments $\Delta u = 0.5 \times 10^{-6}$ mm, are used for each step of computation.

The results are indicated in Figs. 5.8, 5.9, 5.10 and 5.11 for a uniform discretization with nodal spacing $h = 0.005$. The crack path is illustrated in Fig. 5.8. As it was expected, the crack propagates in a symmetry path [105]. For fixed regularization parameter $\ell = 0.05$ mm, the influence of the different values of γ for the LME approximants, is analyzed. Fig. 5.9 depicts the load-deflection curves for FEM and LME with different values of γ . The same results are observed for LME with $\gamma \geq 1.8$ and FEM, while $\gamma \leq 0.8$ gives less accurate result, due to the wider and smoother LME shape functions. Therefore, the LME results converge to the standard FEM results as γ increases [77]. The subsequent study analyzes the influence of the critical energy release rate G_c . The energy release rate, G , is the rate of change in potential energy with crack area. The crack extension occurs when G reaches a critical value G_c . Hence, as G_c decreases the material are more brittle and reaction force is lower. Figs. 5.10, 5.11 illustrate the load-deflection curves for different values of G_c , $\gamma = 1.8$, $\ell = 0.05$ and $\ell = 0.025$. It is obvious from these figures as G_c increases the area under the load-deflection curve appends. Fig. 5.12 indicates load-deflection curves for different discretization with nodal spacing $h = 0.0204, 0.0101, 0.005$. In this figure for fine mesh, $h \leq 0.0101$, the results are mesh-independent, which conform the results obtained by [105].

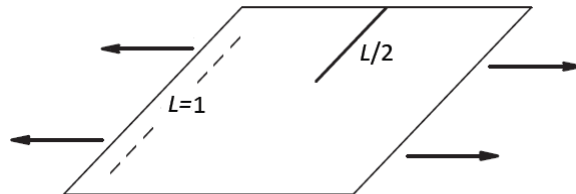


Figure 5.7: Square plate of side length $L = 1$ mm with initial crack of length $L/2$ under pure tension.

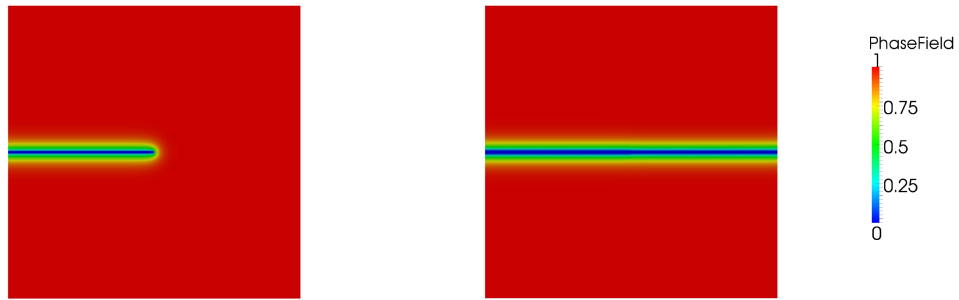


Figure 5.8: (Left) initial phase-field parameter values with initial crack width of $2h$, (right) phase-field solution of the plate for the final state after full breaking.

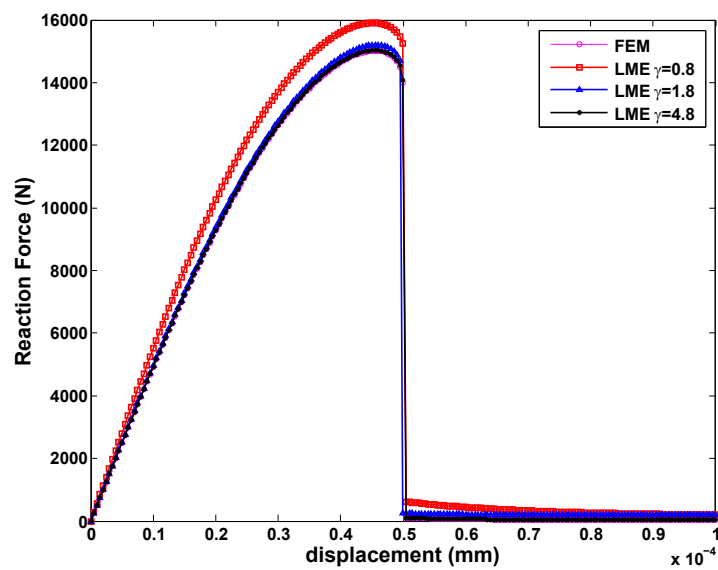


Figure 5.9: Load-deflection curves for FEM and LME with $\gamma = 0.8, 1.8$ and 4.8 .

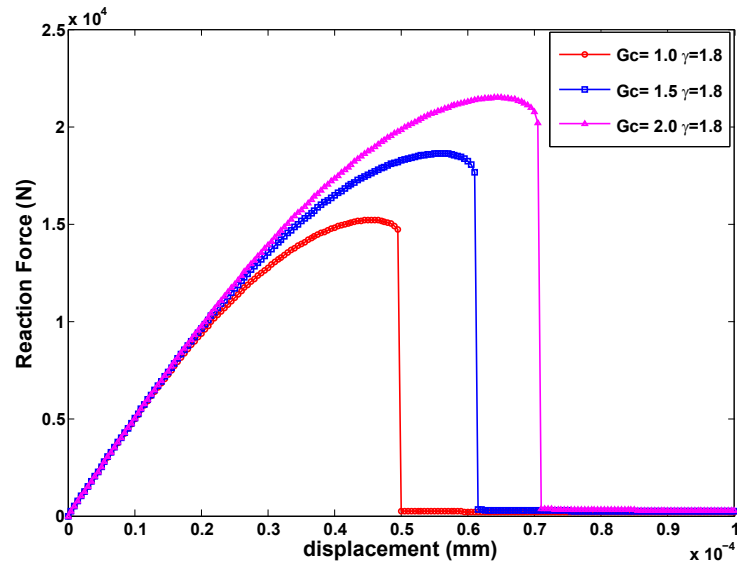


Figure 5.10: Load-deflection curves for $h = 0.005$, $G_c = 1.0, 1.5, 2.0$ N/mm, $\ell = 0.05$ mm and $\gamma = 1.8$.

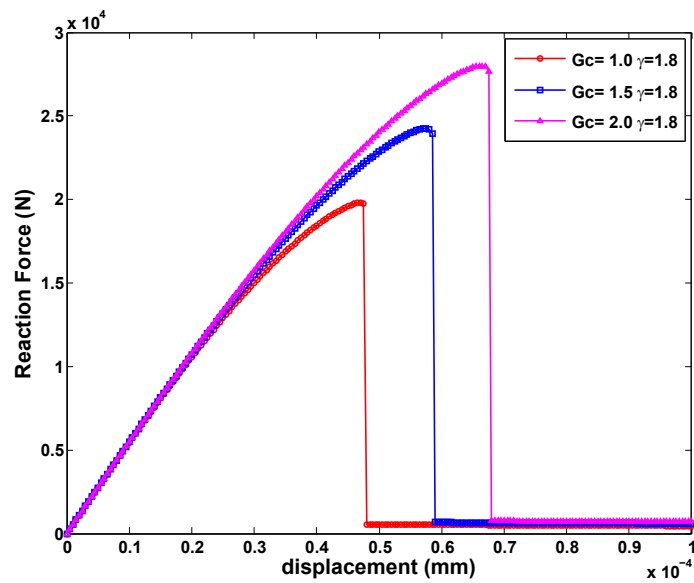


Figure 5.11: Load-deflection curves for $h = 0.005$, $G_c = 1.0, 1.5, 2.0$ N/mm, $\ell = 0.025$ mm and $\gamma = 1.8$.

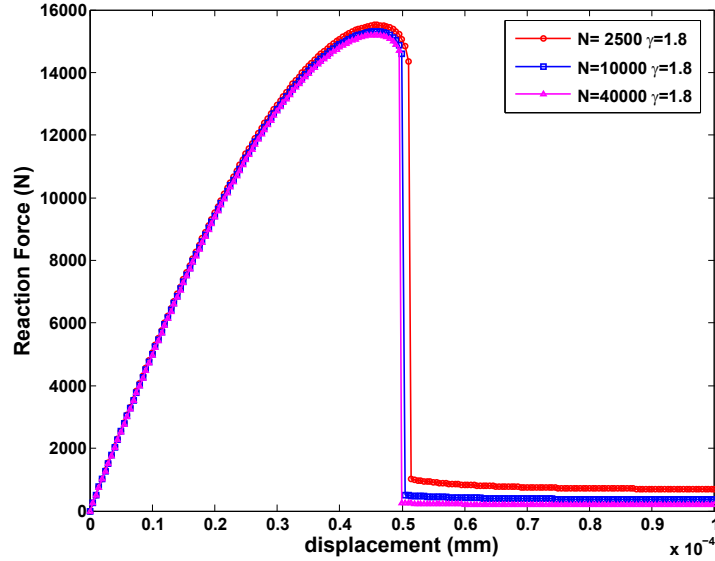


Figure 5.12: Load-deflection curves for $h = 0.0204, 0.0101, 0.005$, $G_c = 1.0$ N/mm, $\ell = 0.05$ mm and $\gamma = 1.8$.

5.4.2 Connected pipes pulling

In this example we show the flexibility and robustness of the present methodology to deal with a thin shell of complex topology and complex crack path. Figure 5.13 shows the surface, consisting of a set of six connected open pipes. The boundary curve at the bottom is clamped, whereas the top boundary curve is incrementally displaced in the upward $(0, 0, 1)$ direction. Material parameters have been selected as $E = 10^7$ N/mm² and $\nu = 0.3$, $G_c = 1$ N/mm, while the thickness is $t = 0.005$ mm. The discretization of the geometry (geometric markers) and the control points consists of two arrangements of 25668 and 100380 unstructured set of points respectively. The original coarse point-set has been obtained from the MATLAB central file exchange and subsequently subdivide it through Loop's subdivision algorithm by using Paraview [144]. The phase field is represented as a colormap on the reference configuration, see Figs. 5.14A,C. Figures 5.14B,D shows the physical deformation obtained, which has been amplified by a factor of 20 to give a better idea of the resulting displacements. Due to the nonlinearity of the model, we observe a symmetry-breaking solution.

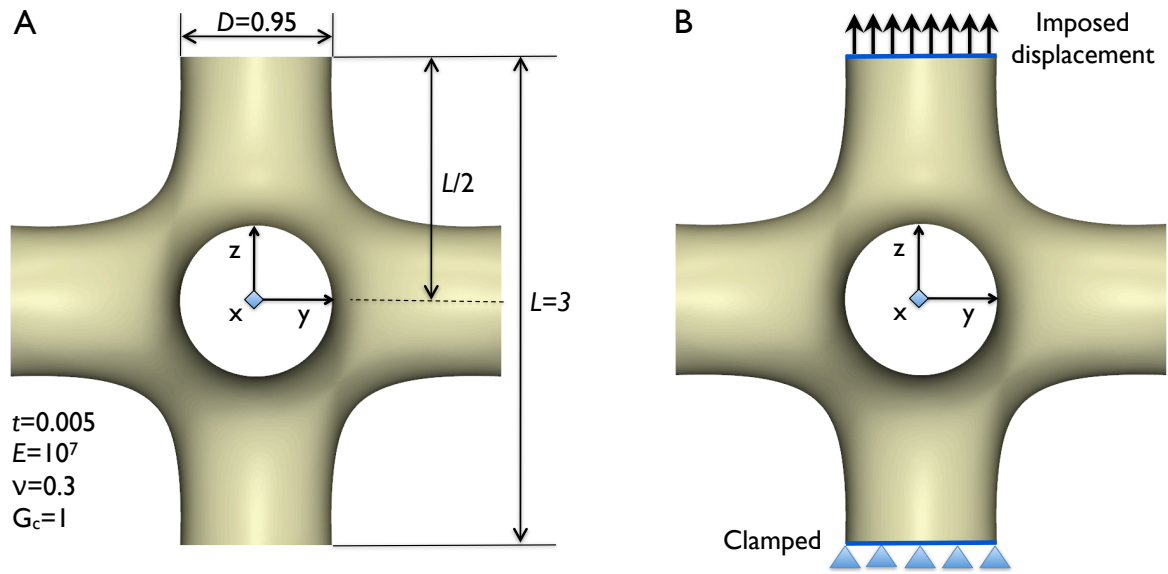


Figure 5.13: Sketch for the brittle thin shell problem. (A) Material and geometrical parameters describing a set of six connected open pipes. (B) The prescribed boundary conditions and the applied incremental displacement.

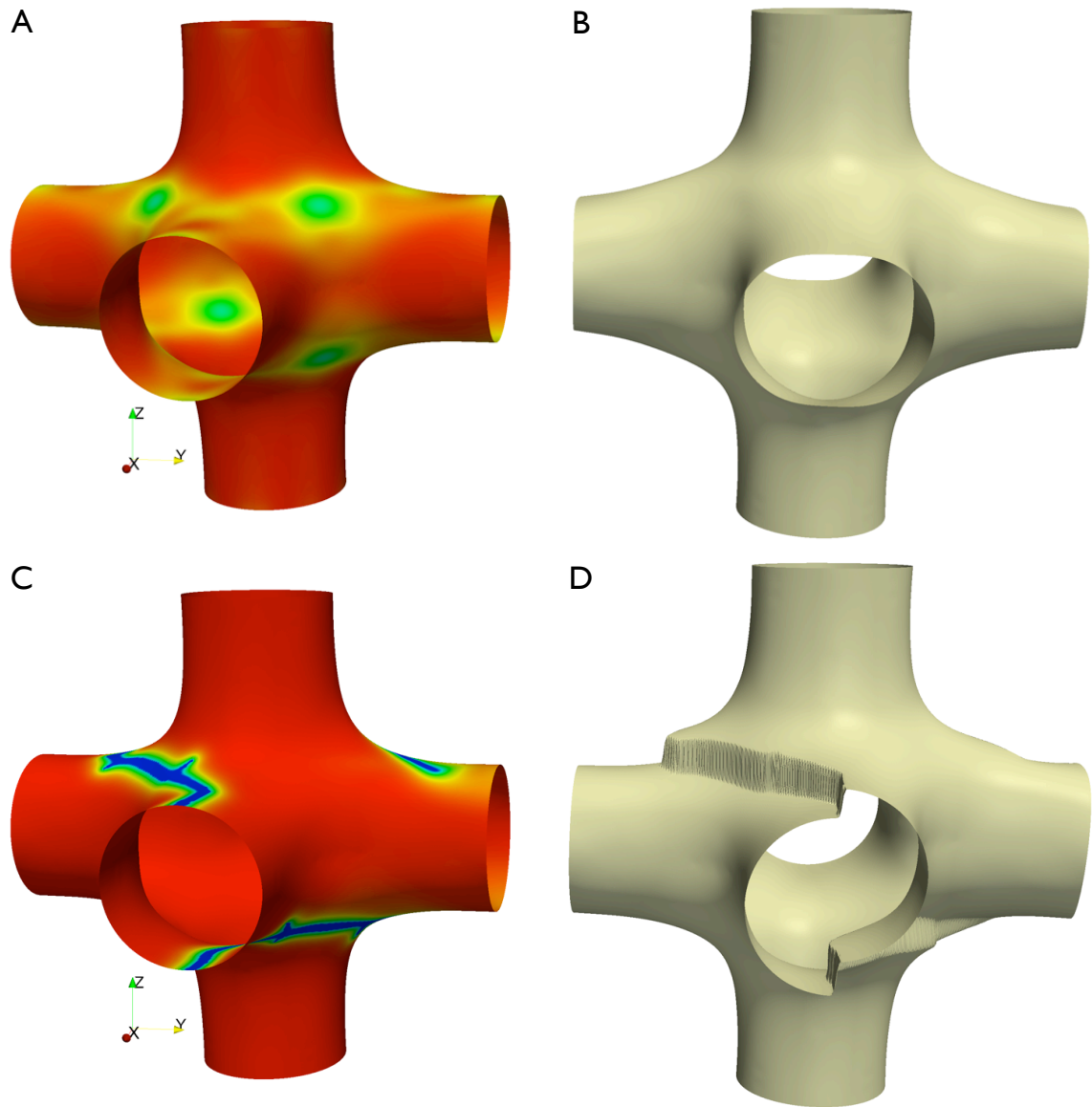


Figure 5.14: Selected snapshots of the deformation process of a brittle thin shell with complex topology. The boundary curve of the bottom pipe is clamped and the top boundary curve is incrementally displaced in the upward $(0, 0, 1)$ direction. The process has been performed without an initial crack. (A,C) Phase field as colormap in the reference configuration for two selected imposed displacements of the top boundary curve, just before the fracture ($d = 0.0055$) and for the final imposed displacement, $d = 0.01$. (B,D) Deformed configurations for two selected instants, the deformation field has been magnified by 20.

Chapter 6

Conclusions and future work

6.1 Contributions

We summarize here the most significant contributions of this work:

1. In the first part of this dissertation, we have developed a local maximum entropy approximation scheme for fracture using enrichment functions. The LME shape functions are non-negative which improves stability, and they possess a weak Kronecker delta property which makes it easy to impose the boundary conditions. With a fixed area (geometric) enrichment, optimal convergence is obtained. The LME basis functions are in general not polynomials but rather particle-based smooth functions, whose support is dictated by a non-dimensional parameter γ . When γ decreases, the LME shape functions have better approximation properties compared to standard FEM shape functions, but the size of their support increases. Hence, accurate numerical integration using standard Gauss quadrature requires a greater number of function evaluations. We conclude that there is an optimal value of γ of around 1.8 that maximizes the accuracy in relation to computational cost.
2. For computation of stress intensity factors, XLME method is competitive in terms of costs compared to XFEM. Very likely, it is possible to improve the computational efficiency further.
3. In the second part, we introduced phase field method to use in conjunction with smooth approximants as LME. We observed that phase field method reduces the algorithmic complexity of the implementation, especially in three dimensional problems. In contrast to discrete methods which require to numerically track

the discontinuities in the displacement field, the phase field methods provide a continuous representation of a crack surface. We also observed that extending 2D problems to 3D is straightforward for the phase field method.

4. We have developed the fourth order phase field method, the aim is to increase the rate of convergence, and improve the accuracy and efficiency.
5. We compared the second and the fourth order phase field models for LME method. The fourth order phase field model gives more accurate results with lower γ and sharper crack simulation. This model lets us use smoother shape functions with finer length scale parameter. As explained in this dissertation, the smoothness of LME shape functions depends on parameter γ . When the parameter γ decreases, the LME shape functions differ from standard FEM shape functions and the locality decreases. Hence, these shape functions approximate smooth functions. We have also shown that both the second and fourth order phase field models are capable of capturing complex crack behavior in three dimensions.
6. We observed that the length scale parameter of the phase field model, is problem dependent. However choosing $4h \leq l_0$ gives almost reliable results.
7. We conclude that there is an optimal value of $\gamma \leq 1.8$ for the fourth order phase field model and $\gamma \geq 4.8$ for the the second order phase field model in use with the meshfree LME approximation, that maximizes the accuracy.
8. The advantage of phase field models over the XLME that we don't need to track the crack path and compute stress intensity factors to predict the crack path. So, the computer's code is much easier than XLME. However, XLME method gives more accurate results.
9. The higher order continuity of the meshfree LME approximation allows to directly solve the fourth-order phase field equations without splitting the fourth-order differential equation into two second order differential equations.
10. In contrast to the at least quadratic NURBS-formulation [110], we employ only linear basis. In FEM, Hughes [111] have shown for the fourth order PDEs, at least a quadratic basis is required. However, a linear LME basis was sufficient to obtain excellent results for Kirchhoff-Love thin shells (also fourth order PDE).

11. We have extended the methodology proposed in [3] to model fracture in Kirchhoff-Love thin shell bodies described by surface of complex geometry and topology. We propose here treating fracture with a phase-field model and discretizing the coupled thin-shell/phase-field equations. We developed this method for brittle material and analyzed this model for a structure with complex geometry and topology. Simulations have shown that the onset of crack propagation in the phase-field model can be linked to the energy release rate reaching the critical value G_c .

6.2 Open lines for research

We next mention some open ideas for research derived from the work performed:

1. In XLME method, we plan to investigate the development of an efficient integration scheme, goal-oriented adaptivity for the parameter γ and the enrichment radius, as well as methods to improve the condition number of the stiffness matrix.
2. The proposed XLME approximation also shows a lot of potential for other problems which will be examined in the future, such as crack growth and fracture in thin shell bodies.
3. A Γ -convergence proof for the fourth order model has not yet been established, see Appendix B.
4. Since the LME shape functions are "approximants" not "interpolants", the irreversibility conditions for the phase field model need to be improve.
5. To model fracture in Kirchhoff-Love thin shell bodies, we have used the second order phase field model with $\gamma \geq 4.8$ to approximate the crack surface. It is noteworthy in this work that we have used different values of the LME aspect parameter γ , for both phase-field and thin shell model. Since, the numerical solutions calculated for linear and nonlinear thin shell problems involving high order derivatives have shown to be very accurate when the locality parameter is selected within the range $0.6 \leq \gamma \leq 1$ (Millan et al., 2011, 2012) [3, 79]. We observe that using similar parameter γ , for the second order phase-field and thin shell model (equal $0.6 \leq \gamma \leq 1$) leads to less accurate results for phase-field. Additionally, different parameters γ make impossible to obtain right results for

mode II, due to connection between shape functions on both sides of crack. The future work is to use equal values of the smoothness LME parameter γ for both problems by introducing the fourth order phase-field model to use in Kirchhoff-Love thin shell structures.

6. A comparison such as the computation cost, the complexity of the algorithms and the accuracy should be done between XLME approximants and phase field method to model fracture in Kirchhoff- Love thin shell bodies with complex geometry and topology.
7. In this work, we assumed that the phase field parameter is uniform through the thickness for the coupled thin-shell/phase-field equations. The future work is to consider nonuniform phase field parameter through the thickness.
8. In the phase field model, the energy is released due to fracture in both tension and compression. This limits the application of the presented model to special problems. In the future, we will separate the positive and the negative part of the stored energy based on the spectral decomposition of the strain tensor [105]. We also plan to apply this feature to thin shell structures with fracture.

Appendix A

Derivatives of the LME shape functions

Here, we calculate the derivatives of the local maximum entropy approximants. We denote spatial gradients of scalar functions by ∇ , whereas for vector-valued functions we denote the matrix of partial derivatives by $D\mathbf{y}(\mathbf{x})$. The symbol ∂ denotes partial differentiation. We suppose the parameter β is constant, as have been used in this work. Consider the following functions

$$f_a(\mathbf{x}, \boldsymbol{\lambda}) = -\beta_a |\mathbf{x} - \mathbf{x}_a|^2 + \boldsymbol{\lambda} \cdot (\mathbf{x} - \mathbf{x}_a) \quad (\text{A.1})$$

$$\mathbf{Z}(\mathbf{x}, \boldsymbol{\lambda}) = \sum_{i=1}^N \exp[f_i(\mathbf{x}, \boldsymbol{\lambda})] \quad (\text{A.2})$$

$$p_a(\mathbf{x}, \boldsymbol{\lambda}) = \frac{\exp[f_a(\mathbf{x}, \boldsymbol{\lambda})]}{\mathbf{Z}(\mathbf{x}, \boldsymbol{\lambda})} \quad (\text{A.3})$$

$$\mathbf{r}(\mathbf{x}, \boldsymbol{\lambda}) = \partial_{\boldsymbol{\lambda}} \log \mathbf{Z}(\mathbf{x}, \boldsymbol{\lambda}) \quad (\text{A.4})$$

$$\mathbf{r}(\mathbf{x}, \boldsymbol{\lambda}) = \frac{\sum_{i=1}^N \exp[f_i(\mathbf{x}, \boldsymbol{\lambda})](\mathbf{x} - \mathbf{x}_i)}{\sum_{i=1}^N \exp[f_i(\mathbf{x}, \boldsymbol{\lambda})]} = \sum_{i=1}^N p_i(\mathbf{x}, \boldsymbol{\lambda})(\mathbf{x} - \mathbf{x}_i) \quad (\text{A.5})$$

$$\mathbf{J}(\mathbf{x}, \boldsymbol{\lambda}) = \partial_{\boldsymbol{\lambda}} \partial_{\boldsymbol{\lambda}} \log \mathbf{Z}(\mathbf{x}, \boldsymbol{\lambda}) \quad (\text{A.6})$$

Calculating the derivative of (A.4) respect to $\boldsymbol{\lambda}$ and arrange the terms gives

$$\mathbf{J}(\mathbf{x}, \boldsymbol{\lambda}) = \sum_{i=1}^N p_i(\mathbf{x}, \boldsymbol{\lambda})(\mathbf{x} - \mathbf{x}_i) \otimes (\mathbf{x} - \mathbf{x}_i) - \mathbf{r}(\mathbf{x}, \boldsymbol{\lambda}) \otimes \mathbf{r}(\mathbf{x}, \boldsymbol{\lambda}) \quad (\text{A.7})$$

For simplicity we consider a fix vector-valued function of $\boldsymbol{\lambda}$. We show this function by $\boldsymbol{\lambda}^*$ and the associated functions for this valued function by $(\cdot)^*$, for example p_a^*, f_a^* . In fact $\boldsymbol{\lambda}^*$ is the unique maximizer of $-\log \mathbf{Z}(\mathbf{x}, \boldsymbol{\lambda})$. Our aim is to compute ∇p_a^* . Applying ∇ on equation (A.3) and considering equations (A.2) and (A.3) and simple calculations give

$$\nabla p_a^* = p_a^* \nabla f_a^* - p_a^* \sum_{i=1}^N p_i^* \nabla f_i^* \quad (\text{A.8})$$

By the chain rule, we have

$$\nabla f_a^* = -2\beta_a(\mathbf{x} - \mathbf{x}_a) + \boldsymbol{\lambda}^* + (\mathbf{x} - \mathbf{x}_a) D\boldsymbol{\lambda}^* \quad (\text{A.9})$$

The only term that is not available explicitly is $D\boldsymbol{\lambda}^*$. Since $\mathbf{r}^* = 0$, we have

$$0 = D\mathbf{r}^* = \left(\frac{\partial \mathbf{r}}{\partial \mathbf{x}}\right)^* + D\boldsymbol{\lambda}^* \left(\frac{\partial \mathbf{r}}{\partial \boldsymbol{\lambda}}\right)^* \quad (\text{A.10})$$

from (A.6)

$$\left(\frac{\partial \mathbf{r}}{\partial \boldsymbol{\lambda}}\right)^* = \mathbf{J}^*$$

and from (A.4) and (A.3) we have

$$\left(\frac{\partial \mathbf{r}}{\partial \mathbf{x}}\right)^* = -\mathbf{J}_\beta + \mathbf{I}$$

$$\mathbf{J}_\beta = 2\sum_{i=1}^N p_i^*(\mathbf{x}, \boldsymbol{\lambda})(\mathbf{x} - \mathbf{x}_i) \otimes (\mathbf{x} - \mathbf{x}_i)$$

$$D\boldsymbol{\lambda}^* = (\mathbf{J}_\beta - \mathbf{I})(\mathbf{J}^*)^{-1}$$

We finally get the first spatial derivative of the shape functions as

$$\nabla p_a^* = p_a^*[\mathbf{r}_\beta - \mathbf{M}_a(\mathbf{x} - \mathbf{x}_a)] \quad (\text{A.11})$$

$$\mathbf{r}_\beta = 2\sum_i \beta_i p_i^*(\mathbf{x} - \mathbf{x}_i), \quad \mathbf{M}_a = (2\beta_a \mathbf{I} - D\boldsymbol{\lambda}^*)$$

The second spatial derivative of the shape functions or Hessian, is denoted by $(H_{p_a})^*$ and computed as follow. By applying ∇ on equation (A.8), we have

$$\begin{aligned} (H_{p_a})^* &= \nabla p_a^* \otimes (\nabla f_a^* - \sum_i p_i^* \nabla f_i^*) + p_a^* ((D\nabla f_a)^* \\ &\quad - \sum_i p_i^* (D\nabla f_i)^*) - p_a^* \sum_i \nabla p_i^* \otimes \nabla f_i^* \end{aligned} \quad (\text{A.12})$$

$$\begin{aligned}
(H_{p_a})^* &= p_a^*[\mathbf{r}_\beta - \mathbf{M}_a(\mathbf{x} - \mathbf{x}_a)] \otimes [\mathbf{r}_\beta - \mathbf{M}_a(\mathbf{x} - \mathbf{x}_a)] \\
&\quad + 2p_a^*(\sum_i \beta_i p_i^* - \beta_i) \mathbf{I} + p_a^* D^2 \boldsymbol{\lambda}^*(\mathbf{x} - \mathbf{x}_a) \\
&\quad - p_a^* \mathbf{r}_\beta \otimes \mathbf{r}_\beta + p_a^* \sum_i p_i^* \mathbf{M}_i(\mathbf{x} - \mathbf{x}_i) \otimes \mathbf{M}_i(\mathbf{x} - \mathbf{x}_i)
\end{aligned} \tag{A.13}$$

Using the fact that $D^2 \mathbf{r} = 0$, we obtain

$$\begin{aligned}
D^2 \boldsymbol{\lambda}^*(\mathbf{x} - \mathbf{x}_a) &= \mathbf{r}_\beta \otimes \mathbf{j}_a + \mathbf{j}_a \otimes \mathbf{r}_\beta + (\mathbf{r}_\beta \cdot \mathbf{j}_a) \mathbf{I} \\
&\quad - \sum_i p_i^* \Delta_{ai} \mathbf{M}_i(\mathbf{x} - \mathbf{x}_i) \otimes \mathbf{M}_i(\mathbf{x} - \mathbf{x}_i)
\end{aligned} \tag{A.14}$$

$$\Delta_{ai} = (\mathbf{x} - \mathbf{x}_i) \cdot (\mathbf{J}^*)^{-1}(\mathbf{x} - \mathbf{x}_a), \quad \mathbf{j}_a = (\mathbf{J}^*)^{-1}(\mathbf{x} - \mathbf{x}_a)$$

After replacing and arranging the terms we have

$$\begin{aligned}
(H_{p_a})^* &= p_a^*[\mathbf{r}_\beta - \mathbf{M}_a(\mathbf{x} - \mathbf{x}_a)] \otimes [\mathbf{r}_\beta - \mathbf{M}_a(\mathbf{x} - \mathbf{x}_a)] \\
&\quad + 2p_a^*(\sum_i \beta_i p_i^* - \beta_i) \mathbf{I} \\
&\quad + p_a^*[\mathbf{r}_\beta \otimes \mathbf{r}_\beta + \mathbf{r}_\beta \otimes \mathbf{j}_a + \mathbf{j}_a \otimes \mathbf{r}_\beta + (\mathbf{r}_\beta \cdot \mathbf{j}_a) \mathbf{I}] \\
&\quad - p_a^* \sum_i p_i^* (1 + \Delta_{ai}) \mathbf{M}_i(\mathbf{x} - \mathbf{x}_i) \otimes \mathbf{M}_i(\mathbf{x} - \mathbf{x}_i)
\end{aligned} \tag{A.15}$$

Appendix B

The Γ -convergence approximation conjecture of De Giorgi model

Definition 1. (Γ -convergence). Let X be a topological space, we say that a sequence functional $f_{j_0} : X \rightarrow R^+$, $j_0 > 0$, Γ -converges in X to $f : X \rightarrow R^+$ if for all $x \in X$ we have

(i) (lim inf inequality) for every sequence $(x_{j_0}) \in X$ converging to $x \in X$ as $j_0 \rightarrow 0$

$$f \leq \liminf_{j_0 \rightarrow 0} f_{j_0}(x_{j_0}); \quad (\text{B.1})$$

(ii) (lim sup inequality) there exists a sequence $(x_{j_0}) \in X$ converging to $x \in X$ such that

$$f \geq \limsup_{j_0 \rightarrow 0} f_{j_0}(x_{j_0}); \quad (\text{B.2})$$

The function f is called the Γ -limit of (f_{j_0}) , and we write $f = \Gamma - \lim_{j_0 \rightarrow 0} f_{j_0}$.

Theorem 4. If f_{j_0} Γ -converges to f and x_{j_0} minimizes f_{j_0} over X , then every cluster point of (x_{j_0}) minimizes f over X .

Γ -convergence of the second order phase field model for the brittle fracture in linear elasticity, has been proved in [52, 145, 146]. This implies that the minimizing solution to Γ_{l_0} will converge to a minimizing solution of Γ as l_0 goes to zero. In fact, the minimizing solution of Γ as l_0 converge to zero is the total potential energy for Griffith's theory.

It was proved in [147, 148], the high order correction of the Mumford–Shah image

model – the Mumford–Shah–Euler image functional

$$F_l = \frac{\alpha}{c_1} \int_{\Omega} [l |\nabla v|^2 + \frac{w(v)}{l}] dV + \frac{\beta}{c_2} \int_{\Omega} [2\Delta v - \frac{w(v)'}{l^2}]^2 dV, \quad (\text{B.3})$$

Γ -converge to

$$\Gamma(\Omega) = \int_{\Omega} (\alpha + \beta \kappa^2) dV, \quad (\text{B.4})$$

as $l \rightarrow 0$. Here α and β are positive weights, c_1, c_2 are positive constants, $w(v)$ is the double-well potential function and κ is the contour curvature.

Appendix C

The Green–Lagrange strain tensor for Kirchhoff–Love assumptions

Consider

$$E_{ij} = \frac{1}{2}(g_{ij} - g_{0ij}) = \frac{1}{2}(\Phi_{,i} \cdot \Phi_{,j} - \Phi_{0,i} \cdot \Phi_{0,j}). \quad (\text{C.1})$$

By substituting $\Phi = \varphi(\xi^1, \xi^2) + \xi \mathbf{t}(\xi^1, \xi^2)$ into above equation we have

$$E_{\alpha\beta} = \varepsilon_{\alpha\beta} + \xi \rho_{\alpha\beta} + (\xi)^2 \vartheta_{\alpha\beta} \quad (\text{C.2})$$

Where

$$\varepsilon_{\alpha\beta} = \frac{1}{2}(\varphi_{,\alpha} \cdot \varphi_{,\beta} - \varphi_{0,\alpha} \cdot \varphi_{0,\beta}) \quad (\text{C.3})$$

$$\rho_{\alpha\beta} = \varphi_{,\alpha} \cdot \mathbf{t}_{,\beta} - \varphi_{0,\alpha} \cdot \mathbf{t}_{0,\beta} \quad (\text{C.4})$$

$$\vartheta_{\alpha\beta} = \frac{1}{2}(\mathbf{t}_{,\alpha} \cdot \mathbf{t}_{,\beta} - \mathbf{t}_{0,\alpha} \cdot \mathbf{t}_{0,\beta}) \quad (\text{C.5})$$

for $\alpha, \beta = 1, 2$.

$$E_{\alpha 3} = \frac{1}{2}\{\varphi_{,\alpha} \cdot \mathbf{t} + \mathbf{t}_{,\alpha} \cdot \mathbf{t} - \varphi_{0,\alpha} \cdot \mathbf{t}_0 - \mathbf{t}_{0,\alpha} \cdot \mathbf{t}_0\}$$

$$E_{33} = \frac{1}{2}\{\mathbf{t} \cdot \mathbf{t} - \mathbf{t}_0 \cdot \mathbf{t}_0\}$$

considering the condition (5.6), we get

$$E_{\alpha 3} = \frac{1}{2}\{\varphi_{,\alpha} \cdot \mathbf{t} + \mathbf{t}_{,\alpha} \cdot \mathbf{t}\}$$

$$E_{33} = \frac{1}{2}\{\mathbf{t} \cdot \mathbf{t} - 1\}$$

So, $\varepsilon_{\alpha 3} = \frac{1}{2} \boldsymbol{\varphi}_{,\alpha} \cdot \mathbf{t}$ and $\varepsilon_{33} = \frac{1}{2} (\mathbf{t} \cdot \mathbf{t} - 1)$ and $\rho_{\alpha 3} = \frac{1}{2} \mathbf{t}_{,\alpha} \cdot \mathbf{t}$.

- $\varepsilon_{\alpha\beta}$ is the membrane strain tensor, which measures the in-plane deformation of the surface. The components $\varepsilon_{\alpha 3}$ measure the shearing of the director \mathbf{t}_0 and the component ε_{33} measures the stretching of the director \mathbf{t}_0 .

- The tensor $\rho_{\alpha\beta}$ measure the bending or change in curvature of the shell. $\rho_{\alpha 3}$ measures the shearing originated from the director elongation.

- The in-plane tensor $\vartheta_{\alpha\beta}$ is exclusively related to changes of the middle surface directors.

Considering the Kirchhoff–Love theory of thin shells, we have

$$\mathbf{t} = \frac{\boldsymbol{\varphi}_{,1} \times \boldsymbol{\varphi}_{,2}}{\bar{j}}, \quad \boldsymbol{\varphi}_{,\alpha} \cdot \mathbf{t} = 0, \quad |\mathbf{t}| = 1, \quad \mathbf{t} \cdot \mathbf{t}_{,\alpha} = 0.$$

Hence, we have

$$\varepsilon_{\alpha 3} = \varepsilon_{33} = \rho_{\alpha 3} = 0$$

So, the only nonzero components of strain tensor are on the mid–surface of shell.

C.1 Equilibrium configuration of thin shells

The potential energy of an elastic shell body with internal energy density W can be expressed by the functional

$$\Pi[\mathbf{u}] = \int_{\mathcal{S}_0} W(\mathbf{u}) dV_0 + \Pi_{\text{ext}}[\mathbf{u}],$$

where Π_{ext} is the potential energy of the external loads. We consider an isotropic Kirchhoff–St. Venant elastic material, with an internal energy density expressed as [149]

$$W = \frac{1}{2} C^{ijkl} E_{ij} E_{kl},$$

where C^{ijkl} are the contravariant components of the elasticity tensor. For thin shell bodies, the Green-Lagrange tensor components are commonly retained up to first order in t , see Equation (5.7), and the effect of curvature on the configuration Jacobian away from the middle surface is neglected, that is $j_0/\bar{j}_0 = 1$ (see [117, 139]). Assuming that the elasticity tensor does not vary through the thickness, the internal energy density can be integrated through-the-thickness as follows:

$$\Pi[\mathbf{u}] = \int_{\Omega_0} \int_{-t/2}^{t/2} W(\mathbf{u}) \frac{j_0}{\bar{j}_0} d\xi d\Omega_0 + \Pi_{\text{ext}}[\mathbf{u}],$$

resulting in an internal energy density per unit area

$$\mathcal{W} = \frac{1}{2} \int_{-t/2}^{t/2} C^{\alpha\beta\gamma\delta} E_{\alpha\beta} E_{\gamma\delta} \frac{j_0}{j_0} d\xi \quad (\text{C.6})$$

with

$$C^{\alpha\beta\gamma\delta} = \frac{E}{(1-\nu^2)} \left[\nu a_0^{\alpha\beta} a_0^{\gamma\delta} + \frac{1}{2}(1-\nu) (a_0^{\alpha\gamma} a_0^{\beta\delta} + a_0^{\alpha\delta} a_0^{\beta\gamma}) \right],$$

where $a_0^{\alpha\gamma} (a_0)_{\gamma\beta} = \delta_{\beta}^{\alpha}$, E is the Young's modulus, and ν the Poisson's ratio.

By substituting Equation (C.2) into the Equation (C.6) and consistent with the thin shell assumption, and neglecting higher order terms of t , we have

$$\mathcal{W} \simeq \frac{1}{2} C^{\alpha\beta\gamma\delta} \left(t \varepsilon_{\alpha\beta} \varepsilon_{\gamma\delta} + \frac{t^3}{12} \rho_{\alpha\beta} \rho_{\gamma\delta} \right).$$

Thus, the internal potential energy can be written as an integral over the reference middle surface

$$\Pi_{\text{int}}[\mathbf{u}] = \int_{\Omega_0} \mathcal{W}(\mathbf{u}) d\Omega_0.$$

C.2 Small displacements

We assume that the deformation field for the shell is restricted to small deformation theory or small displacement theory. Then, if the displacement vector of the middle surface of the shell is defined as $\boldsymbol{\varphi} = \mathbf{u} + \boldsymbol{\varphi}_0$, the linear membrane components of the middle surface of the shell can be written up to first order in \mathbf{u} in the form

$$\varepsilon_{\alpha\beta} = \frac{1}{2} (\boldsymbol{\varphi}_{0,\alpha} \cdot \mathbf{u}_{,\beta} + \boldsymbol{\varphi}_{0,\beta} \cdot \mathbf{u}_{,\alpha} + \mathbf{u}_{,\alpha} \cdot \mathbf{u}_{,\beta}),$$

By considering that $\mathbf{u}_{,\alpha} \cdot \mathbf{u}_{,\beta} = 0$, then we have

$$\varepsilon_{\alpha\beta} = \frac{1}{2} (\boldsymbol{\varphi}_{0,\alpha} \cdot \mathbf{u}_{,\beta} + \boldsymbol{\varphi}_{0,\beta} \cdot \mathbf{u}_{,\alpha}).$$

From Section 5.3, with the Kirchhoff–Love assumptions and defining the displacement vector $\boldsymbol{\varphi} = \mathbf{u} + \boldsymbol{\varphi}_0$, the linear bending strain tensor components in Equation (C.4) can be written as

$$\rho_{\alpha\beta} = \boldsymbol{\varphi}_{0,\alpha\beta} \cdot \mathbf{t}_0 - (\boldsymbol{\varphi}_{0,\alpha\beta} + \mathbf{u}_{,\alpha\beta}) \cdot \mathbf{t}, \quad (\text{C.7})$$

where

$$\mathbf{t} = \frac{\boldsymbol{\varphi}_{,1} \times \boldsymbol{\varphi}_{,2}}{\bar{j}} = \frac{(\mathbf{u}_{,1} + \boldsymbol{\varphi}_{0,1}) \times (\mathbf{u}_{,2} + \boldsymbol{\varphi}_{0,2})}{\bar{j}},$$

$$\mathbf{t} = \bar{j}^{-1} (\boldsymbol{\varphi}_{0,1} \times \boldsymbol{\varphi}_{0,2} + \mathbf{u}_{,1} \times \boldsymbol{\varphi}_{0,2} + \boldsymbol{\varphi}_{0,1} \times \mathbf{u}_{,2} + \mathbf{u}_{,1} \times \mathbf{u}_{,2}).$$

Considering up to first order in \mathbf{u} , \bar{j}^{-1} in the reference configuration is written in the form

$$\bar{j}^{-1} \approx \bar{j}_0^{-1} - \bar{j}_0^{-2} \mathbf{t}_0 \cdot (\mathbf{u}_{,1} \times \boldsymbol{\varphi}_{0,2} + \boldsymbol{\varphi}_{0,1} \times \mathbf{u}_{,2}),$$

which allows us to calculate the normal director increment $\Delta \mathbf{t} = \mathbf{t} - \mathbf{t}_0$ as

$$\Delta \mathbf{t} \approx \bar{j}_0^{-1} (\mathbf{u}_{,1} \times \boldsymbol{\varphi}_{0,2} + \boldsymbol{\varphi}_{0,1} \times \mathbf{u}_{,2}) - \bar{j}_0^{-1} [\mathbf{t}_0 \cdot (\mathbf{u}_{,1} \times \boldsymbol{\varphi}_{0,2} + \boldsymbol{\varphi}_{0,1} \times \mathbf{u}_{,2})] \mathbf{t}_0.$$

Considering equations: $\mathbf{v} = \mathbf{u}_{,1} \times \boldsymbol{\varphi}_{0,2} + \boldsymbol{\varphi}_{0,1} \times \mathbf{u}_{,2}$ and $\mathbf{a} \times (\mathbf{b} \times \mathbf{c}) = \mathbf{b}(\mathbf{a} \cdot \mathbf{c}) - \mathbf{c}(\mathbf{a} \cdot \mathbf{b})$ the normal director increment takes a form

$$\Delta \mathbf{t} = \bar{j}_0^{-1} [\mathbf{v}(\mathbf{t}_0 \cdot \mathbf{t}_0) - (\mathbf{t}_0 \cdot \mathbf{v})\mathbf{t}_0] = \bar{j}_0^{-1} [\mathbf{t}_0 \times (\mathbf{v} \times \mathbf{t}_0)].$$

Replacing \mathbf{t} by $\mathbf{t}_0 + \Delta \mathbf{t}$ in Equation (C.7), rearranging terms, applying the identities $\mathbf{a} \cdot (\mathbf{b} \times \mathbf{c}) = \mathbf{c} \cdot (\mathbf{a} \times \mathbf{b}) = \mathbf{b} \cdot (\mathbf{c} \times \mathbf{a})$ and $\mathbf{a} \times \mathbf{b} = -\mathbf{b} \times \mathbf{a}$, and omitting higher-order terms in \mathbf{u} , the bending strains can be expressed as

$$\rho_{\alpha\beta} = -\mathbf{t}_0 \cdot \mathbf{u}_{,\alpha\beta} + \bar{j}_0^{-1} \left[(\boldsymbol{\varphi}_{0,\alpha\beta} \times \boldsymbol{\varphi}_{0,2}) \cdot \mathbf{u}_{,1} + (\boldsymbol{\varphi}_{0,1} \times \boldsymbol{\varphi}_{0,\alpha\beta}) \cdot \mathbf{u}_{,2} \right] + \bar{j}_0^{-1} (\mathbf{t}_0 \cdot \boldsymbol{\varphi}_{0,\alpha\beta}) \left[(\boldsymbol{\varphi}_{0,2} \times \mathbf{t}_0) \cdot \mathbf{u}_{,1} + (\mathbf{t}_0 \times \boldsymbol{\varphi}_{0,1}) \cdot \mathbf{u}_{,2} \right]. \quad (\text{C.8})$$

Bibliography

- [1] J. Gálvez, M. Elices, G. Guinea, and J. Planas, “Mixed mode fracture of concrete under proportional and nonproportional loading,” *International Journal of Fracture*, vol. 94, no. 3, pp. 267–284, 1998.
- [2] P. M. A. Areias and T. Belytschko, “Analysis of three-dimensional crack initiation and propagation using the extended finite element method,” *International Journal for Numerical Methods in Engineering*, vol. 63, no. 5, pp. 760–788, 2005.
- [3] D. Millán, A. Rosolen, and M. Arroyo, “Nonlinear manifold learning for mesh-free finite deformations thin shell analysis,” *International Journal for Numerical Methods in Engineering*, vol. 93, no. 7, pp. 685–713, 2013.
- [4] R. Reed, U. S. N. B. of Standards, and B. M. I. C. Laboratories, *The Economic Effects of Fracture in the United States*. No. pt. 1 in NBS special publication, U.S. Department of Commerce, National Bureau of Standards, 1983.
- [5] A. A. Griffith, “The phenomena of rupture and flow in solids,” *Philosophical Transactions of the Royal Society of London. Series A, Containing Papers of a Mathematical or Physical Character*, vol. 221, no. 582-593, pp. 163–198, 1921.
- [6] G. Irwin, “Elasticity and plasticity: fracture,” *In Encyclopedia of Physics, Flügge S (ed.), Springer: Berlin*, vol. 6, pp. 551–590, 1958.
- [7] K. Chaoui, R. Khelif, N. Zeghib, and A. Chateauneuf, “Failure analysis of polyethylene gas pipes,” in *Safety, Reliability and Risks Associated with Water, Oil and Gas Pipelines* (G. Pluvinage and M. Elwany, eds.), NATO Science for Peace and Security Series, pp. 131–163, Springer Netherlands, 2008.
- [8] D. Winne and B. Wundt, “application of the griffith-irwin theory of crack propagation to the bursting behavior of disks, including analytical and experimental studies,” *Transactions of the American Society of Mechanical Engineers*, vol. 80, pp. 1643–1655, 1958.

-
- [9] P. Areias, T. Rabczuk, and D. D. da Costa, “Element-wise fracture algorithm based on rotation of edges,” *Engineering Fracture Mechanics*, vol. 110, pp. 113 – 137, 2013.
- [10] P. Areias and T. Rabczuk, “Finite strain fracture of plates and shells with configurational forces and edge rotations,” *International Journal for Numerical Methods in Engineering*, vol. 94, no. 12, pp. 1099–1122, 2013.
- [11] P. Areias, T. Rabczuk, and P. Camanho, “Finite strain fracture of 2d problems with injected anisotropic softening elements,” *Theoretical and Applied Fracture Mechanics*, vol. 72, pp. 50 – 63, 2014. Multiscale Modeling of Material Failure.
- [12] H. Nguyen-Xuan, G. Liu, S. Bordas, S. Natarajan, and T. Rabczuk, “An adaptive singular es-fem for mechanics problems with singular field of arbitrary order,” *Computer Methods in Applied Mechanics and Engineering*, vol. 253, pp. 252 – 273, 2013.
- [13] T. Belytschko and T. Black, “Elastic crack growth in finite elements with minimal remeshing,” *International Journal for Numerical Methods in Engineering*, vol. 45, no. 5, pp. 601–620, 1999.
- [14] N. Moës, J. Dolbow, and T. Belytschko, “A finite element method for crack growth without remeshing,” *International Journal for Numerical Methods in Engineering*, vol. 46, no. 1, pp. 131–150, 1999.
- [15] T. Strouboulis, I. Babuška, and K. Copps, “The design and analysis of the generalized finite element method,” *Computer Methods in Applied Mechanics and Engineering*, vol. 181, no. 1–3, pp. 43 – 69, 2000.
- [16] I. Babuška and J. M. Melenk, “The partition of unity method,” *International Journal for Numerical Methods in Engineering*, vol. 40, no. 4, pp. 727–758, 1997.
- [17] J. Chessa and T. Belytschko, “An enriched finite element method and level sets for axisymmetric two-phase flow with surface tension,” *International Journal for Numerical Methods in Engineering*, vol. 58, no. 13, pp. 2041–2064, 2003.
- [18] D. Chopp and N. Sukumar, “Fatigue crack propagation of multiple coplanar cracks with the coupled extended finite element/fast marching method,” *International Journal of Engineering Science*, vol. 41, no. 8, pp. 845 – 869, 2003.

-
- [19] R. Duddu, S. Bordas, D. Chopp, and B. Moran, “A combined extended finite element and level set method for biofilm growth,” *International Journal for Numerical Methods in Engineering*, vol. 74, no. 5, pp. 848–870, 2008.
- [20] H. Ji, D. Chopp, and J. E. Dolbow, “A hybrid extended finite element/level set method for modeling phase transformations,” *International Journal for Numerical Methods in Engineering*, vol. 54, no. 8, pp. 1209–1233, 2002.
- [21] R. Merle and J. Dolbow, “Solving thermal and phase change problems with the extended finite element method,” *Computational Mechanics*, vol. 28, no. 5, pp. 339–350, 2002.
- [22] G. J. Wagner, N. Moës, W. K. Liu, and T. Belytschko, “The extended finite element method for rigid particles in stokes flow,” *International Journal for Numerical Methods in Engineering*, vol. 51, no. 3, pp. 293–313, 2001.
- [23] X. Y. Liu, Q. Z. Xiao, and B. L. Karihaloo, “Xfem for direct evaluation of mixed mode sifs in homogeneous and bi-materials,” *International Journal for Numerical Methods in Engineering*, vol. 59, no. 8, pp. 1103–1118, 2004.
- [24] F. van der Bos and V. Gravemeier, “Numerical simulation of premixed combustion using an enriched finite element method,” *Journal of Computational Physics*, vol. 228, no. 10, pp. 3605 – 3624, 2009.
- [25] S. Bordas, P. V. Nguyen, C. Dunant, A. Guidoum, and H. Nguyen-Dang, “An extended finite element library,” *International Journal for Numerical Methods in Engineering*, vol. 71, no. 6, pp. 703–732, 2007.
- [26] C. Dunand, V. P. Nguyen, M. Belgasmia, S. P. A. Bordas, A. Guidoum, and H. D. Nguyen, “New trends in the development of the x-fem, chapter architecture trade-offs including a mesher in an object-oriented extended finite element code,” 2007.
- [27] A. Menk and S. Bordas, “Influence of the microstructure on the stress state of solder joints during thermal cycling,” in *Thermal, Mechanical and Multi-Physics simulation and Experiments in Microelectronics and Microsystems, 2009. EuroSimE 2009. 10th International Conference on*, pp. 1–5, April 2009.
- [28] S. Bordas and B. Moran, “Enriched finite elements and level sets for damage tolerance assessment of complex structures,” *Engineering Fracture Mechanics*, vol. 73, no. 9, pp. 1176 – 1201, 2006.

-
- [29] N. Sukumar and J.-H. Prévost, “Modeling quasi-static crack growth with the extended finite element method part i: Computer implementation,” *International Journal of Solids and Structures*, vol. 40, no. 26, pp. 7513 – 7537, 2003.
- [30] B. Karihaloo and Q. Xiao, “Modelling of stationary and growing cracks in {FE} framework without remeshing: a state-of-the-art review,” *Computers and Structures*, vol. 81, no. 3, pp. 119 – 129, 2003.
- [31] T. Belytschko, R. Gracie, and G. Ventura, “A review of extended/generalized finite element methods for material modeling,” *Modelling and Simulation in Materials Science and Engineering*, vol. 17, no. 4, p. 043001, 2009.
- [32] V. P. Nguyen, T. Rabczuk, S. Bordas, and M. Duflo, “Meshless methods: A review and computer implementation aspects,” *Mathematics and Computers in Simulation*, vol. 79, no. 3, pp. 763 – 813, 2008.
- [33] T. Rabczuk, S. Bordas, and G. Zi, “On three-dimensional modelling of crack growth using partition of unity methods,” *Computers and Structures*, vol. 88, no. 23–24, pp. 1391 – 1411, 2010. Special Issue: Association of Computational Mechanics – United Kingdom.
- [34] G. Ventura, J. X. Xu, and T. Belytschko, “A vector level set method and new discontinuity approximations for crack growth by efg,” *International Journal for Numerical Methods in Engineering*, vol. 54, no. 6, pp. 923–944, 2002.
- [35] E. De Luycker, D. J. Benson, T. Belytschko, Y. Bazilevs, and M. C. Hsu, “X-fem in isogeometric analysis for linear fracture mechanics,” *International Journal for Numerical Methods in Engineering*, vol. 87, no. 6, pp. 541–565, 2011.
- [36] T. Rabczuk and T. Belytschko, “Cracking particles: a simplified meshfree method for arbitrary evolving cracks,” *International Journal for Numerical Methods in Engineering*, vol. 61, no. 13, pp. 2316–2343, 2004.
- [37] M. Duflo and H. Nguyen-Dang, “A meshless method with enriched weight functions for fatigue crack growth,” 2003.
- [38] E. Barbieri, N. Petrinic, M. Meo, and V. L. Tagarielli, “A new weight-function enrichment in meshless methods for multiple cracks in linear elasticity,” *International Journal for Numerical Methods in Engineering*, vol. 90, no. 2, pp. 177–195, 2012.

- [39] E. Béchet, H. Minnebo, N. Moës, and B. Burgardt, “Improved implementation and robustness study of the x-fem for stress analysis around cracks,” *International Journal for Numerical Methods in Engineering*, vol. 64, no. 8, pp. 1033–1056, 2005.
- [40] I. Babuska and U. Banerjee, “Stable generalized finite element method (sgfem),” *Computer Methods in Applied Mechanics and Engineering*, vol. 201–204, no. 0, pp. 91 – 111, 2012.
- [41] R. H. J. Peerlings, R. de Borst, W. A. M. Brekelmans, and J. H. P. de Vree, “Gradient enhanced damage for quasi-brittle materials,” *International Journal for Numerical Methods in Engineering*, vol. 39, no. 19, pp. 3391–3403, 1996.
- [42] R. de Borst, *Damage, Material Instabilities, and Failure*, pp. 22–234. John Wiley and Sons, Ltd, 2004.
- [43] M. J. Borden, C. V. Verhoosel, M. A. Scott, T. J. Hughes, and C. M. Landis, “A phase-field description of dynamic brittle fracture,” *Computer Methods in Applied Mechanics and Engineering*, vol. 217–220, pp. 77–95, 2012.
- [44] H. Gomez, V. Calo, Y. Bazilevs, and T. Hughes, “Isogeometric analysis of the Cahn-Hilliard phase-field model,” *Computer Methods in Applied Mechanics and Engineering*, vol. 197, pp. 4333–4352, 2008.
- [45] H. Gomez, T. Hughes, X. Nogueira, and V. Calo, “Isogeometric analysis of the isothermal Navier-Stokes-Korteweg equations,” *Computer Methods in Applied Mechanics and Engineering*, vol. 199, pp. 1828–1840, 2010.
- [46] A. Abdollahi and I. Arias, “Phase-field modeling of the coupled microstructure and fracture evolution in ferroelectric single crystals,” *Acta Materialia*, vol. 59, no. 12, pp. 4733 – 4746, 2011.
- [47] A. Rosolen, C. Peco, and M. Arroyo, “An adaptive meshfree method for phase-field models of biomembranes. part i: Approximation with maximum-entropy basis functions,” *Journal of Computational Physics*, vol. 249, no. 0, pp. 303 – 319, 2013.
- [48] G. Francfort and J.-J. Marigo, “Revisiting brittle fracture as an energy minimization problem,” *Journal of the Mechanics and Physics of Solids*, vol. 46, pp. 1319–1342, 1998.

-
- [49] B. Bourdin, G. Francfort, and J.-J. Marigo, “The Variational Approach to Fracture,” *Journal of Elasticity*, vol. 91, no. 1-3, pp. 5–148, 2008.
- [50] D. Mumford and J. Shah, “Optimal approximations by piecewise smooth functions and associated variational problems communications on pure and applied mathematics,” *Communications on Pure and Applied Mathematics*, vol. 42, no. 5, pp. 577–685, 1989.
- [51] L. Ambrosio, “Variational problems in sbv and image segmentation,” *Acta Applicandae Mathematica*, vol. 17, no. 1, pp. 1–40, 1989.
- [52] V. M. Ambrosio, Luigi; Tortorelli, “Approximation of functionals depending on jumps by elliptic functionals via gamma-convergence,” *Communications on Pure and Applied Mathematics*, vol. 43, no. 8, pp. 999–1036, 1990.
- [53] B. Bourdin, G. Francfort, and J.-J. Marigo, “Numerical experiments in revisited brittle fracture,” *Journal of the Mechanics and Physics of Solids*, vol. 48, no. 4, pp. 797–826, 2000.
- [54] L. Chen, T. Rabczuk, S. Bordas, G. Liu, K. Zeng, and P. Kerfriden, “Extended finite element method with edge-based strain smoothing (esm-xfem) for linear elastic crack growth,” *Computer Methods in Applied Mechanics and Engineering*, vol. 209 - 212, no. 0, pp. 250 – 265, 2012.
- [55] T. Rabczuk, “Computational methods for fracture in brittle and quasi-brittle solids: State-of-the-art review and future perspectives,” *ISRN Applied Mathematics*, vol. 2013, p. 38, 2013.
- [56] J. Dolbow, N. Moës, and T. Belytschko, “Modeling fracture in mindlin-reissner plates with the extended finite element method,” *International Journal of Solids and Structures*, vol. 37, pp. 7161–7183, 1999.
- [57] P. Baiz, S. Natarajan, S. Bordas, P. Kerfriden, and T. Rabczuk, “Linear buckling analysis of cracked plates by sfem and xfem (smxfem),” *Journal of Mechanics of Materials and Structures*, vol. 9, pp. 1213–1238, 2011.
- [58] S. Natarajan, P. Baiz, S. Bordas, T. Rabczuk, and P. Kerfriden, “Natural frequencies of cracked functionally graded material plates by the extended finite element method,” *Composite Structures*, vol. 93, no. 11, pp. 3082 – 3092, 2011.

- [59] X. Zhuang, R. Huang, H. Zhu, H. Askes, and K. Mathisen, “A new and simple locking-free triangular thick plate element using independent shear degrees of freedom,” *Finite Elements in Analysis and Design*, vol. 75, no. 0, pp. 1 – 7, 2013.
- [60] P. M. A. Areias and T. Belytschko, “Non-linear analysis of shells with arbitrary evolving cracks using xfem,” *International Journal for Numerical Methods in Engineering*, vol. 62, no. 3, pp. 384–415, 2005.
- [61] T. Rabczuk and P. Areias, “A meshfree thin shell for arbitrary evolving cracks based on an extrinsic basis,” *Computer Modeling in Engineering and Sciences*, vol. 16, no. 2, pp. 115–130, 2006.
- [62] T. Rabczuk, P. Areias, and T. Belytschko, “A meshfree thin shell method for non-linear dynamic fracture,” *International Journal for Numerical Methods in Engineering*, vol. 72, no. 5, pp. 524–548, 2007.
- [63] T. Rabczuk, R. Gracie, J.-H. Song, and T. Belytschko, “Immersed particle method for fluid–structure interaction,” *International Journal for Numerical Methods in Engineering*, vol. 81, no. 1, pp. 48–71, 2010.
- [64] S. Wu, G. Li, and T. Belytschko, “A dkt shell element for dynamic large deformation analysis,” *Communications in Numerical Methods in Engineering*, vol. 21, no. 11, pp. 651–674, 2005.
- [65] P. Areias and T. Belytschko, “Analysis of finite strain anisotropic elastoplastic fracture in thin plates and shells,” *Journal of Aerospace Engineering*, vol. 19, no. 4, pp. 259–270, 2006.
- [66] T. Chau-Dinh, G. Zi, P.-S. Lee, T. Rabczuk, and J.-H. Song, “Phantom-node method for shell models with arbitrary cracks,” *Computers and Structures*, vol. 92–93, no. 0, pp. 242 – 256, 2012.
- [67] G. Becker and L. Noels, “A full-discontinuous galerkin formulation of nonlinear kirchhoff–love shells: elasto-plastic finite deformations, parallel computation, and fracture applications,” *International Journal for Numerical Methods in Engineering*, vol. 93, no. 1, pp. 80–117, 2013.
- [68] Y. Cai, X. Zhuang, and H. Zhu, “A generalized and efficient method for finite cover generation in the numerical manifold method,” *International Journal of Computational Methods*, vol. 10, no. 05, p. 1350028, 2013.

- [69] P. Areias, J. Song, and T. Belytschko, “Analysis of fracture in thin shells by overlapping paired elements,” *Computer Methods in Applied Mechanics and Engineering*, vol. 195, no. 41–43, pp. 5343 – 5360, 2006.
- [70] F. Cirak, M. Ortiz, and A. Pandolfi, “A cohesive approach to thin-shell fracture and fragmentation,” *Computer Methods in Applied Mechanics and Engineering*, vol. 194, no. 21–24, pp. 2604 – 2618, 2005.
- [71] T. Rabczuk and T. Belytschko, “A three-dimensional large deformation meshfree method for arbitrary evolving cracks,” *Computer Methods in Applied Mechanics and Engineering*, vol. 196, no. 29–30, pp. 2777 – 2799, 2007.
- [72] S. Bordas, T. Rabczuk, and G. Zi, “Three-dimensional crack initiation, propagation, branching and junction in non-linear materials by an extended mesh-free method without asymptotic enrichment,” *Engineering Fracture Mechanics*, vol. 75, no. 5, pp. 943 – 960, 2008.
- [73] N. Sukumar, “Construction of polygonal interpolants: a maximum entropy approach,” *International Journal for Numerical Methods in Engineering*, vol. 61, no. 12, pp. 2159–2181, 2004.
- [74] C. Shannon, “A mathematical theory of communication,” *The Bell System Technical Journal*, vol. 27, pp. 623–656, 1948.
- [75] E. Jaynes, “Information theory and statistical mechanics,” *Physics Reviews*, vol. 106, pp. 620–630, 1957.
- [76] E. T. Jaynes, “Information theory and statistical mechanics. ii,” *Phys. Rev.*, vol. 108, pp. 171–190, Oct 1957.
- [77] M. Arroyo and M. Ortiz, “Local maximum-entropy approximation schemes: a seamless bridge between finite elements and meshfree methods,” *International Journal for Numerical Methods in Engineering*, vol. 65, no. 13, pp. 2167–2202, 2006.
- [78] D. Shepard, “A two-dimensional interpolation function for irregularly-spaced data,” in *Proceedings of the 1968 23rd ACM National Conference*, ACM ’68, (New York, NY, USA), pp. 517–524, ACM, 1968.
- [79] D. Millán, A. Rosolen, and M. Arroyo, “Thin shell analysis from scattered points with maximum-entropy approximants,” *International Journal for Numerical Methods in Engineering*, vol. 85, no. 6, pp. 723–751, 2011.

- [80] A. Ortiz, M. Puso, and N. Sukumar, “Maximum-entropy meshfree method for compressible and near-incompressible elasticity,” *Computer Methods in Applied Mechanics and Engineering*, vol. 199, no. 25–28, pp. 1859–1871, 2010.
- [81] A. Ortiz, M. Puso, and N. Sukumar, “Maximum-entropy meshfree method for incompressible media problems,” *Finite Elements in Analysis and Design*, vol. 47, no. 6, pp. 572–585, 2011.
- [82] C. Cyron, M. Arroyo, and M. Ortiz, “Smooth, second order, non-negative mesh-free approximants selected by maximum entropy,” *International Journal for Numerical Methods in Engineering*, vol. 79, no. 13, pp. 1605–1632, 2009.
- [83] N. Sukumar, B. Moran, and T. Belytschko, “The natural element method in solid mechanics,” *International Journal for Numerical Methods in Engineering*, vol. 43, no. 5, pp. 839–887, 1998.
- [84] F. Cirak, M. Ortiz, and P. Schröder, “Subdivision surfaces: a new paradigm for thin-shell finite-element analysis,” *International Journal for Numerical Methods in Engineering*, vol. 47, no. 12, pp. 2039–2072, 2000.
- [85] A. Tagliani, “Existence and stability of a discrete probability distribution by maximum entropy approach,” *Applied Mathematics and Computation*, vol. 110, no. 2–3, pp. 105 – 114, 2000.
- [86] V. Rajan, “Optimality of the delaunay triangulation in r^d ,” *Discrete and Computational Geometry*, vol. 12, no. 1, pp. 189–202, 1994.
- [87] H. M. Westergaard, “Bearing Pressure and Cracks,” *Journal of Applied Mechanics*, vol. 6, pp. 49–53, 1939.
- [88] G. R. Irwin, “Analysis of Stresses and Strains Near the End of a Crack Traversing a Plate,” *J. Appl. Mech.*, 1957.
- [89] A. E. Green and I. N. Sneddon, “The distribution of stress in the neighbourhood of a flat elliptical crack in an elastic solid,” *Mathematical Proceedings of the Cambridge Philosophical Society*, vol. 46, pp. 159–163, 1 1950.
- [90] M. L. Williams, “On the stress distribution at the base of a stationary crack,” *Journal of Applied Mechanics*, vol. 24, pp. 109–114, Mar. 1957.

-
- [91] X.-P. Xu and A. Needleman, “Numerical simulations of fast crack growth in brittle solids,” *Journal of the Mechanics and Physics of Solids*, vol. 42, no. 9, pp. 1397 – 1434, 1994.
- [92] G. T. Camacho and M. Ortiz, “Computational modelling of impact damage in brittle materials,” *International Journal of Solids and Structures*, vol. 33, no. 20-22, pp. 2899–2938, 1996.
- [93] J. J. C. Remmers, R. d. Borst, and A. Needleman, “A cohesive segments method for the simulation of crack growth,” *Computational Mechanics*, vol. 31, no. 1-2, pp. 69–77, 2003.
- [94] R. Timon and W. Wall, *EXtended finite element and meshfree method*. Lecture Notes, Technical University of Munich, Germany, 2007.
- [95] F. L. Stazi, E. Budyn, J. Chessa, and T. Belytschko, “An extended finite element method with higher-order elements for curved cracks,” *Computational Mechanics*, vol. 31, no. 1-2, pp. 38–48, 2003.
- [96] W. Quak, A. van den Boogaard, D. González, and E. Cueto, “A comparative study on the performance of meshless approximations and their integration,” *Computational Mechanics*, vol. 48, no. 2, pp. 121–137, 2011.
- [97] E. Béchet, H. Minnebo, N. Moës, and B. Burgardt, “Improved implementation and robustness study of the x-fem for stress analysis around cracks,” *International Journal for Numerical Methods in Engineering*, vol. 64, no. 8, pp. 1033–1056, 2005.
- [98] J. F. Yau, S. S. Wang, and H. T. Corten, “A Mixed-Mode Crack Analysis of Isotropic Solids Using Conservation Laws of Elasticity,” *Journal of Applied Mechanics-transactions of The Asme*, vol. 47, 1980.
- [99] A. Zehnder, *Fracture mechanics*. Lecture Notes, Cornell University, 2010.
- [100] T. Rabczuk and G. Zi, “A meshfree method based on the local partition of unity for cohesive cracks,” *Computational Mechanics*, vol. 39, no. 6, pp. 743–760, 2007.
- [101] T. Anderson and T. Anderson, *Fracture Mechanics: Fundamentals and Applications, Second Edition*. Taylor & Francis, 1994.

-
- [102] G. Dal Maso, *An Introduction to [gamma]-convergence*, vol. 8 of *Progress in nonlinear differential equations and their applications*. Boston, MA: Birkhäuser, 1993.
- [103] A. Braides, *Approximation of Free-Discontinuity Problems*, vol. 1694 of *Lecture Notes in Mathematics*. Springer, 1998.
- [104] A. Braides, *Gamma-convergence for Beginners*. Oxford University Press: New York, 2002.
- [105] C. Miehe, F. Welschinger, and M. Hofacker, “Thermodynamically consistent phase-field models of fracture: Variational principles and multi-field fe implementations,” *International Journal for Numerical Methods in Engineering*, vol. 83, pp. 1273–1311, 2010.
- [106] M. J. Borden, T. J. Hughes, C. M. Landis, and C. V. Verhoosel, “A higher-order phase-field model for brittle fracture: Formulation and analysis within the isogeometric analysis framework,” *Computer Methods in Applied Mechanics and Engineering*, vol. 273, no. 0, pp. 100 – 118, 2014.
- [107] P. Areias, M. Msekh, and T. Rabczuk, “Damage and fracture algorithm with the screened poisson equation,” *computational mechanics*, 2015.
- [108] M. Hofacker and C. Miehe, “Continuum phase field modeling of dynamic fracture: variational principles and staggered fe implementation,” *International Journal of Fracture*, vol. 178, no. 1-2, pp. 113–129, 2012.
- [109] B. Bourdin, “Numerical implementation of the variational formulation for quasi-static brittle fracture,” *Interfaces and Free Boundaries*, vol. 9, no. 3, pp. 411–430, 2007.
- [110] T. Hughes, J. Cottrell, and Y. Bazilevs, “Isogeometric analysis: CAD, finite elements, NURBS, exact geometry and mesh refinement,” *Computer Methods in Applied Mechanics and Engineering*, vol. 194, pp. 4135–4195, 2005.
- [111] T. J. R. Hughes, *The finite element method : linear static and dynamic finite element analysis*. Englewood Cliffs, N.J. Prentice-Hall International, 1987.
- [112] F. Amiri, D. Millán, Y. Shen, T. Rabczuk, and M. Arroyo, “Phase-field modeling of fracture in linear thin shells,” *Theoretical and Applied Fracture Mechanics*, vol. 69, no. 0, pp. 102 – 109, 2014. Introducing the new features of Theoretical

- and Applied Fracture Mechanics through the scientific expertise of the Editorial Board.
- [113] A. Gravouil, N. Moës, and T. Belytschko, “Non-planar 3d crack growth by the extended finite element and level sets—part ii: Level set update,” *International Journal for Numerical Methods in Engineering*, vol. 53, no. 11, pp. 2569–2586, 2002.
- [114] S. Timoshenko, S. Woinowsky-Krieger, and S. Woinowsky, *Theory of plates and shells*, vol. 2. McGraw-hill New York, 1959.
- [115] P. Ciarlet, “A brief introduction to mathematical shell theory,” in *Classical and Advanced Theories of Thin Structures* (A. Morassi and R. Paroni, eds.), vol. 503 of *CISM International Centre for Mechanical Sciences*, pp. 111–185, Springer Vienna, 2008.
- [116] M. L. Bucelem and K.-J. Bathe, “Higher-order mitc general shell elements,” *International Journal for Numerical Methods in Engineering*, vol. 36, no. 21, pp. 3729–3754, 1993.
- [117] J. Simo and D. Fox, “On a stress resultant geometrically exact shell model. Part I: Formulation and optimal parametrization,” *Computer Methods in Applied Mechanics and Engineering*, vol. 72, pp. 267–304, 1989.
- [118] P. Krysl and T. Belytschko, “Analysis of thin shells by the element-free galerkin method,” *International Journal of Solids and Structures*, vol. 33, no. 20–22, pp. 3057 – 3080, 1996.
- [119] L. Noels and R. Radovitzky, “A new discontinuous galerkin method for kirchhoff–love shells,” *Computer Methods in Applied Mechanics and Engineering*, vol. 197, no. 33–40, pp. 2901 – 2929, 2008.
- [120] G. Becker, C. Geuzaine, and L. Noels, “A one field full discontinuous galerkin method for kirchhoff–love shells applied to fracture mechanics,” *Computer Methods in Applied Mechanics and Engineering*, vol. 200, no. 45–46, pp. 3223 – 3241, 2011.
- [121] F. Cirak and Q. Long, “Subdivision shells with exact boundary control and non-manifold geometry,” *International Journal for Numerical Methods in Engineering*, vol. 88, no. 9, pp. 897–923, 2011.

- [122] J. Kiendl, K.-U. Bletzinger, J. Linhard, and R. Wüchner, “Isogeometric shell analysis with kirchhoff–love elements,” *Computer Methods in Applied Mechanics and Engineering*, vol. 198, no. 49–52, pp. 3902 – 3914, 2009.
- [123] D. Benson, Y. Bazilevs, M. Hsu, and T. Hughes, “Isogeometric shell analysis: The reissner–mindlin shell,” *Computer Methods in Applied Mechanics and Engineering*, vol. 199, no. 5–8, pp. 276 – 289, 2010.
- [124] N. Nguyen-Thanh, J. Kiendl, H. Nguyen-Xuan, R. Wüchner, K. Bletzinger, Y. Bazilevs, and T. Rabczuk, “Rotation free isogeometric thin shell analysis using pht-splines,” *Computer Methods in Applied Mechanics and Engineering*, vol. 200, no. 47–48, pp. 3410 – 3424, 2011.
- [125] A. Rosolen, D. Millán, and M. Arroyo, “On the optimum support size in mesh-free methods: a variational adaptivity approach with maximum entropy approximants,” *International Journal for Numerical Methods in Engineering*, vol. 82, no. 7, pp. 868–895, 2010.
- [126] F. Amiri, C. Anitescu, M. Arroyo, S. Bordas, and T. Rabczuk, “Xlme interpolants, a seamless bridge between xfem and enriched meshless methods,” *Computational Mechanics*, vol. 53, no. 1, pp. 45–57, 2014.
- [127] K. Pearson, “On lines and planes of closest fit to systems of points in space,” *Philosophical Magazine*, vol. 2, no. 6, pp. 559–572, 1901.
- [128] H. Hotelling, “Analysis of a complex of statistical variables into principal components,” *Journal of Educational Psychology*, vol. 24, no. 7, pp. 498–520, 1933.
- [129] K. Karhunen, “Zur spektraltheorie stochastischer prozesse,” *Annales Academiae Scientiarum Fennicae*, vol. 34, pp. 1–7, 1946.
- [130] M. Loève, *Probability Theory*. University series in higher mathematics, New Jersey: Van Nostrand, 1955.
- [131] E. Lorenz, “Empirical orthogonal functions and statistical weather prediction,” Statistical Forecasting Project, Scientific Report 1, MIT, Department of Meteorology, Cambridge, MA, USA, December 1956.
- [132] J. Lumley, “The structure of inhomogeneous turbulent flows,” in *Atmospheric turbulence and radio propagation* (A. M. Yaglom and V. I. Tatarski, eds.), pp. 166–178, Moscow: Nauka, 1967.

-
- [133] I. Jolliffe, *Principal Component Analysis*. Springer Series in Statistics, New York, NY, USA: Springer, second ed., 2002.
- [134] D. Donoho and C. Grimes, “Hessian eigenmaps: locally linear embedding techniques for high-dimensional data,” *Proceedings of the National Academy of Sciences*, vol. 100, pp. 5591–5596, May 2003.
- [135] Z. Zhang and J. Wang, “Mlle: Modified locally linear embedding using multiple weights,” in *Advances in Neural Information Processing Systems 19* (B. Schölkopf, J. Platt, and T. Hoffman, eds.), pp. 1593–1600, Cambridge, MA: MIT Press, 2007.
- [136] D. Levin, “Mesh-independent surface interpolation,” in *Geometric Modeling for Scientific Visualization* (H. Brunnett and Mueller, eds.), pp. 37–49, Springer-Verlag, 2003.
- [137] G. Karypis and V. Kumar, *METIS: Unstructured Graph Partitioning and Sparse Matrix Ordering System*. Department of Computer Science and Engineering, University of Minnesota, version 4.0 ed., 1998.
- [138] F. Cirak and M. Ortiz, “Fully C^1 -conforming subdivision elements for finite deformation thin-shell analysis,” *International Journal for Numerical Methods in Engineering*, vol. 51, no. 7, pp. 813–833, 2001.
- [139] J. Simo, D. Fox, and M. Rifai, “On a stress resultant geometrically exact shell model. Part II: the linear theory; computational aspects,” *Computer Methods in Applied Mechanics and Engineering*, vol. 73, pp. 53–92, 1989.
- [140] T. Rabczuk, S. P. Xiao, and M. Sauer, “Coupling of mesh-free methods with finite elements: basic concepts and test results,” *Communications in Numerical Methods in Engineering*, vol. 22, no. 10, pp. 1031–1065, 2006.
- [141] Y. Cai, X. Zhuang, and C. Augarde, “A new partition of unity finite element free from the linear dependence problem and possessing the delta property,” *Computer methods in applied mechanics and engineering.*, vol. 199, pp. 1036–1043, January 2010.
- [142] N. Vu-Bac, H. Nguyen-Xuan, L. Chen, C. K. Lee, G. Zi, X. Zhuang, G. R. Liu, and T. Rabczuk, “A phantom-node method with edge-based strain smoothing for linear elastic fracture mechanics,” *Journal of Applied Mathematics*, p. 12, 2013.

-
- [143] X. Zhuang, H. Zhu, and C. Augarde, “An improved meshless shepard and least squares method possessing the delta property and requiring no singular weight function,” *Computational Mechanics*, pp. 1–15, 2013.
- [144] A. Henderson, *The ParaView Guide: A Parallel Visualization Application*. Kitware Inc., 2007.
- [145] L. Ambrosio, N. Fusco, and D. Pallara, *Functions of Bounded Variation and Free Discontinuity Problems (Oxford Mathematical Monographs)*. Oxford University Press, USA, May 2000.
- [146] A. Chambolle, “An approximation result for special functions with bounded deformation,” *Journal de Mathématiques Pures et Appliquées*, vol. 83, no. 7, pp. 929 – 954, 2004.
- [147] R. March and M. Dozio, “A variational method for the recovery of smooth boundaries,” *Image and Vision Computing*, vol. 15, no. 9, pp. 705 – 712, 1997.
- [148] S. Esedoglu and J. Shen, “Digital inpainting based on the mumford-shah-euler image model,” *European J. Appl. Math*, vol. 13, pp. 353–370, 2002.
- [149] P. Ciarlet, *Mathematical elasticity, Vol III: theory of shells*. North-Holland, 2000.

Curriculum Vitae

Fatemeh Amiri

Institute of Structural Mechanics
Bauhaus-Universität Weimar
Marienstraße 15, 99423 Weimar, Germany
Email: fatemeh.amiri@uni-weimar.de
Date of Birth: 21.03.1984
Nationality: Iranian

Education

- Ph.D: Institute of Structural Mechanics, Bauhaus-University Weimar, Germany, 2015.
- MS.c: Master of Science at Isfahan University of Technology, Iran, 2010.
- BS.c: Bachelor at Shahid Chamran University of Ahvaz, Iran, 2007.

Research Interests

- Fracture mechanics
- Structural mechanics
- Computational materials design
- Numerical Relativity simulations of black holes
- Applied Mathematics

Skills and Expertise

C++, Matlab, Fortran, Pascal, Maple, Mathematica, Paraview viewer, Gmsh mesh generator, Tecplot, Latex, Numerical simulations.

Publications Refereed Journal Articles

- F. Amiri, C. Anitescu, M. Arroyo, S. Bordas, and T. Rabczuk, “Xlme interpolants, a seamless bridge between xfem and enriched meshless methods,” *Computational Mechanics*, vol. 53, no. 1, pp. 45–57, 2014.
- F. Amiri, D. Millan, Y. Shen, T. Rabczuk, and M. Arroyo, “Phase-field modeling of fracture in linear thin shells,” *Theoretical and Applied Fracture Mechanics*, vol. 69, pp. 102 – 109, 2014.